1.0

1.1

1.25   1.4   1.6

4.5 2.8 2.5
5.0 3.2 2.2
5.6 3.6
      4.0 2.0

1.8

MICROCOPY RESOLUTION TEST CHART

AFOSR-TR- 80-0220

LEVEL II

Air Force Office of Scientific Research

Eglin Air Force Base

Grant AF-AFOSR 78-3569

THE INFLUENCE OF BALLISTIC DAMAGE
ON THE AEROELASTIC CHARACTERISTICS OF
LIFTING SURFACES

by

D. S. Scott

J. C. Westkaemper

A. Sigal

R. O. Stearman

DTIC
ELECTE
MAR 27 1980
E

Department of Aerospace Engineering and Engineering Mechanics
The University of Texas at Austin
Austin, Texas   78712

ADA082536

DDC FILE COPY

80 3   20 028

SECURITY CLASSIFICATION OF THIS PAGE (When Data Entered)

REPORT DOCUMENTATION PAGE	READ INSTRUCTIONS BEFORE COMPLETING FORM

1. REPORT NUMBER	2. GOVT ACCESSION NO.	3. RECIPIENT'S CATALOG NUMBER
AFOSR-TR- 80 - 0220		

4. TITLE (and Subtitle)	5. TYPE OF REPORT & PERIOD COVERED
THE INFLUENCE OF BALLISTIC DAMAGE ON THE AEROELASTIC CHARACTERISTICS OF LIFTING SURFACES	1 Feb 78 — 31 Jan 80 Interim
	6. PERFORMING ORG. REPORT NUMBER

7. AUTHOR(s)	8. CONTRACT OR GRANT NUMBER(s)
D. S. Scott R. O. Stearman J. C. Westkaemper A. Sigal	AFOSR-78-3569

9. PERFORMING ORGANIZATION NAME AND ADDRESS	10. PROGRAM ELEMENT, PROJECT, TASK AREA & WORK UNIT NUMBERS
Dept. of Aerospace Engineering & Engr. Mechanics University of Texas at Austin Austin, TX 78712	61102F 2301/A6

11. CONTROLLING OFFICE NAME AND ADDRESS	12. REPORT DATE
AFOSR/NP Bolling AFB, Bldg. #410 Wash DC 20332	Jul 79
	13. NUMBER OF PAGES
	196

14. MONITORING AGENCY NAME & ADDRESS(if different from Controlling Office)	15. SECURITY CLASS. (of this report)
	unclassified
	15a. DECLASSIFICATION/DOWNGRADING SCHEDULE

16. DISTRIBUTION STATEMENT (of this Report)

Approved for public release;
distribution unlimited.

17. DISTRIBUTION STATEMENT (of the abstract entered in Block 20, if different from Report)

18. SUPPLEMENTARY NOTES

19. KEY WORDS (Continue on reverse side if necessary and identify by block number)

Damages Lifting Surfaces
Drag Divergence
Aeroelasticity & Ballistic Damage

20. ABSTRACT (Continue on reverse side if necessary and identify by block number)

An investigation is carried out to determine whether ballistic damage can seriously degrade the aeroelastic integrity of lifting surfaces on aircraft. A promising aeroelastic failure mechanism is identified that results from the localized drag generated when a lifting surface encounters severe damage to its aerodynamic shape. This damage induced drag is shown to significantly decrease the divergence speed of a generic or statistical fighter wing for certain damage site locations while increasing the flutter speed of the wing. Consequently,

DD FORM 1473 EDITION OF 1 NOV 65 IS OBSOLETE

a critical damage level exists where divergence becomes the critical
aeroelastic instability for a wing which may still have adequate strength
and flutter integrity. In view of the very limited information existing on
the aerodynamic modeling of damaged lifting surfaces, a combined analytical
and experimental modeling study was initiated to investigate the flow field
in the vicinity of thru hole type damages on lifting surfaces.

THE INFLUENCE OF BALLISTIC DAMAGE
ON THE AEROELASTIC CHARACTERISTICS OF
LIFTING SURFACES

Accession For	
NTIS GRA&I	☒
DDC TAB	☐
Unannounced	☐
Justification	

by

D. S. Scott

J. C. Westkaemper

A. Sigal

R. O. Stearman

By		
Distribution/		
Availability Codes		
Dist	Avail and/or special	
A		

Department of Aerospace Engineering and Engineering Mechanics
The University of Texas at Austin
Austin, Texas   78712

(AFSC)

d is
(7b).

A.
Technical Information Officer

ACKNOWLEDGEMENTS

ABSTRACT

An investigation is carried out to determine whether ballistic
damage can seriously degrade the aeroelastic integrity of lifting
surfaces on aircraft. A promising aeroelastic failure mechanism
is identified that results from the localized drag generated when a
lifting surface encounters damage to its aerodynamic shape. This
damage induced drag is shown to significantly decrease the divergence
speed of a generic or statistical fighter wing for certain damage site
locations while increasing the flutter speed of the wing. Consequently,
a critical damage level exists where divergence becomes the critical
aeroelastic instability for a wing which may still have adequate
strength and flutter integrity. In view of the very limited infor-
mation existing on the aerodynamic modeling of damaged lifting surfaces,
a combined analytical and experimental modeling study was initiated to
investigate the flow field in the vicinity of through hole type
damages on lifting surfaces.

TABLE OF CONTENTS

TABLE OF CONTENTS Cont'd.

LIST OF TABLES

LIST OF FIGURES

LIST OF FIGURES

LIST OF FIGURES

1. INTRODUCTION

The influence of inflight ballistic damage on the aeroelastic response of an aircraft is not yet well understood. The primary damages of interest are those sustained by the lifting surfaces, that is, the aircraft wings and tail sections. A review of inflight films illustrating ballistic damage to aircraft indicates that in some cases an aircraft can tolerate a significant amount of damage from several hits while in other cases a single hit may result in the immediate destruction of the aircraft. While small damage could kill an aircraft by destroying vital functions such as controls or control linkages, or possibly through the ignition of a section of the fuel system, a question naturally arises as to whether a reasonably small amount of damage might occur in a critical area of the aircraft that could promote an explosive type of flutter or divergence instability. These instabilities would most likely destroy the aircraft. Alternatively, aerodynamic discontinuities caused by damage could also induce severe buffeting phenomenon. This is due to the formation of separated flow or wakes from bluff geometries generated by the damage. Many modern aircraft wings and tail surfaces are very stiff, and if flutter, divergence or buffeting is responsible for the aircraft breakup, the phenomenon would probably occur too rapidly for positive identification from combat films. In the present study an investigation is carried out to determine whether ballistic damage can seriously degrade the aeroelastic integrity of lifting surfaces on aircraft.

1

Several phenomenon known to reduce critical flutter and divergence speeds of lifting surfaces are first reviewed and attempts made to correlate their possible occurrence with classes of ballistic damage. After reviewing these potential aeroelastic failure modes that might be induced by ballistic damage, a promising mechanism is identified that results from the localized drag that can be generated on a lifting surface due to significant damage to its aerodynamic shape. When this localized drag occurs at critical positions over the surface it significantly lowers the divergence speed of the surface. For this reason, this failure mechanism will be referred to as a "drag divergence" mode of instability.

One of the more common types of damage to a lifting surface is the through hole caused by gunfire. An extensive literature search indicated that no analytical tools are available to investigate this problem from an aeroelastic modeling point of view. That is, a description of the steady and unsteady air loads cannot currently be predicted on a lifting surface with hole type discontinuities. This is due to the complex nature of the flow field in the localized damaged area which involves strong viscous interactions and separated flow effects. This literature search also indicated that virtually no recent experimental studies have been carried out on this more common type of damage. In view of this, the present study devoted a significant effort toward the investigation of through hole type modeling of damaged lifting surfaces.

A potential flow modeling of a surface with a through hole type damage was conducted utilizing an established lifting surface code designed to minimize computational effort. A parallel wind tunnel study of damaged lifting surfaces was also initiated. These companion studies were designed to provide further insight into the appropriate modeling of damaged lifting surfaces.

2. AEROELASTIC ANALYSIS OF DAMAGED
LIFTING SURFACES

Plausible arguments can be presented that demonstrate how flutter instabilities can be triggered by damage to certain critical elements of aircraft. These failure modes can be made to occur on straight or swept lifting surfaces that can be modeled as thin elastic beams or plates. Lifting surfaces employed on contemporary, variable geometry, and light weight fighters have wing thickness ratios that would for the most part qualify as such thin structures.

Some of the first and most comprehensive work on this subject was conducted in 1950 by Biot and Arnold as outlined in Reference 1. The results of their studies demonstrated that aeroelastic instabilities were not easily triggered by ballistic damage. Furthermore, if sufficient structural damage was imposed on a lifting surface to lower its flutter and divergence speeds into the flight envelope, the surfaces would fail due to inadequate strength rather than due to inadequate stiffness. In essence, the reduction of flutter and/or divergence margins by 25% required nearly an 80% loss of stiffness at certain critical sections within the wing. It was probably the impact of this finding that delayed any further investigation of this subject for nearly 30 years.

A recent investigation by Hemmig, Venkayya, and Eastep (Reference 2) has incorporated more contemporary finite element techniques

to model structural damage to lifting surfaces. Their results also suggest the difficulty of reducing flutter and divergence margins of highly redundant lifting surface structures much below the levels suggested by Biot and Arnold. Some further insight into the problem was obtained here, however, when it was demonstrated that highly optimized structural designs may demonstrate increased aeroelastic sensitivity to ballistic damage.

Further, more recent, aeroelastic investigations of lifting surfaces within the literature suggest that additional refinements in the aerodynamic modeling may be in order. 3/ 4/ In essence, the chordwise forces due to drag and leading edge suction were found to have an observable influence on the flutter and divergence boundaries for certain wing geometries. In addition, other investigations outlined in the appendix also suggest that wings with a highly optimized aerodynamic configuration will demonstrate increased sensitivity to ballistic damage through larger drag rises. In view of this, a portion of the present study concentrates on an extension of the earlier Biot and Arnold work by incorporating into their analysis significant chordwise forces due to drag that arise as the result of the ballistic damage.

In the following, suggestions are made of some flutter and divergence phenomenon that might be triggered by ballistic damage. One of these phenomenon, classified here as drag divergence , was then chosen as the first topic to be investigated.

2.1 Review of Phenomenon Known to Reduce Critical Flutter and Divergence Speeds of Aircraft

One of the more obvious aeroelastic failure modes that can be triggered on aircraft is that of control surface flutter. This possibility results from the fact that all primary controls on modern aircraft are hard hydraulic or irreversible systems. They, therefore, need not be mass balanced to the extent that a soft control would be to prevent control induced flutter. A critical flutter instability could be triggered in this case by cutting out the hydraulic actuator to the control or possibly damaging critical elements of the hydraulic control circuit. The desired result is to produce a soft control which will initiate a control induced flutter as a result of the low frequency degree of freedom that has been added to the system dynamics. If a redundant mass balance is included on the control to allow for such damage, it must also be at least partially removed by the critical hit. Flutter, induced by means of soft controls, occurs as a result of the low natural frequency of this control degree of freedom and the strong dependence of this frequency upon the aircraft flight speed. This low frequency branch representing the free floating control cuts up rapidly through the other structural mode branches of the system as the velocity increases, giving rise to the possibility of several binary flutter instabilities that could be triggered. This is a typical feature of such free floating or soft controls. On ailerons or flaps, for example, this would induce the aileron or flap mode to couple with the first or higher wing bending and/or torsional degrees of freedom to initiate a flutter instability. Similar features would also occur on rudder and elevator controls as well as for any soft servo tabs that are located

6

on soft controls. On the other hand, for stabilators a stall flutter condition could occur as the relatively free to flap control rotates into the stall regime. In this latter case no frequency coalescence or modal coupling would be needed to trigger flutter.

The above cited examples illustrate a few types of damage that can be modeled with existing aerodynamic and structural dynamic tools. Their aeroelastic integrity can be studied for a given aircraft, and the proposed hypothesis of critical damage-inducing destructive flutter verified.

The influence of a soft control on an aileron flap-wing bending-torsion mode of flutter is illustrated in Figure 1, taken from Reference 5. The typical section model employed in this analysis is illustrated in Figure 2c. This study illustrates that the flutter speed of the wing aileron system can be easily reduced by more than 60% when the control is reduced from that of a hard hydraulic system $\omega_\beta/\omega_\alpha$ large to a soft system $\omega_\beta/\omega_\alpha$ less than 0.5, where ω_α is the first wing torsion mode frequency and ω_β is the aileron flap mode frequency. This analysis also indicates that it is not necessary to completely cut out all of the control stiffness but simply reduce it to some fraction of the first wing torsion mode frequency.

Some contemporary fighter aircraft designs involve canard geometries (Viggen fighter), strakes and leading edge flaps (F-16) and highly swept wings (F-111). Under maneuvering flight conditions and at moderate to high angles of attack all of these configurations have vortex

7

line formations interacting with the main lifting surface. These vortex filaments provide a nonlinear lift effect which tends to increase the local lift curve slope of the surface. Since the classical wing flutter and divergence speeds are roughly inversely proportional to lift curve slope, a corresponding reduction in flutter and divergence speeds are expected at these moderate to high angles of attack. This has, in fact, been demonstrated in a recent flutter analysis as illustrated in Figure 3, taken from Reference 6. In this study, Stark has shown that the leading edge vortex from the delta wing of the Viggen fighter aircraft flying at a moderate 3° angle of attack lowers the flutter speed over the zero lift condition by approximately 17%. From this study it appears that damage induced during maneuvering flight conditions will be more effective in reducing flutter and divergence margins of these aircraft. It also suggests that damage which introduces vortex formations over the lifting surfaces would be detrimental to its flutter and divergence characteristics as long as the circulation from the vortex cell increased the effective lift curve slope of the wing.

Aerodynamic interference effects associated with variable geometry aircraft can significantly influence their flutter and divergence margins. This is illustrated in Figure 4a where it is shown that the flutter margins of these aircraft can be potentially reduced when the aircraft is in the high speed attack mode (that is for a fully swept back wing). Types of ballistic damage that may result in further loss of

8

flutter margin for these aircraft can be deduced from Figure 4b. Here
the wing tail flutter speed for these aircraft is seen to strongly
depend upon the ratio of first wing symmetric bending frequency, ω_h,
to first fuselage uncoupled torsion frequency, ω_θ. Both experimental
wind tunnel model studies and analytical investigations indicated a
pronounced minimum in this flutter boundary for $0.2 < \omega_h/\omega_\theta < 1$. To
maximize flutter margin, the aircraft configuration will most likely
be designed to a frequency ratio sufficiently removed from that value
associated with this minimum flutter speed. If the aircraft is designed
to the low side of this frequency ratio, say Point A, damage to the
fuselage torque box could drive ω_θ down and increase the ratio (ω_h/ω_θ)
to the critical value decreasing the flutter speed of the aircraft.
Model tests indicate that this reduction might be 15-20%. 7/ If
the aircraft is designed to operate at the higher end of this frequency
ratio, say Point B, structural damage to the wing alone might lower the
flutter speed 20-30% as indicated by model tests. More specific esti-
mates can be determined once a given variable aircraft geometry is iden-
tified.

In past vulnerability studies on aircraft, the drag increase
due to damage has been a major factor in an aircraft mission kill analy-
sis. An increase of aerodynamic drag due to ballistic damage is probably
the easiest of all damages to impose since most any surface area that is
damaged on the aircraft will usually result in some drag increment. It
is easy to visualize, for example, how the drag of a lifting surface

9

can be increased by an order of magnitude due to ballistic damage at its leading edge. Until recently, the chordwise forces due primarily to drag terms have been ignored in the aeroelastic analysis of lifting surfaces since their influence is usually an order of magnitude smaller than the lift or moment contributions for many lifting surface configurations. Current research, however, has shown that on configurations such as all moving control surfaces with special hinge axles, higher aspect ratio lifting surfaces, and possibly for T-tails, and "cranked" wings, drag forces can significantly influence the flutter and divergence boundaries on undamaged lifting surfaces. 8/ 3/ 4/ Figure 5, from Reference 4, for example, demonstrates the influence that different levels of drag, uniform and constant along the span, can have on the flutter and divergence boundaries of lifting surfaces. This figure also suggests that for high aspect ratio wings typical of those found on rotors, sailplanes, and possibly long range bombers, the stability of the surface should be investigated about its deformed state or actual flying shape rather than around its zero lift state. This latter structural effect is probably not as important for stiff fighter wings even in the presence of damage. In view of these results, it seems quite likely that the drag increments due to ballistic damage, which are an order of magnitude larger than for the undamaged wing and of course more spacially concentrated, can significantly influence flutter and divergence boundaries of lifting surfaces.

After reviewing several phenomenon that are known to reduce

critical flutter and divergence speeds of aircraft lifting surfaces, a
drag divergence mode of failure is proposed as one easily imposed by
ballistic damage and one likely to significantly degrade the aeroelastic
integrity of the lifting surface.

2.2 Proposed Drag Divergence Failure Mechanism

A drag divergence failure mechanism has been postulated for
damaged aircraft wings where the damage is of such a nature that high
chordwise forces are generated near the tip of the wing. This causes
the wing to snap or diverge laterally as indicated in Figure 6, producing
an instability similar to the lateral buckling of thin beams under con-
centrated inplane tip loads. This mechanism of failure is based upon
the premise that large drag loads and resulting chordwise forces can be
imposed on the structure through selected types of damage. For example,
if the damage occurs in the leading edge region of the wing, a limited
amount of experimental evidence indicates that one might increase the
local profile drag coefficient by a factor of four or five. 9/ 10/
During maneuvering flight conditions, induced drag levels can also be
increased by a significant amount when damage is imposed on the wing. 9/*
A parametric study is outlined below which demonstrates the plausibility
of lowering the divergence speeds of a typical fighter aircraft wing to
within its flight envelope when a damage induced drag term and a resulting
chordwise force are included in the aeroelastic analysis. Traditional
aeroelastic studies in the past have overlooked the damaged induced drag

---

*See also the Appendix

11

force as producing a plausible failure mechanism or as even having any significant influence on flutter and divergence margins of lifting surfaces. 3/ 4/ 1/

To check the above proposed failure mechanism a generic or statistical model of a typical 1950 fighter aircraft wing was employed which was basically the model developed in Reference 1. In that study, Biot and Arnold conducted a comprehensive investigation which involved a flutter and divergence analysis of a typical model of a fighter wing subjected to a wide range of structural damage conditions. The basic aeroelastic parameters of this typical wing were chosen to be the geometric mean of some fourteen different fighter aircraft. These are representative of the early 1950 fighter configurations which had moderate aspect ratio straight wings. Table I contains a listing of these fourteen aircraft. In determining the typical fighter wing, the geometric mean of the parameters was employed inasmuch as it gives less weight to the extreme, or fringe, values of a set of variates than to those values nearer the mean. The undamaged wing parameters of this typical model are given in Table II.

The present investigation employed basically the same modal analysis approximation and strip theory aerodynamic modeling that was employed in Reference 1. (See Figure 2) One additional parameter was included, however, which accounted for the steady state chordwise drag force that occurred as a result of the damage and which was not included in the study of Reference 1. Since even significant amounts of structural damage were shown in Reference 1 to result in only minor changes to the flutter and divergence speeds of this typical wing, another failure mecha-

12

nism had to be investigated. It was important that this mechanism be capable of producing a structural failure of a wing which still had an adequate strength margin in the presence of the structural damage. This suggested an aerodynamic damage* mechanism such as a high increase in local drag induced on the wing which would in turn significantly influence an aeroelastic type of instability. In the following, it is shown that the proposed drag divergence mechanism might accomplish this. An estimate of damage induced drag levels can be obtained based upon the experimental studies of References 9 and 10 where different types of damage have been classified, their resulting drag increments measured in the wind tunnel, and a few limited drag models developed.

2.2.1 Damage Classification

There are numerous combinations of damage shape and size that may occur due to a ballistic hit, depending on the structure and flight conditions. The consequence of a hit may range from very little effect up through a mission kill or a complete aircraft destruction. A mission kill occurs when the damage causes a change in the aircraft's performance such that it is unable to complete its mission. 9/ Any type of damage that results in either an aircraft or mission kill is significant enough to require investigation.

It has been noted that a prominent cause of mission defeat is a drag rise creating a loss of altitude or range. 9/ However, it has only recently been shown that drag forces may play an important

---

*Aerodynamic damage is the modification of the aerodynamic forces arising from the change of shape of the aircraft.

13

role in the aeroelastic response of an aircraft. 3/ 4/ Through wind tunnel tests, drag due to aerodynamic damage has been shown to be a first order effect. 12/ Tables III and IV, and Figure 7, reproduced from References 9, 10, and 12, show some damage classes and their associated drag effects. As can be seen, a 1% hole of type A, which represents a projectile entry through the leading edge and exit through the upper wing surface, can easily double the minimum drag of the undamaged aircraft (Figure 7). It is significant to note that this is a localized drag force concentrated in the region of the damage. As mentioned previously, when this damage is located near the tip of the wing it tends to produce lateral divergence of the wing. This divergence is similar to the classical lateral buckling of thin beams by in-plane tip loadings as viewed in Figure 6. It has been shown that inclusion of a uniform running drag load into the aeroelastic analysis can decrease critical flutter speeds of high aspect-ratio wings by as much as 15%. (See Figure 5 and Reference 3). Additionally, for these same high aspect-ratio wings, certain combinations of rigidity and drag may render divergence more critical than flutter. For moderate to small aspect-ratio wings the drag is shown to increase the flutter speeds but the divergence speed is still reduced by the presence of a drag term. These observations imply that the addition of a large concentrated drag force, located near the wing-tip, may cause an aircraft kill through a wing divergence failure mode.

Any type of damage, then, that results in high drag forces, may render an aircraft inoperative through either a mission kill or an immediate kill from aeroelastic wing divergence. It should be noted

14

that damaged leading edges of lifting surfaces give rise to excep-
tionally high drag forces. Any type of damage tending to blunt or
distort the leading edge could create a significant drag rise. An
estimate for the drag rise due to blunting the leading edge can be
obtained from Table IV, which is based on the method of Reference 10.
For example, for M = 0.8, full span leading edge damage can cause a
wing of thickness ratio of 6% to develop a ΔC_D of 0.02 to 0.03, which
is about 3 to 5 times the friction drag.

In summary, it is proposed that localized drag forces near
the wing tip can significantly lower the wing divergence margins of an
aircraft, leaving the aircraft especially vulnerable in high 'g'
maneuvers. The following aeroelastic study confirms this by investi-
gating the high drag configuration of flow-through type holes located
in the outboard portion of the wing that give rise to a drag divergence
type of failure mechanism.

2.2.2 Estimate of Drag Increments Due to Damage

The current state of the art for estimating damage induced
drag levels leaves much to be desired. The estimation of both parasite
and induced drag increments due to through hole and other classes of
damage to lifting surfaces needs further experimental and analytical
research effort. At the present, probably the best estimate of damage
induced drag levels can be obtained from the experimental studies of

15

Reference 9.[*] In this study, drag changes due to damage are reflected
in a lifting surface drag polar

$$C_D = C_{D_\pi} + pC_L^2$$

as changes in the zero lift drag coefficient C_{D_π} and the slope p
which is the additional drag due to angle of attack. While it is
questionable as to whether such a simple drag model can properly account
for various spanwise and chordwise damage locations and damage types, it
appeared to be the best tool available when the present study was under-
taken.

It is important, however, to make a few comments on some
special features of the test conditions upon which this drag model was
developed before proceeding. First, the basic study was conducted on
a two-dimensional wing, thus the slope p in the expression for C_D
should not be interpreted as induced drag in the sense of a finite
wing. Secondly, these parameters were measured on a 2 ft. chord and
an 8 1/2 ft. span two-dimensional wing section having a symmetrical
NACA 65_1-012 profile. The Reynolds number of the tests was 3.7×10^6
which is sufficiently large that the measurements may be applied to full
scale damaged aircraft. Although this thickness wing was typical of aircraft

---

[*]A few more current studies recently came to the attention of the
authors which provided some additional insight into the problem of
estimating damage induced drag levels. 10/ Some estimates from this
study are presented in the Appendix.

16

similar to the generic or statistical fighter wing employed in the present study, it is not representative of most contemporary fighter aircraft. The investigation also included some configurations with edges of the holes raised to form a "scoop" or a "spoiler" lip. The height of the lips were 1/2" and 1" or about 2% and 4% of the local chord. Naturally, such protuberances generate a considerable drag. There is some indication, however, that actual petals on damaged wings of high performance fighters do not exceed 1", which is only a fraction of 1% of the full scale chord. Some care should, therefore, be utilized when applying damage cases E and F of Table III. Finally, for the estimation of the influence of damage induced aerodynamic drag on the aeroelastic characteristics of lifting surfaces some additional questions naturally arise. That is, whether one considers damage in-flicted at constant lift where the pilot has initiated the necessary control response to maintain the desired flight conditions or whether damage is induced at a constant angle of attack. It is believed that the actual case lies between estimates based on fixed lift coefficient and fixed angle of attack. A better estimate cannot be made at the present stage of the study since the required aerodynamic data is lacking. A further discussion on this problem can be found in the Appendix.

In the following study illustrative drag estimates are made based upon the constant lift approach although the aeroelastic analysis is independent of how this actual drag estimate is determined. In summary, first order aerodynamic damage effects employed in the aero-elastic modeling were considered to be the steady drag load resulting from the damage.

17

Employing the model of Reference 9, a coefficient of drag increase C_D^* is defined in terms of a damage area as

$$C_D^* = \frac{\Delta D}{A} = C_D \frac{S}{A}$$

S = wing area

A = hole or damage area (entrance holes plus exit holes divided by 2)

and then

$$C_D^* = C_{D_\pi}^* + p^* C_L^2$$

with

$$C_{D_\pi}^* = \Delta C_{D_\pi} \frac{S}{A}$$

$$p^* = \Delta p \frac{S}{A}$$

That is, $C_{D_\pi}^*$ and p^* represent increments in the drag polar based upon the hole damage area, i.e., the sum of the entrance and exit hole areas divided by two. A tabulation of experimentally determined values of $C_{D_\pi}^*$ and p^* is given in Table III. The classes of damage (i.e., leading edge, mid chord, etc.) are also presented under Table III.

18

A more detailed description of the specific damage cases studied
can be found in Figures A.2 and A.3 of the Appendix. From Table III
it is evident that

$$C^*_{D_\pi} \leq 3.4$$

$$p^* \leq 16$$

represent experimentally determined upper bound values for the drag
parameters. These larger values occur for the leading edge class A
or B type damage at the higher subsonic Mach numbers for the smaller
holes. Based upon the data of Table III, a conservative damage induced
drag estimate for the lower Mach number range would be

$$C^*_D = 1.0 + 5C_L^2$$

while an upper bound estimate possibly more appropriate for the higher
Mach numbers and larger holes would appear to be

$$C^*_D = 2.4 + 10C_L^2$$

19

These damaged induced drag coefficients are based upon the assumption that leading edge type damages are imposed upon the lifting surfaces.

To obtain an estimate of the actual levels of damage induced drag force that can be imposed on the typical fighter aircraft in combat, consider the following fighter parameters. [9]

$$
\begin{aligned}
\text{weight } w &= 21{,}000 \text{ lb} \quad \text{(including stores)} \\
\text{wing area } S &= 300 \text{ ft}^2 \quad \text{(including fuselage carry thru)} \\
\text{aspect ratio } \mathcal{R} &= 4.5 \\
C_{D_\pi} &= 0.014 \quad \text{(clean fighter)} \\
C_{D_\pi} &= 0.026 \quad \text{(fighter with external stores)} \\
p &= 0.083 \\
\text{combat altitude } & 20{,}000 \text{ ft}
\end{aligned}
$$

Based upon these parameters and a 600 mph cruise condition an estimate of the lift coefficient gives

$$
C_L = \frac{w}{1/2\ \rho U^2 S} = \frac{(21{,}000)2}{(.5332)(0.002378)(1.467 \times 600)^2\ 300}
$$

$$
C_L = 0.143
$$

At these cruise conditions a leading edge type damage could give rise to the following drag coefficient increments:*

---

*An assumption is made at this point that the total lift is held approximately constant and the aircraft in a level flight attitude by means of a pilot induced control response.

20

$$C_D^* \cong 1.10 \quad \text{Conservative estimate}$$

$$C_D^* \cong 2.60 \quad \text{Upper bound estimate}$$

The actual drag increment, based upon wing area, for a hole type damage with an equivalent area of 3% of the wing area is

$$\Delta C_D \cong C_D^* \frac{A}{S} = 0.03(1.10)$$

$$\Delta C_D \cong 0.033 \quad \text{Conservative estimate}$$

$$\Delta C_D \cong 0.078 \quad \text{Upper bound estimate}$$

The cruise drag of the undamaged fighter is

$$C_D \cong 0.014 + 0.083(.143)^2$$

$$C_D \cong 0.016 \quad \text{Clean fighter}$$

$$C_D \cong 0.026 + 0.083(0.143)^2$$

$$C_D \cong 0.028 \quad \text{Fighter with stores}$$

Considering the conservative and upper bound estimates for damage in-duced drag on a wing, it appears that for the equivalent of a 3% damage area (i.e. 3% of total wing area is damaged) the drag due to damage

21

could range from approximately 2 to 5 times the total cruise drag on a clean fighter for the above flight conditions and up to 3 times the total cruise drag of the fighter with stores. (Compare also Figure 7) These drag levels for the undamaged fighter are respectively

$$D_{clean} \simeq (0.0157)(0.5)(.001268)600(1.467)^2(300)$$

$$D_{clean} \simeq 2300 \quad \text{(clean fighter)}$$

$$D_{stores} \simeq 4000 \quad \text{(fighter with stores)}$$

In this high speed 600 mph one 'g' level flight condition at 20,000 ft. altitude localized drag on the wing due to damage equivalent to 3% of the wing area might range from a conservative estimate of

$$D_{damage} \simeq 4800 \quad \text{Conservative estimate}$$

to

$$D_{damage} \simeq 11,200 \quad \text{Upper bound estimate}$$

These drag levels are not sufficient to lower the flutter and divergence speeds of a wing with slight structural damage into its flight envelope (650 mph U_{true} for this typical fighter). This fact will be demonstrated later.

Under combat or maneuvering flight conditions, however, which is characteristic of when damage will occur on a fighter aircraft, the situation becomes more critical. This can best be illustrated by

22

considering the typical fighter during a high 'g' pull out or turning maneuver. The damage induced drag can be calculated, for example, at 20,000 ft. altitude and 600 mph true air speed in a five 'g' maneuver from the lift coefficient as follows:

$$C_{L_{5g}} = \frac{nW}{1/2\rho U^2 S}$$

$$= \frac{5(21,000)(2)}{(.5332)(.002378)(880.2)^2(300)}$$

$$C_{L_{5g}} = 0.713$$

which is an attainable C_L value for this aircraft even for moderate damage. This results in the following drag coefficient increments:[*]

$$C_D^* \cong 1.0 + 5(.713)^2 = 3.54 \quad \text{Conservative estimate}$$

$$C_D^* \cong 2.4 + 10(.713)^2 \cong 7.5 \quad \text{Upper bound estimate}$$

The resulting drag increment for a 3% damage area under the above maneuvering flight conditions will range between

$$\Delta D = C_D^*(.03)(300)(0.5)(.5332)(.002378)(880.2)^2$$

$$\Delta D \cong 4420 \ C_D^*$$

---

[*]It is again assumed at this point that the pilot induces the appropriate control response to hold C_L approximately constant and complete the maneuver. When a hit is assumed to occur at constant angle of attack α instead of C_L, lower values of C_D^* can be anticipated as outlined in the appendix.

$$\Delta D \,\,\doteq\,\, 15{,}600\# \qquad \text{Lower bound}$$

$$\Delta D \,\,\doteq\,\, 33{,}150\# \qquad \text{Upper bound estimate}$$

A parameter study was made to determine the range of drag increments that could be expected, based upon the experiments of Reference 9 for a range of load factor 'n' and damaged area 'A' in terms of % wing area for three combat altitudes and a 600 mph true maneuvering speed. These results are presented in Table V and Figures 8 and 9.

2.2.3 Drag Divergence Aeroelastic Analysis

A flutter and divergence analysis to investigate the drag divergence failure hypothesis of the statistical fighter wing was conducted at sea level conditions for a range of aerodynamic damage expressed in terms of damage induced drag levels. The results of the study are summarized in Figures 10. Much of the analysis was conducted for no assumed structural damage, although several studies were also made where both structural and aerodynamic damage were considered. In developing a model for the structural damage studies, reference at this point is made to the comprehensive work by Biot and Arnold (Reference 1), which assesses the changes in the physical parameters of the wing such as its mass and stiffness that might be caused by ballistic damage. In that study only rigidity changes, and their secondary effects on inertia, due to a shift of elastic axis, were considered to be of practical significance. Since aircraft of this type were normally designed

to withstand loads up to 1.5 times the maximum static design loads, the structure should normally experience decreases in torsion (GJ) and bending rigidities (EI) of up to 45% and not undergo strength failure at its ultimate load factor. To model in detail the changes in structural parameters the two spar wing was idealized as illustrated below.
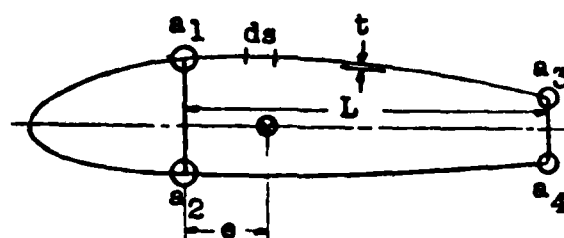
In the analysis of such a two spar wing it is common practice to neglect all of the material aft of the rear spar where the controls are generally located. Such a modeling indicates, for example, that even extreme damage patterns result in a movement of the elastic center of the wing by only 12.5% of the section semi-chord. A parametric study was conducted in Reference 1 to determine the shift that could be imposed on the wing elastic axis by ballistic damage. This study can be summarized by the following table:

Nature of Damage	Elastic Axis Location e			
Undamaged	13.90 in	aft	front	spar
Main torque box destroyed	13.68 in	"	"	"
50% decrease bending stiffness rear spar	11.02 in	"	"	"
Nose torque box destroyed	17.82 in	"	"	"
35% decrease bending stiffness front spar	16.07 in	"	"	"
Nose torque box destroyed and 35% decrease in bending stiffness front spar	19.28 in	"	"	"

One conclusion of Reference 1 was that shifts in the elastic axis of these magnitudes due to ballistic damage, which still left the structure with adequate static strength, would not significantly influence the flutter and divergence margins. Consequently in the present structural damage model only reductions of EI and GJ were applied locally in the damage area, to reflect ballistic damage to the structure. Since the wing structure of this typical fighter was of a two spar semi-monocoque construction, see Figure 2b, torque box destruction and GJ reduction would probably be easier to accomplish than reducing EI by removing spar cap material. For this reason the more representative damage cases are thought to be those involving larger GJ reductions than EI reductions. All of the structural damage cases are summarized in Table VI and four of the more significant data cases are plotted in Figures 10 continued.

26

During the flutter and divergence analysis of this wing, two
aerodynamic damage cases were considered. In one case, aerodynamic
damage induced drag was assumed localized at the 80% semi-span of the
wing in the area of the leading edge, while in the second case this
damage was moved to the 90% semi-span position. The basic wing modeling
employed an elastic thin beam structure described by the following
coupled system of equations similar to those employed in the thin beam
lateral buckling studies.*

$$\frac{\partial^2}{\partial x^2}\left(EI\,\frac{\partial^2 w}{\partial x^2}\right) + m\,\frac{\partial^2 w}{\partial t^2} + S_\alpha\,\frac{\partial^2 \beta}{\partial t^2} + \Delta D\,H(\xi - x)\left[(\xi - x)\frac{\partial^2 \beta}{\partial x^2} - 2\,\frac{\partial \beta}{\partial x}\right]$$

$$- L(\beta,w;x,t) = 0$$

$$\frac{\partial}{\partial x}\left(GJ_{eff}\,\frac{\partial \beta}{\partial x}\right) + I_\alpha\,\frac{\partial^2 \beta}{\partial t^2} + S_\alpha\,\frac{\partial^2 w}{\partial t^2} + \Delta D\,H(\xi - x)\left[(\xi - x)\,\frac{\partial^2 w}{\partial x^2}\right]$$

$$- M_{ea}(\xi,w;x,t) = 0$$

where

$$\Delta D = C_D^* Aq$$

(C_D^* = constant determined from experiment; A = 1/2 total entrance

plus exit hole area) and

*H(x) is the Unit Step Function, and was employed here to more compactly
write the beam equations that are valid to the right and left of the
concentrated load.

with

$$w = w_0(x) e^{i\omega t}$$

$$\beta = \beta_0(x) e^{i\omega t}$$

where

$$w_0(x) = \sum_{i=1}^{r} h_i f_i(x)$$

$$\beta_0(x) = \sum_{j=1}^{r} \beta_j F_j(x)$$

and $f_i(x)$, $F_j(x)$ are determined from normal vibration modes of structure, with h_i and β_j defined as complex coefficients.

In addition, the appropriate inertial and time dependent aerodynamic force terms were included, thus allowing a complete dynamic, but steady state, stability study. For the preliminary studies, in-compressible strip theory was also employed for the moderately high aspect ratio wings considered in the analysis.[*] Finally, a constant static parasite drag term was considered to be the significant or first order aerodynamic force caused by the damage.

---

[*]The cancelling of compressibility and finite span effects have tradi-tionally lead analysts to employ incompressible strip theory as a first simple estimate in aeroelastic stability studies. The Scanlan and Rosenbaum definition for aerodynamic lift and moment was employed here. See their text "Aircraft Vibration and Flutter", Dover 1968. See also Reference 1.

28

A Galerkin type solution of these equations for various levels of damage parasite drag resulted in the family of U-g and U-ω curves illustrated in Figure 11. The level of drag is seen to play an important role in the transition from a classical flutter critical instability for the undamaged wing to a critical drag divergence type of instability for the damaged wing (see also Figure 10). Interestingly enough, although only of academic concern, when divergence is critical, the actual flutter speed increases as a result of the added drag term. This is consistent with other findings in the literature for moderate aspect ratio undamaged wings. 3/ 4/ In the present study, the divergence becomes critical due to the high level of localized drag caused by the damage. The near frequency coalescence, characteristic of classical bending torsion flutter is eliminated or delayed by the tendency of the first mode frequency branch to approach zero frequency, thereby promoting divergence in the first mode branch prior to the occurrence of flutter in the torsion branch.

The results of the drag divergence and flutter analysis are presented in Figures 10. The influence of aerodynamic damage alone is illustrated in the first of Figures 10. This damage is in the form of drag only with 100% structural integrity assumed. Two aerodynamic damage cases are considered here. The first case locates the concentrated aerodynamic damage force at the 80% semi-span of the wing near the leading edge while the second case considers a drag load concentrated near the leading edge of the 90% semi-span position (Fig. 2a). This

29

aerodynamic damage mechanism alone is seen to significantly reduce
critical wing divergence speeds at the higher drag levels. In addition,
a trade off drag level occurs where divergence becomes more critical
than flutter. That is, the drag divergence speed is seen to reduce
monotonically with increased damaged induced drag levels. In contrast,
the flutter speed is shown to increase at the lower drag levels.
The significant influence of the semi-span location of the damage
site can also be seen from this figure. In addition, the more criti-
cal conditions are found at sea level conditions as expected. In spite
of the significant reductions in the critical divergence speeds of the
wing, aerodynamic damage alone is not sufficient to reduce these critical
speeds to within the flight envelope of our generic fighter wing for
reasonable damage induced drag levels. Consequently, several struc-
tural damage configurations were superimposed upon these aerodynamic
damage cases to further degrade the wing's drag divergence speeds.
These results are presented in Figures 10 continued. As indicated ear-
lier the structural damage was imposed by reducing the bending stiffness
EI and torsional stiffness GJ in the area of the local damage site. For
the damage located at the 80% semi-span, wing elements 4, 5 and 6 were
degraded in stiffness by the amount indicated in Figures 10. On the
other hand for the damage located at the 90% semi-span only stations
5 and 6 were reduced by the amount indicated. Those damage cases in-
volving larger GJ reduction than EI are thought to represent the more
realistic type damage cases.

To illustrate the plausible drag divergence failure mechanism, consider the fighter in a typical 5 'g' pull out maneuver at sea level conditions when a class 'A' or 'B' hit is received at a 600 mph maneuvering speed. Based upon the experiments of Reference 9 and Figure 8 one could anticipate a drag coefficient increment C_D^* anywhere from 1.7 to 3.8 depending upon the nature of the damage. Using a nominal value of 3.5 for C_D^*, Figure 9 demonstrates the development of a 30,000# drag load for hole type damage equal to 3% of the wing area or a 48,000# drag load for a 5% hole damage area.

The influence of a class 'A' or 'B' type hit on the structure is best illustrated by reference to Figure 2b. This illustrates the two spar semi-monocoque type structure representative of the statistical fighter wing. Reference to Table III indicates that a class 'A' or 'B' type hit would most likely disable the front two torque boxes significantly reducing the sectional torsional stiffness GJ. It also appears that part of the front spar cap would be removed reducing the section bending stiffness EI. From Figure 10 continued, for aerodynamic damage at the 80% semi-span, it is evident that one combination of aerodynamic and structural damage equivalent in area to 5% of the wing area and producing a 70% reduction in torsional and bending stiffness at stations 4, 5, and 6 would reduce the divergence speed of the fighter to approximately 600+ mph or to within its flight envelope. Another damage alternative occurs for an aerodynamic damage at the 90% semi-span and a resulting 70% reduction in torsional stiffness at stations 5 and 6 with only a 50% reduction in bending stiffness at these same stations. In

31

this case, a 42,000# drag load, caused by a 4 1/2% hole under a 5 'g'

pull out, will reduce the divergence speed to within the flight envelope.

This could also be accomplished by a 4% hole at the 90% semi-span for

the same pull out maneuver if not the average C_D^* but the upper limit of

$C_D^* = 5$ were allowed and similar reduction in EI and GJ retained. Other

tradeoffs are also possible, as is evident from Figures 8, 9 and 10 con-

tinued. Fighter aircraft wings of the category of our statistical model

are probably designed to a load factor of at least 8.00 to 8.67 with a 1.5

margin on strength under these conditions. 13/ In a 5 'g' pull out maneu-

ver, therefore, our fighter should have adequate strength even though its

EI and GJ have been reduced by 60% to 70% in the outer wing panels.

Some additional factors should be mentioned at this point con-

cerning the damage induced drag levels and the feasibility of promoting

a drag divergence mechanism. Based upon the findings of Reference 4 and

Figure 5, it is evident that the drag associated with the undamaged wing

will further reduce the computed divergence speeds. This has been neglected

in the present analysis but will further reduce the divergence boundaries

of Figures 10 into the flight envelope of the wing. In addition, only an

approximate allowance has been made up until now for pilot response to a

control input to compensate for the loss of lift on a damaged wing. The

response was assumed to be one of immediate aileron deflection downward on

the damaged wing to inhibit a rolling tendency of the aircraft once it is

hit and to maintain an approximately constant C_L to complete the maneuver.

This aileron deflection would probably introduce a slightly different induced

drag term on the damaged wing than that estimated by holding C_L constant.

This would modify the drag increment that was determined above and possibly

further enhance the drag divergence. Finally, the transient character of the damage occurrence and the resulting higher impulsive chordwise loading was also ignored and only the chordwise loading considered that resulted primarily from a steady drag load increase, localized at the damage site. In spite of these simplifications in the analysis, drag divergence appears to be a plausible mechanism of failure on damaged fighter aircraft wings undergoing high load factor maneuvers.

In summary a plausible aeroelastic failure mechanism due to warhead damage can be rationalized for certain classes of lifting surfaces when both aerodynamic and structural damage modeling are included. One or the other alone does not seem sufficient to initiate a failure mechanism. These results, therefore, are consistent with the findings of Reference 1 in that respect. That is, the present study recovers the critical flutter and divergence speeds of Reference 1 when aerodynamic damage is ignored and only structural damage is considered. Since the success of the proposed failure mechanism is strongly dependent upon an accurate assessment of aerodynamic damage in the form of damage induced drag increments, more experimental wind tunnel studies over and above the results of Reference 9 and the Appendix appear necessary. Further refinements in the aeroelastic modeling are also recommended to allow for the impulsive or explosive character of the damage induced drag force as it actually occurs during the warhead strike. 14/

33

3. POTENTIAL FLOW MODELING OF A THROUGH-HOLE
TYPE DAMAGE IN A LIFTING SURFACE

3.1 Program Description

A potential flow modeling of a surface with a through-hole
type damage was conducted utilizing an established lifting surface code
designed to minimize computational effort. Basically a kernel function
method with a multiple interference lifting surface option was utilized
to predict the steady load changes due to this aerodynamic damage. These
predicted loads are needed, for example, in an aeroelastic flutter,
divergence, or response analysis since such studies couple the structural
dynamic equations with the generalized loads or generalized aerodynamic
force terms.

An extensive literature search revealed that papers on the
analytical aerodynamic modeling of damaged lifting surfaces are very
limited in number. In addition, virtually no experimental studies have
been performed to aid the investigation on the aerodynamic modeling of
damaged lifting surfaces. Due to this lack of both analytical and experi-
mental investigations, a study was undertaken to determine the ability of
existing unsteady aerodynamic numberical codes to model damaged lifting
surfaces. A supporting wind tunnel study was also undertaken at the Uni-
versity of Texas to further aid this aerodynamic modeling evaluation.

3.2 Aerodynamic Modeling Methodology

There are numerous simplified methods available for predicting
the load or pressure distributions of lifting surfaces. Most of these

34

closed form classical methods have severe geometric limitations. Several numerical methods, however, are now available that can model three-dimensional lifting surfaces employing present day computers. Two of the most widely used techniques are the finite-element and collocation methods. Both methods solve the same integral equation but use different representations of the pressure distribution.

The finite-element method, often referred to as a vortex-lattice or doublet-lattice method, divides the lifting surface into numerous panels. It is assumed that the lift on each panel is represented by a horseshoe vortex whose bound segment is located at the panel quarter-chord. The downwash on each panel is induced by all horseshoe vortices in the system. The boundary condition of tangential flow (no flow through the wing) is applied at a select point (3/4 chord at mid-span) on each panel, where the total downwash has been calculated. Satisfaction of these boundary conditions leads to a set of simultaneous equations from which the unknown vortex strengths can be found. Accurate solutions require a large number of elements, hence unknowns for which the size and cost of the problem sometimes becomes prohibitive.

The collocation method represents the pressure distribution with an assumed pressure distribution function having unknown coefficients. The boundary condition of flow tangency is more nearly satisfied over the entire surface than the finite-element method. However, the assumed pressure function must be reasonably well-chosen for good convergence to the actual pressure distribution. The collocation method has fewer unknowns than the finite-element method, but requires special handling of the integral singularity at each collocation point.

A collocation method, specifically the N.A.S.A. trisonic kernel function method developed by A. M. Cunningham, was chosen as having a good potential to successfully model damaged surfaces for both steady and unsteady flows. The ability of the code to handle numerous interfering, non-planar surfaces, along with the versatility of the user selected pressure weighting functions, allows a large variation of damage types that can be handled.

3.3 The Kernel Function Method Utilized

The following is a brief discussion of the "N.A.S.A. kernel function method" subsonic solution technique as outlined by Cunningham. References 15-18 contain detailed descriptions of the solution process, and also discuss the supersonic and transonic regimes.

The integral equation to be solved is derived from the acceleration potential. This equation relates the downwash (normal velocity) and the lift distribution in the following manner

$$\frac{\bar{w}_p}{U}(\tilde{x}, \tilde{y}, \tilde{z}) = \frac{A}{U} \sum_{q=1}^{Q} \iint_{S_q} \Delta\bar{p}_q(\tilde{\xi}, \tilde{n}, \tilde{\zeta}) K(\tilde{x}_0, \tilde{y}_0, \tilde{z}_0, k, M) d\tilde{\xi} \, d\tilde{n}$$

where

$$\tilde{x} = \frac{x}{b_{ref}}$$

$$\tilde{y} = \frac{y}{b_{ref}}$$

$$\tilde{z} = \frac{z}{b_{ref}}$$

b_{ref} = reference length

$x_0 = x - \xi$

$y_0 = y - \eta$

$z_0 = z - \zeta$

k = reduced frequency $\left(\frac{\omega b_{ref}}{U}\right)$

U = free stream velocity

ω = frequency, rad/sec

A = constant = $\frac{1}{4\pi\rho U}$

Q = total number of surfaces

$\bar{w}$ = downwash amplitude

S = integration area

K = kernel function

$\Delta\bar{p}_q$ = pressure difference amplitude at point $\tilde{\xi}, \tilde{\eta}, \tilde{\zeta}$, on the qth surface

The downwash, $\dfrac{\bar{w}_p}{U}(\tilde{x}, \tilde{y}, \tilde{z})$, on the pth surface, is expressed as

$$\frac{\bar{w}_p}{U}(\tilde{x}, \tilde{y}, \tilde{z}) = \frac{-8\pi}{U}\left(\frac{\partial h}{\partial \tilde{x}} + ikh\right)_p$$

where

$$h = h(\tilde{x}, \tilde{y}), \text{ modal displacement at point } \tilde{x}, \tilde{y}.$$

The kernel function, $K(\tilde{x}_0, \tilde{y}_0, \tilde{z}_0, k, M)$, is simply the downwash at point $\tilde{x}, \tilde{y}, \tilde{z}$ due to a unit load at point $\tilde{\xi}, \tilde{n}, \tilde{\zeta}$ (Figure 12). For steady flow, the kernel function may be expressed as

$$K(\tilde{x}_0, \tilde{y}_0, \tilde{z}_0, 0, M) = -\frac{1}{\tilde{y}_0^2}\left[1 + \frac{\tilde{x}_0}{\sqrt{\tilde{x}_0^2 + \beta^2\tilde{y}_0^2}}\right]$$

The two methods of solution of the integral equation, as previously noted, are the finite-element method whereby a wing is panelled with small elements loaded with horseshoe vortices of unknown strengths, and the collocation method of assumed pressure distribution functions with unknown coefficients. The "N.A.S.A. kernel function method" is a collocation method applicable to multiple surface configurations.

For a single planar subsonic surface (Figure 16), the pressure distribution function for a collocation method takes the following general form

38

$$\Delta p_q(\tilde{\xi}, \tilde{\eta}) = \frac{1}{2} \rho U^2 \sqrt{1 - \left(\frac{\tilde{\eta}}{\tilde{S}_0}\right)^2} \sqrt{\frac{\tilde{x}_{TE} - \tilde{\xi}}{\tilde{\xi} - \tilde{x}_{LE}}} \left[a_1 + a_2\tilde{\xi} + a_3\tilde{\eta} + a_4\tilde{\xi}\tilde{\eta} + \ldots\right]$$

in which the unknown a_j coefficients are to be determined.

Substituting this expression into the integral equation yields

$$\frac{\bar{w}_p}{U}(\tilde{x}, \tilde{y}) = \sum_{q=1}^{Q} \frac{1}{8\pi} \int_{-\tilde{S}_0}^{+\tilde{S}_0} \int_{\tilde{x}_{LE}}^{\tilde{x}_{TE}} \sqrt{1 - \left(\frac{\tilde{\eta}}{\tilde{S}_0}\right)^2} \sqrt{\frac{\tilde{x}_{TE} - \tilde{\xi}}{\tilde{\xi} - \tilde{x}_{LE}}}$$

$$\cdot \left[a_1 + a_2\tilde{\xi} + a_3\tilde{\eta} + a_4\tilde{\xi}\tilde{\eta} + \ldots\right] K(\tilde{x}_0, \tilde{y}_0, k, M)_{qp} \, d\tilde{\xi} \, d\tilde{\eta}$$

The influence of the pressure function j on the downwash value at the $(x, y)_i$ point is defined to be

$$A_{i1} = \frac{1}{8\pi} \int_{-\tilde{S}_0}^{+\tilde{S}_0} \int_{\tilde{x}_{LE}}^{\tilde{x}_{TE}} \sqrt{1 - \left(\frac{\tilde{\eta}}{\tilde{S}_0}\right)^2} \sqrt{\frac{\tilde{x}_{TE} - \tilde{\xi}}{\tilde{\xi} - \tilde{x}_{LE}}} \, K(\tilde{x}_{0_i}, \tilde{y}_{0_i}, k, M) \, d\tilde{\xi} \, d\tilde{\eta}$$

$$A_{i2} = \frac{1}{8\pi} \int_{-\tilde{S}_0}^{+\tilde{S}_0} \int_{\tilde{x}_{TE}}^{\tilde{x}_{LE}} \sqrt{1 - \left(\frac{\tilde{\eta}}{\tilde{S}_0}\right)^2} \sqrt{\frac{\tilde{x}_{TE} - \tilde{\xi}}{\tilde{\xi} - \tilde{x}_{LE}}} \, \tilde{\xi} \, K(\tilde{x}_{0_i}, \tilde{y}_{0_i}, k, M) \, d\tilde{\xi} \, d\tilde{\eta}$$

$$A_{i3} = \frac{1}{8\pi} \times \int_{-\tilde{S}_0}^{+\tilde{S}_0} \int_{\tilde{x}_{LE}}^{\tilde{x}_{TE}} \sqrt{1 - \left(\frac{\tilde{\eta}}{\tilde{S}_0}\right)^2} \sqrt{\frac{\tilde{x}_{TE} - \tilde{\xi}}{\tilde{\xi} - \tilde{x}_{LE}}} \; \tilde{\xi} \, \tilde{\eta} \; K(\tilde{x}_{0_i}, \tilde{y}_{0_i}, k, M) \, d\tilde{\xi} \, d\tilde{\eta}$$

.   .

.   .

.   .

such that

$$w_i = \sum_{j=1}^{J} A_{ij} \, a_j$$

Satisfying the above equation at J downwash points leads to the matrix equation to be solved for J unknown coefficients

$$\left[A_{ij} \right] \left\{ a_{ij} \right\} = \left\{ w_i \right\}$$

or

$$\left\{ a_{ij} \right\} = \left[A_{ij} \right]^{-1} \left\{ w_i \right\}$$

The collocation points are optimally selected as roots of Tschebyshev polynomials of the second kind such that

$$x_i = -\cos\left(\frac{2i}{2\bar{m} + 1} \pi\right) \qquad i = 1, 2, \ldots \bar{m}$$

40

and

$$y_r = -\cos \frac{\pi r}{R+1} \qquad r = 1, 2, \ldots R$$

where

$\bar{m}$ = number of chordwise collocation points

R = number of spanwise collocation points

The actual planform, then, is transformed into a square plane such that

$$\underline{x} = (\tilde{x} - \tilde{x}_m(\tilde{y}))/b(\tilde{y})$$

$$\underline{y} = (\tilde{y} - \tilde{s}_0)/\tilde{s}_0$$

where $\tilde{x}_m$ is the 1/2-chord.

By defining the collocation points at these locations, the integrated subsonic lift will be exact for $w(x)$ described as a polynomial of order $\bar{m} - 1$ or less in the chordwise direction. The same is true in the spanwise direction for $w(y)$ of order $R - 1$ or less. Note that for $\bar{m} = 1$, the location of the collocation point becomes the classical 3/4-chord point.

The pressure distribution may be redefined for a general multi-surface configuration (Figure 12) in the transformed coordinates as

41

$$p_q(\xi,\underline{\eta}) = \frac{4\rho U^2}{b_q(\underline{\eta})} S_{0_q} h(\xi)l(\underline{\eta}) \left[g_{0_q}(\underline{\eta})f_0(\xi) + g_{1_q}(\underline{\eta})f_1(\xi) + \ldots \right]$$

where

$\xi,\underline{\eta}$ = integration point location in the transformed coordinates

$b_q(\underline{\eta})$ = local semichord at span station $\underline{\eta}$

S_{0_q} = semispan

$h(\xi)$ = chordwise weighting function

$l(\underline{\eta})$ = spanwise weighting function

$g_{n_q}(\underline{\eta})$ = $a_{0_{n_q}} U_0(\underline{\eta}) + a_{1_{n_q}} U_1(\underline{\eta}) + \ldots$

$f_0(\xi) = U_0(\xi) = 1$

$f_1(\xi) = U_1(\xi) + U_0(\xi) = 2\xi + 1$

$\vdots \qquad\qquad \vdots$

$f_n(\xi) = U_n(\xi) + U_{n-1}(\xi)$

$U_n(\xi)$ = Tschebyshev polynomials of the second kind.

The weighting functions, $h(\xi)$ and $l(\underline{\eta})$, are selected from Figure 13
with some restrictions depending on the flow conditions and type of
surface or damage.

The kernel function integral equation may be rewritten as

$$\bar{w}_p(x,\, y,\, z) \;=\; \sum_{q=1}^{Q}\left\{ \int\!\!\int_{S_q} \left[\frac{S_{o_q}}{b_q(\underline{n})}\, h(\underline{\xi})\, l(\underline{n}) \sum_{n=0}^{\bar{m}-1} f_n(\underline{\xi}) \sum_{m=0}^{R-1} a_{mn_q} U_m(\underline{n}) \right] \right.$$

$$\left. K(\tilde{x}-\tilde{\xi},\; \tilde{y}-\tilde{n},\; \tilde{z}-\tilde{\zeta},\; k,\; M)_{qp}\; d\tilde{\xi}\, d\tilde{n} \right\}$$

where the kernel is evaluated in the actual planform coordinates.

Separating the double integral into a chordwise and spanwise integral, we may write

$$A_{mn_{pq}} \;=\; S_{o_q} \int_{\tilde{y}_a}^{\tilde{y}_b} \frac{l(\underline{n}) U_m(\underline{n})}{b_q(\underline{n})} \left\{ \int_{\tilde{x}_{LE}}^{\tilde{x}_{TE}} h(\underline{\xi}) f_n(\underline{\xi}) K(\tilde{x}-\tilde{\xi},\; \tilde{y}-\tilde{n},\; \tilde{z}-\tilde{\zeta},\; k,\; M)_q d\tilde{\xi} \right\} d\tilde{n}$$

where $\tilde{y}_a$, $\tilde{y}_b$ = left and right hand wing tips including the image surface if necessary.

The chordwise integral is evaluated with a Tschebychev-Gaussian Quadrature integration formula with the integration points located such that interdigitation is maintained between the integration and collocation points (Figure 14) thusly,

$$\xi_j \;=\; -\cos\left(\frac{2j-1}{2J+1}\,\pi\right) \quad j = 1,\, 2,\, \dots\, J$$

$$J = \text{number of chordwise integration points}$$

$$= \text{INT}[n(\bar{m}+1/2)] \text{ for } n = 1,\, 3,\, 5,\, \dots$$

43

Evaluation of the spanwise integral, being an improper integral, is more difficult. Expansion of the integrand in a Taylor series and evaluation of the terms by a special quadrature integration formula and an analytic evaluation with correction terms added is necessary. Optimally locating the spanwise integration points such that interdigitation is maintained, we may write

$$\underline{\eta}' = - \cos (\frac{2s - 1}{2S'} \pi) \quad \text{for } s = 1, 2, \ldots S'$$

where $S' = n(R + L)$ for $n = 1, 2, \ldots$

A further spanwise coordinate transformation, described in detail in Reference 17, is made to insure that the integration chords are grouped symmetrically and more densely about the downwash chord (Figure 15). The chordwise integral at the integration chords nearest to the down-wash chord is evaluated with an additional number of integration points so that the accuracy of the chordwise integral is consistent with that of the spanwise integral in the critical region.

3.4 Through-Hole Aerodynamic Damage Study

Before modeling the damaged lifting surface, a baseline configuration or undamaged model was established for a reference. The planform geometry of Figure 16, exhibiting moderate sweep angles, is typical of several modern fighter-type aircraft, and was modeled as an undamaged single surface wing at a Mach number of 0.24.

As mentioned previously, the present study is designed to aid in the aeroelastic modeling of damaged lifting surfaces. Consequently, predicting the generalized aerodynamic forces of damaged surfaces is of more direct concern than the pressure distributions themselves. To obtain a measure of the ability to predict these forces on damaged surfaces, integrated parameters such as C_{L_α}, X_{cp}, and Y_{cp} were employed as a final standard of measure. The "N.A.S.A. kernel function code" has numerous input options available which must be investigated before a best solution procedure can be established. 18/ The number of collocation points (control points) and their distribution, within the program limits, along with the selection of the assumed pressure distribution weighting functions, are two options to be carefully considered. A parameter study of these two options was performed on the planform of Figure 16 to determine the baseline solution.

The importance of the proper selection of pressure weighting functions was found by holding the number of control points constant and selecting reasonable combinations of chordwise and spanwise weighting functions. Six chordwise and six spanwise control points were selected in order to allow for a relatively high order model. Figures 17-21 present chordwise pressure coefficients at three span stations, running lift, and the center of pressure variation along the span. The following abbreviations were employed in the figures:

45

NC = number of chordwise control points

NS = number of spanwise control points

YP = 2Y/B = fraction of semispan, where

$\qquad$ YP = 0.00 at wing root

$\qquad$ YP = 1.00 at wing tip

$$\Delta CP = \frac{P_{\ell} - P_u}{q}$$

X/C = fraction of local chord

IC = chordwise pressure weighting function (Figure 13)

LS = spanwise pressure weighting function (Figure 13)

CLC/CAVG = lift coefficient based on local chord nondimension-alized by average chord of wing

XCP = chordwise center of pressure nondimensionalized by b_{ref} = 23.46"

IS = 2: symmetric surface used in all cases (Figure 13)

Good convergence is seen for the case of IC = 1 and LS = 3, which is the choice Reference 18 outlines as being the best behaved solution. The choice of IC = 3 and LS = 3 also yields a good solution, except near the wing tip. Choices of IC = 2 and IC = 4 are poor selections since they require considerable alteration to achieve the correct solution which requires a leading edge pressure singularity and a Kutta condition at the trailing edge. This large alteration results in oscillations about the better solutions and points out the importance of selecting weighting functions that approximate the solution as closely as possible.

Proper control point selection can also be investigated in a similar manner. Using the weighting functions of IC = 1 and LS = 3, the baseline data was determined by varying the number and distribution of control points. Solutions were obtained for six different control point cases maintaining an equal number of chordwise and spanwise points, and for three cases in which the number of spanwise points was greater than the number of chordwise points. Figures 22-26 present pressure coefficients, running lift, and center of pressure plots for the first six cases of equal chordwise and spanwise control points. The cases of NC = NS = 4, NC = NS = 5, and NC = NS = 6 show good convergence all the way to the wing tip. Table VII summarized the nine different cases and indicates more sensitivity to chordwise control point selection than spanwise selection. Figure 26 shows excellent comparison of center of pressure location for cases D and F at the wing root, while at the wing tip only case F is seen to approach the desired solution. From the ΔC_{L_α} column of Table VII we also see convergence toward case F, which was chosen as the baseline data.

A damaged model was formulated by dividing the planform into eight lifting surfaces surrounding the damage hole as shown in Figures 27 and 28. A trapezoidal damage area of 1% of the wing area (not including the image surface) was located at the wing quarter-chord and three-quarter semispan to simulate damage in a high drag location ideal for inducing drag divergence. Although true damage is not trapezoidal, the "N.A.S.A. kernel function method" requires trapezoidal

47

lifting surfaces, which were divided by constant chord lines of $\frac{x}{c} = 0.179$ and $\frac{x}{c} = 0.321$. An undamaged model can then be formulated by the addition of a ninth lifting surface, replacing the damaged area, as seen in Figure 29. Because the "N.A.S.A. kernel function method" does not directly satisfy any pressure continuity conditions between lifting surfaces, the nine surface undamaged model is required for a true comparison with the 8 surface damaged model. By finding the nine surface undamaged solution which closely correlates with the single surface undamaged solution, the damaged surface can be removed to give a true indication of the effects of a hole. This model allows a Kutta condition to be imposed on both sides of the hole and the trailing edge of surface 4, along with a singularity at the leading edge of surface 5, which is consistent with potential flow thin-wing theory. Symmetrical flow was assumed (IS = 2), which allows the image surface to be damaged also, since this would be the case for a side wall tunnel installation where the tunnel wall acts as a reflecting plane.

A convergence study was performed on the nine surface undamaged model by incrementally increasing the number of control points on each surface. The number of points and their distribution in each surface is tabulated in Table VIII for each case run, while Table IX lists the pressure weighting functions chosen for each surface. Note that the overall planform still maintains a no-load (Kutta) condition on the wing tip and trailing edge, and a leading edge singularity. Figures 30-37 present the control point layouts for each case on the

48

wing planform, which allows an important visual check of the distributions. A corresponding convergence study was then performed on the damaged model by removing the appropriate surface and imposing the Kutta condition on the front, left, and right edges of the hole and introducing the leading edge singularity to surface 5 of the damaged model. The pressure weighting functions chosen are presented in Table IX for comparison with the undamaged model weighting functions. Table X summarizes the data generated by the convergence study where initially, cases 1-6 and 1D-6D were run to obtain a base of data which was reviewed to provide information for the remaining cases. Undamaged cases 1-6 appear to converge toward case 5, with the exception of case 2 which appears to be a decent solution even though relatively few control points were used. Case 2 was modified to yield cases 8 and 9, of which case 8 appears to be a good solution.

Case 5, utilizing the control point arrangement of Figure 34, was used for a closer look at the effects of a damage hole since it compared quite well with the single surface solution of case F. Figures 38-40 compare chordwise pressure coefficient differences, at three span stations, for the single surface undamaged case F and the 9 surface undamaged case 5. Note the discontinuities between the surfaces, which arises since no mechanism in the program is currently available to directly invoke continuity conditions between surfaces. The choice of two control points in the chordwise direction and a constant pressure weighting function leads to a linear variation of

49

load for surfaces 2, 5, and 8. For the other surfaces the load
variations are of higher order. Figure 41 gives a visual check of the
span stations for which the damaged case 5D and undamaged case 5 are
compared in Figures 42-49. The discontinuities, of course, still
exist, but it can be seen that the pressure disturbance is largely
attenuated in approximately one hole width on either side of the damage
area. Figures 45 and 46, located on the hole, show the Kutta condi-
tion imposed upon the trailing edge of surface 4, and also shows the
leading edge singularity of surface 5. Figures 50-52 compare the
running lifts of cases F, 5, and 5D where it can be seen that spanwise
discontinuities also exist. The choice of two control points along
with the choice of a constant pressure weighting function leads to
a linear variation of load in the spanwise direction for surfaces 4
and 5. The Kutta conditions on the sides of the hole drive the lift
down in the vicinity of the hole, and this overall effect of a loss
of lift can easily be seen. Figure 50 shows a slight disagreement
between the two undamaged surface models near the wing root chord.
Although this is not yet clearly understood, it does emphasize the
desire to compare both damaged and undamaged configurations employing
the multi-surface modeling. Releasing the Kutta conditions and sin-
gularity on the hole, i.e. case 7D which uses the same weighting
functions as the undamaged case, provides a slight increase in lift,
as shown in Table X and Figures 53-55. This method, which allows the
program to seek its own load levels surrounding the hole, does not

50

give realistic data, as is best seen by Figure 55.

Case 8, using only 45 control points, also compared favorably with case F. Case 8 utilizes a better control point distribution than case 5, where a consistent and evenly distributed arrangement is desired. Using only one chordwise control point on high aspect-ratio surfaces requires an additional number of chordwise integration points to achieve a converged solution. For this reason, the default value of one was overridden and four chordwise integration points used to maintain the appropriate interdigitation between control and integration points. Figures 56-58 present pressure coefficient differences, at three span stations, comparing the undamaged single surface solution (case F) with the undamaged solution of case 8. For one control point and the selection of a constant chordwise pressure function, the result is a constant load; however, we see that the constant load over this surface is the mean load as predicted by case F. Figure 59 visually displays the locations of the six span stations for which pressure coefficient data is presented in Figures 60-65. Pressure discontinuities still exist and the hole disturbances are again largely attenuated by approximately one hole width on either side of the damage. Figures 66-68 present running lift plots for cases F, 8, and 8D. The constant load segment is again the result of one control point and a constant spanwise pressure weighting function for the appropriate surfaces. Figure 67 indicates a loss in lift throughout most of the wing surface, with the greatest loss in the vicinity of the hole, as expected.

Comparison of Figures 51 and 67 indicate general agreement between the two configurations. While case 5 is a higher order model than case 8 in the sense that it utilizes more chordwise and spanwise control points in the critical region, these control points are not as well distributed across the planform as desired. Case 8 makes use of fewer control points distributed properly to achieve a slightly improved result. This emphasizes the difficulties that may be encountered when one attempts to indiscriminately locate a large number of control points in a region of discontinuity hoping to recover a more accurate solution of the local phenomenon.

A simplified model of the planform can be formulated by dividing it into 5 surfaces for the undamaged model and 4 surfaces for the damaged model, as shown in Figures 69 and 70 respectively. This model eliminates the chordwise discontinuities and allows a smooth curve to exist from the leading edge to the trailing edge. A control point distribution similar to case 8 was selected (Figure 71) with the pressure distributions listed in Table XI. Note that although a singularity may exist for surface 3, a Kutta condition may be imposed only on the front of the hole and not on the sides. Pressure coefficient differences and running lifts are presented in Figures 72-77, where little improvement over case 7D can be seen. Table XII shows a 1.5% increase in lift due to damage which is consistent with cases 7D and 10D. Again, lack of Kutta conditions yield an unrealistic solution.

A review of Table X emphasizing cases 5 and 8, which are
the best converged solutions, illustrates the aerodynamic changes,
as predicted by potential flow modeling, that a 1% through-hole type
damage may have on a simulated fighter wing. The hole was located
in a region critical to drag divergence of the wing. It is seen that
the total lift of the surface is reduced by approximately 5% while the
center of pressure may shift forward by 1/2% to 1%. In view of this,
one might anticipate a change on the order of 5% in the classical
generalized aerodynamic forces in an aeroelastic analysis. These
changes in generalized lift and moment forces are probably second
order when compared to the generalized forces introduced by the drag
changes resulting from the 1% hole type damage.* Thus, in an aero-
elastic analysis of damaged lifting surfaces, incremental drag effects
due to damage may be more important than lift and moment changes
due to through-hole damages of the order of 1-2% of the wing area.

3.5 Modeling Results

It has been shown that the "N.A.S.A. kernel function method"
consistently predicts a 5 to 6 per cent loss of lift for a trapezoidal
damage hole, located near the wing tip, having an area of 1% the local
wing area. A Kutta condition must be imposed on the sides and forward
edge of the hole and special attention paid to the location and dis-
tribution of the downwash and integration points; especially for the

---

*See Section 2.2.1

high aspect ratio sub-surfaces. The "N.A.S.A. kernel function method" contains some inherent handicaps that restrict its ability to model damage holes in detail. Because no continuity conditions are satisfied between lifting surfaces, pressure discontinuities exist between surfaces. Inconsistent pressure weighting function values often exist at the damage corners in order to satisfy the required Kutta conditions on the hole. This is the case at the junctions of the sides and aft edge of the hole, where a Kutta condition is input for the sides and a singularity input at the aft edge. These discontinuities are inherent to a kernel function approach and necessitate a macro-scale only study of the damage hole; that is, a loads analysis in lieu of a detailed pressure analysis. Further study incorporating wind tunnel tests and finite-element modeling, such as doublet-lattice, would provide a better understanding of the near-field effects of a damage hole and allow a data base to be compiled for future reference. Incorporation of induced-drag calculations to the "N.A.S.A. kernel function method" and comparison with wind tunnel data would allow realistic estimates to be made of flutter and divergence margins due to aerodynamic damage.

4. EXPERIMENTAL WIND TUNNEL PROGRAM

The experimental phase of the effort is intended to supply data for evaluation of the computer methods of predicting surface pressure distributions for damaged lifting surfaces. The initial study of the possible modes of aeroelastic failure induced by damage revealed that increases in drag resulting from damage were likely to be an important factor. The original experimental program was thus modified slightly by adding provisions for the direct measurement of lift and drag, to a limited extent. Although lift can, in principle, be obtained from the integration of surface pressures, this cannot be done with any acceptable accuracy for the drag of damaged configurations. These lift and drag forces will actually be measured on a force type wind tunnel balance.

4.1 Model Design and Construction

The entire study is directed primarily toward the effects of damage on high-performance aircraft, i.e. those designed for supersonic flight. Such aircraft are characterized by swept leading edges and thin airfoil sections. In selecting a model for the wind tunnel tests, consideration was given to the construction of a model with generally "typical" characteristics and to the alternative of use of an actual aircraft horizontal stabilizer. The advantage of using a production stabilizer was that the construction method, tolerances, finish and stiffness would automatically be present in the test "model". A survey of the size and availability through surplus of slab-type stabilizers

55

(no separate elevators) characteristic of supersonic aircraft led to the selection of the T-38 stabilizer which was small enough to fit in the wind tunnel.

The T-38 stabilizers are each mounted in the aircraft via a single torque tube; these are designed such that the left-stabilizer tube slides into the right-stabilizer tube, with through-bolts joining them into a single unit. The axis of this combined torque tube is perpendicular to the longitudinal centerline of the fuselage. However, the aft fuselage is slightly boattailed, with the result that the root rib of the stabilizer is not perpendicular to the torque tube. For mounting on the flat tunnel side wall, it was necessary to add a wedge-shaped extension at the root, as shown in Figure 78, where the original root is indicated by the dotted line. This addition was made using a foamed-in-place urethane which was given a smooth finish of the proper contour with a filler putty. The extension is barely evident in Figure 79a.

The stabilizer is of aluminum honeycomb construction with a bonded skin and a single main spar at 52.7% chord. Examination of a damaged stabilizer led to the conclusion that it would be impractical to attempt to remove one skin surface and channel the honeycomb to install pressure taps. It was not thought that delamination of the skin and subsequent re-attachment would maintain adequate strength or proper surface contour. Consequently it was decided to run the stainless steel pressure tubing along the outside of the lower-side skin and thence through the stabilizer to orifices on the upper surface. Since the

airfoil section is symmetrical, positive and negative angles of attack would supply equivalent data for the upper and lower surfaces. The stabilizer has a slight negative dihedral (4°), but it was predicted that the effect of this on symmetry would be small.

A total of 150 pressure taps were installed at locations as shown in Table XIII. The computer study of the problem was based on damage at 75% of the semispan, hence there is a concentration of pressure taps in this region to measure the effects of damage. The tap locations were laid out on the upper (test) skin and drilled with a 0.813 mm diameter drill; at each position a 4.76 mm hole was drilled from the lower surface, through the honeycomb to the back of the test skin (Figure 79b). A brass cylinder was soldered to each stainless steel pressure tube, as shown in Figure 80a; this cylinder was in turn cemented to the inner side of the test skin using a removable wire for alignment and to keep the tube clear. The stainless steel tubes were then bent to lie flat on the lower skin, leading first to the main spar and then along the spar to the torque tube as seen in Figure 79b. In the solid leading edge of the stabilizer, a 1.27 mm hole was drilled to intersect the 0.81 mm orifice hole and the steel tubing was cemented directly into the larger hole without using a brass cylinder (Figure 79b). After all the steel tubes were in place, they were cemented to the lower-surface skin, with filler putty being used to fair them with the surface as seen in Figure 79a. Strain gages were mounted on the torque tube at two axial locations as seen in Figure 80b; two 4-arm bridges

57

were located in the "horizontal" plane and two in the "vertical" plane, to measure normal and axial forces directly.

4.2 Model Installation and Instrumentation

The stabilizer was mounted through the right sidewall of the tunnel which simulated the aft fuselage for the left stabilizer half which was tested (Figure 81a). The torque tube was supported outside the tunnel by two pillow blocks which were in turn mounted on the stand seen in Figure 81b. A lever arm and lead screw were used to set angle of attack, which was indicated by a goniometer mounted on the lever arm. The gap between the torque tube and the tunnel wall was sealed with a flexible rubber gasket.

The pressure measurements were made using Scanivalve pressure multiplexers and DRUCK pressure transducers.* The transducer outputs were read and recorded by a Hewlett Packard 3052A data acquisition system which controlled the pressure multiplexers and calculated the pressure coefficients as well. The strain gage outputs were processed by Vishay 2110 signal conditioners with recording and data reduction via the data acquisition system.

4.3 Wind Tunnel Facility

The subsonic wind tunnel is of the open circuit type with atmospheric intake and discharge, having a 1.52 by 2.13 m (5 x 7 ft) test section. The drive system comprises four fans of 200 hp each,

---

DRUCK model PDCR differential pressure transducer PDCR CR-22, ±1PSI range.

mounted in parallel, with fine speed control through variable inlet vanes during each run. The fan blade angle is adjustable between runs for coarse speed changes. The test technique consisted of setting the model at the desired angle of attack, and initiating the automatic data acquisition system. The system was programmed with appropriate delays to allow pressure stabilization each time the pressure multiplexer was stepped. Six readings were taken and averaged for each data point to help minimize the effect of transients in the system.

The 65A004 airfoil section of the stabilizer has a sharp leading edge and thus is subject to leading edge separation. Such separation was observed in two-dimensional tests at angles of attack near and above 4°, as reported in Reference 21. During the current tests with the T-38 stabilizer, it was noted that the repeatability of the pressure coefficient data was poor, even at angles of attack near zero. Since the data for the undamaged stabilizer will serve as a base reference for the various damage configurations, the latter tests were deferred in order to better define the reference case. The output voltage from one pressure-multiplexer transducer was observed using a strip-chart recorder. Figure 82 shows a typical trace for one chordwise row of pressure taps, where the least division is 1.50 seconds; it is evident that unsteady flow exists near the leading edge, with the fluctuations becoming smaller as the distance from the leading edge increases. Similar traces of the tunnel pitot and static pressures showed negligible variation, and repeatability of the tunnel Mach number was good. It was therefore concluded that the

unsteadyness in flow is not caused by the tunnel but is present only near the stabilizer leading edge. This phenomenon is presently being studied in greater detail, because of its obvious ramifications for the aeroelasticity studies. References 19 and 20 report similar unsteadyness, but at higher angles of attack where it is attributed to leading edge separation.

4.4 Results of Experimental Study

The current experimental effort is being concentrated on an investigation of the unsteady flow which has been observed near the leading edge of the stabilizer. Such unsteadyness has been observed in two-dimensional tests by NACA, which attributed it to leading edge separation; in those tests, however, it was not noted at angles of attack below about 4 degrees, whereas in the present work it is evident even at zero angle of attack. Several flow visualization techniques will be used to determine the nature and extent of the separation and the effect of the sweep and low aspect ratio of the stabilizer being tested. Electronic filters are being tested as a means of obtaining steady, repeatable pressure and force data, for the undamaged configuration. These reference data are critical, since any uncertainties present will also appear when determining the effects of damage.

A complete set of force and pressure data, at 20 angles of attack, can be taken in half a day of tunnel operation. Once the solution is selected for the unsteady-flow problem, the data for the

60

damaged surfaces can be obtained in a few weeks. The pressure data
will be used to define the influence of damage on the stabilizer lift
distribution, and the force data will be used in the aeroelasticity
analysis to refine the results which are now based on approximate aero-
dynamic force data.

TABLE I

STATISTICAL FIGHTER PROPERTIES DETERMINED AS
GEOMETRIC MEAN OF FOLLOWING
FIGHTER AIRCRAFT

Service Designation	Manufacturer
P-51A	North American
XP-60	Curtiss-Wright
XP-84	Republic
XFJ-1	North American
XF8F-1	Grumman
XF9F-2	Grumman
F9F-3	Grumman
XFD-1	McDonnell
F2H-1	McDonnell
XF2D-1	McDonnell
XF6F-1	Grumman
XBT2D-1	Douglas
XF3D-1	Douglas
XF6U-1	Chance-Vought

Parameter X_g of typical fighter determined as geometric mean of similar parameters X_1, X_2, etc. of above aircraft. That is

$$X_g = (X_1 \cdot X_2 \cdot X_3 \cdot ----X_m)^{1/m}$$

where X_1, X_2, $----X_m$ represent the set of variates.

The specific typical wing parameters determined were

Weight.	Chord length.
Static moment about a reference axis.	Chordwise center of gravity position.
Bending area moment of inertia.	Chordwise elastic axis position.
Mass moment of inertia about a reference axis.	
Coefficient of torsional rigidity.	

62

TABLE II

TYPICAL DATA SHEET FOR DETERMINATION OF PARAMETERS FOR
REPRESENTATIVE AIRPLANE - CLASS I

Weight Distribution - Wing

STATION	1		2		3		4		5		6	
MODEL	W#	W_1/W_5	W#	W_2/W_5	W#	W_3/W_5	W#	W_4/W_5	W#	W_5/W_5	W#	W_6/W_5
P-51A	539	9.38	454	7.90	271	4.71	153.	2.66	57.5	1.0	51.9	.903
XP-60	964	7.90	636	5.21	411	3.37	337.	2.76	122.	1.0	41.7	.342
XP-84	1150	7.10	580	3.58	502	3.10	262.	1.62	162.	1.0	148.	.914
XFJ-1	302	2.72	249	2.24	189	1.70	119.	1.07	111.	1.0	68.8	.620
XF8F-1	341	8.33	283	6.92	254	6.20	99.2	2.43	40.9	1.0	25.9	.633
XF9F-2	431	5.20	287	3.46	107	1.29	90.8	1.10	82.9	1.0	65.5	.790
F9F-2,3	365	3.48	311	2.96	140	1.33	111.	1.06	105.	1.0	-	-
XFD-1	1158	16.1	314	4.37	121	1.68	80.	1.13	71.9	1.0	49.6	.690
XF2D-1	176	2.70	211	2.73	240	3.10	104.	1.34	77.4	1.0	69.9	.903
F2H-1	398	2.86	543	3.91	545	3.92	187.	1.35	139.	1.0	90.1	.648
XF6F-1	510	5.63	508	5.61	419	4.63	185.	2.04	90.6	1.0	73.4	.810
XBT2D-1	374	3.67	219	2.15	245	2.40	147	1.44	102.	1.0	80.2	.786
XF3D-1	445	4.08	497	4.56	392	3.60	169.	1.55	109.	1.0	83.4	.765
XF6U-1	407	6.24	230	3.53	129	1.98	83.8	1.29	65.2	1.0	82.4	1.26
REP. AIRPLANE	473	5.26	352	3.91	247	2.74	138.	1.53	90.	1.0	66.	.733

63

TABLE II Cont'd.

Wing Parameters - Representative Airplane - Class I

Station Parameter	1	2	3	4	5	6
Weight - #	473.	352.	247.	138.	90.	66.
I_{α_i} - # in.^{2} · 10^{-4}	25.8	15.6	8.78	4.81	2.855	1.73
S_{α_i} - # in. · 10^{-3}	2.641	.728	1.133	.900	.536	.379
EI_i - # in.^{2} · 10^{-8}	67.05	31.78	17.37	9.589	5.202	3.028
GJ_i - $\frac{\text{# in.}^2}{\text{rad}}$ · 10^{-8}	46.4	26.9	12.25	8.85	4.98	2.35
Chord - in.	105.4	95.3	85.2	75.1	65.0	54.9
Elastic Axis - % chord aft of Leading Edge	33.6	33.6	33.6	33.6	33.6	33.6
Center of Gravity - % chord aft of Leading Edge	38.9	35.8	39.0	42.3	42.8	44.1
Front Spar - % chord aft of Leading Edge	26.8	26.8	26.8	26.8	26.8	26.8
Rear Spar - % chord aft of Leading Edge	61.5	61.5	61.5	61.5	61.5	61.5
Aileron Hinge Line - % chord aft of Leading Edge	76.2	76.2	76.2	76.2	76.2	76.2

S_o = Semispan - 235 in.

64

TABLE III

(Taken from Reference 9)

KEY TO GENERALIZED DAMAGE CLASSES

Dashed lines in the sketches below indicate regions of possible hole damage. Projectile penetrates both regions of each sketch. These dashed lines do not indicate total skin damage, but locations of a family of possible projectile holes. Holes of class E & F damages have projecting skin; all other damages are flush holes.

Damage Classes	Wing Section
A,B	
C,D	
E,G,H	
F,J,K	
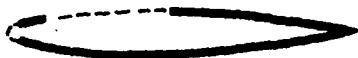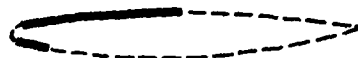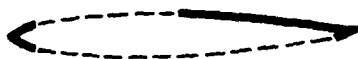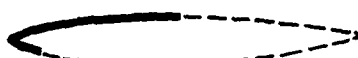
Damage Classes	Hole Size *
A, C, E, F, G, J	.15c
B, D, H, K	.10c

* Diameter of an equal area circular hole

Digest of Drag Increases Due to Damage

Damage Class	Hole Size [+]	M = .3		M = .7		M = .85
		$\frac{C_{D}^{*}}{\pi}$	p^{*}	$\frac{C_{D}^{*}}{\pi}$	p^{*}	$\frac{C_{D}^{*}}{\pi}$
A	.15c	1.2	6	2.4	10	3.4
B	.10c	1.0	5	2.7	16	2.2
C	.15c	.8	2.5	1.3	.3	-.7
D	.10c	1.0	1	2.3	-1.5	-.5
E	.15c	.2	6	1.0	9	1
F	.15c	.2	.3	1.0	-.5	1
G	.15c	-.2	4	0	6	-1
H	.10c	0	4	0	7	-2.5
J	.15c	-.2	.7	0	0	-1
K	.10c	-.2	1	0	.5	-2.5

[+] Diameter of an equal area circular hole

Table IV

Drag Rise Due to Forward Facing Steps or Blunt Leading Edge. (Reference 10)
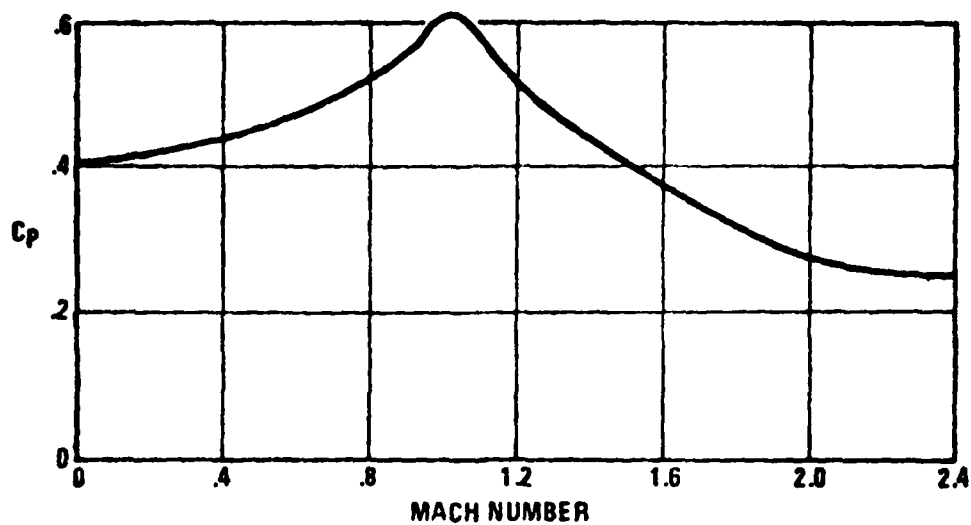
The Drag Rise Coefficient $\Delta C_D = \frac{A}{S} C_p$, where A is the area of the forward facing blunt surfaces, $(A = tl)$, and S is the reference wing area.
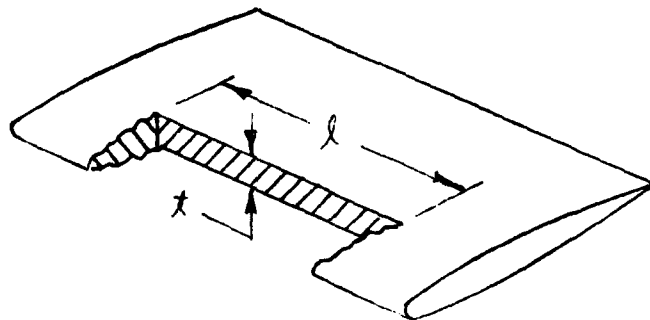
TABLE V

DAMAGE INDUCED DRAG LEVELS FOR VARIOUS
MANEUVERING FLIGHT CONDITIONS

LOAD FACTOR n	c_L	c_D^* upper & lower bounds		$\Delta D \sim$ LBS		
				2% hole	3% hole	5% hole
1	0.143	1.10	2.60	3,242# to 7,660#	4,863# to 11,492#	8,150# to 19,150#
5	0.713	3.54	7.48	10,433# to 22,040#	15,649# to 33,062#	26,080# to 55,100#
6	0.856	4.70	9.73	13,851# to 28,667#	20,777# to 43,000#	34,628# to 71,667#
6.5	0.927	5.30	11.0	15,619# to 32,400#	23,429# to 48,620#	39,048# to 81,033#

600 mph true maneuvering speed
20,000 ft. combat altitude

67

TABLE VI

CRITICAL DIVERGENCE SPEEDS
FOR AERODYNAMICALLY DAMAGED WING

no structural damage

ΔD @ 80% semi-span sea level			ΔD @ 90% semi-span sea level	
divergence speed mph	ΔD lbs		divergence speed mph	ΔD lbs
1470	0		1470	0
1151	22,160		1029	17,700
1038	36,050		912	27,900
887	65,830		776	50,360
785	102,950		699	81,680

ΔD @ 80% semi-span
20,000 ft

divergence speed mph	ΔD lbs
2030	0
1579	22,200
1422	36,040
1215	65,740
1074	102,790

TABLE VI (Cont'd.)

CRITICAL FLUTTER SPEEDS
FOR AERODYNAMICALLY DAMAGED WING

no structural damage

ΔD @ 80% semi-span sea level			ΔD @ 90% semi-span sea level	
flutter speed mph	ΔD lbs		flutter speed	ΔD lbs
940	0		940	0
980	16,065		1040	18,091
1040	36,189		1900	114,512

ΔD @ 80% semi-span
20,000 ft

ΔD #	Flutter speed mph
0	1280
14,932	1300
32,966	1360

TABLE VI (Cont'd.)

PRELIMINARY STUDY TO INVESTIGATE
INFLUENCE OF STRUCTURAL DAMAGE
ON DIVERGENCE SPEEDS

sea level
ΔD @ 80% semi-span

ΔD #	Nature of Structural Damage	Divergence speed mph
	EI Reduced 30% at Stations 5 & 6	
20060	GJ " 50% " " "	1095
61,190	"	855
96,570	"	760
157,030	"	685
195,400	"	683
	EI Reduced 40% at Stations 5 & 6	
	GJ " 60% " " " "	
19,220	"	1072
59,720	"	845
94,600	"	752
154,250	"	679
184,940	"	665

TABLE VI (Cont'd.)

PRELIMINARY STUDY TO INVESTIGATE
INFLUENCE OF STRUCTURAL DAMAGE
ON DIVERGENCE SPEEDS

sea level

ΔD @ 80% semi-span

ΔD #	Nature of Structural Damage	Divergence speed mph
17,855	EI Reduced 50% at Stations 5&6 GJ " " 70% " " " "	1033
56,655	"	823
90,366	"	735
148,841	"	667
17,820	EI Reduced 50% at Station 6 EI Reduced 70% at Station 5 GJ Reduced 70% at Stations 5&6	1032
56,380	"	821
90,120	"	734
147,950	"	665
177,780	"	652
17,820	EI Reduced 70% at Stations 5&6 GJ Reduced 70% at stations 5&6	1032
56,370	"	821
90,120	"	734
147,900	"	665

TABLE VI (Cont'd.)

PRELIMINARY STUDY TO INVESTIGATE
INFLUENCE OF STRUCTURAL DAMAGE
ON DIVERGENCE SPEEDS

sea level

ΔD @ 80% semi-span

ΔD #	Nature of Structural Damage	Divergence speed mph
17060	{ EI Reduced 30% at Stations 4,5&6 GJ " " 50% " " " " }	1010
57,730	"	794
83,850	"	708
138,320	"	643
167,040	"	632
15,620	{ EI Reduced 40% at Stations 4,5&6 GJ " " 60% " " " " " }	955
48,060	"	758
76,900	"	678
128,600	"	620
156,120	"	611

TABLE VI (Cont'd.)

PRELIMINARY STUDY TO INVESTIGATE
INFLUENCE OF STRUCTURAL DAMAGE
ON DIVERGENCE SPEEDS

sea level

ΔD @ 80% semi-span

ΔD #	Nature of Structural Damage	Divergence speed mph
13040	EI Reduced 50% at Stations 4,5&6 GJ " " 70% " " " "	833
42040	"	709
68,090	"	683
115,070	"	588
141,650	"	582
12,260	EI Reduced 70% at Stations 4,5&6 GJ " " 70% " " " "	865
39,470	"	687
63,270	"	615
106,420	"	564

TABLE VI (Cont'd.)

PRELIMINARY STUDY TO INVESTIGATE
INFLUENCE OF STRUCTURAL DAMAGE
ON DIVERGENCE SPEEDS

sea level

ΔD @ 90% semi-span

ΔD #	Nature of Structural Damage	Divergence speed mph
15,110	EI Reduced 30% at Stations 5&6 GJ " " 50% " " " "	950
43,900	"	725
74,420	"	667
14,070	EI Reduced 40% at Stations 5&6 GJ " " 60% " " " "	917
41,340	"	703
71,330	"	653
12,340	EI Reduced 70% at Station 5 " " 50% " " 6 GJ " 70% " Stations 5&6	859
36,650	"	662
64,930	"	623

TABLE VI (Cont'd.)

PRELIMINARY STUDY OF INVESTIGATE
INFLUENCE OF STRUCTURAL DAMAGE
ON DIVERGENCE SPEEDS

sea level

ΔD @ 90% semi-span

ΔD #	Nature of Structural Damage	Divergence speed mph
12,716	EI Reduced 50% at Stations 5&6 GJ " " 70% " " " "	872
37,990	"	674
67,243	"	634
12,290	EI Reduced 70% at Stations 5&6 GJ " " 70% " " " "	857
36,320	"	659
64,510	"	621

75

CONVERGENCE STUDY

Undamaged - 1 Surface

$$IC = 1$$
$$LS = 3$$

CASE	NC	NS	$C_{L_\alpha}(\frac{1}{rad})$	$\Delta C_{L_\alpha}(\frac{1}{rad})$	XCP	YCP
A	1	1	3.5760		1.1431	1.0157
				+0.5037		
B	2	2	3.0723		1.1559	1.1028
				-0.0219		
C	3	3	3.0942		1.1521	1.1061
				+0.0442		
D	4	4	3.0500		1.1656	1.1120
				-0.0059		
E	5	5	3.0559		1.1637	1.1118
				+0.0035		
F*	6	6	3.0524		1.1661	1.1125
				N/A		
G	4	5	3.0629		1.1629	1.1116
				-0.0096		
H	4	6	3.0725		1.1643	1.1117
				-0.0336		
I	3	6	3.1061		1.1573	1.1108

*"best" solution

TABLE VII

CONVERGENCE STUDY OF CONTROL POINT SELECTION

Undamaged

CASE	SURFACE #	NC	NS
	1	1	1
	2	1	1
	3	1	1
	4	1	1
1	5	1	1
	6	1	1
	7	1	1
	8	1	1
	9	1	1
	1	1	2
	2	1	2
	3	2	2
	4	1	1
2	5	1	1
	6	2	1
	7	1	2
	8	1	2
	9	2	2
	1	2	2
	2	2	2
	3	2	2
	4	2	2
3 .	5	2	2
	6	2	2
	7	2	2
	8	2	2
	9	2	2
	1	2	3
	2	2	3
	3	3	3
	4	2	2
4	5	2	2
	6	3	2
	7	2	3
	8	2	3
	9	3	3

CASE	SURFACE #	NC	NS
	1	2	3
	2	2	3
	3	4	3
	4	2	2
5	5	2	2
	6	4	2
	7	2	3
	8	2	3
	9	4	3
	1	2	4
	2	2	4
	3	5	4
	4	2	2
6	5	2	2
	6	5	2
	7	2	3
	8	2	3
	9	5	3
	1	1	6
	2	1	6
	3	3	6
	4	1	1
8	5	1	1
	6	3	1
	7	1	2
	8	1	2
	9	3	2
	1	1	6
	2	1	6
	3	4	6
	4	1	1
9	5	1	1
	6	4	1
	7	1	2
	8	1	2
	9	4	2

Case 7 damaged only

Damaged

Same selections but surface 5 removed.

TABLE VIII

PRESSURE WEIGHTING

FUNCTION SELECTION

Undamaged - Cases: 1, 2, 3, 4, 5, 6, 8, 9

Surface #	IC	LS
1	3	2
2	4	2
3	2	2
4	3	2
5	4	2
6	2	2
7	3	3
8	4	3
9	2	3

Damaged - Cases: 1D, 2D, 3D, 4D, 5D, 6D, 8D, 9D

Surface #	IC	LS
1	3	2
2	4	3
3	2	2
4	1	2
5	1	2
6	3	3
7	4	1
8	2	3

Damaged - Cases: 7D, 10D

Surface #	IC	LS
1	3	2
2	4	2
3	2	2
4	3	2
5	2	2
6	3	3
7	4	3
8	2	3

TABLE IX

CONVERGENCE STUDY

	UNDAMAGED – 9 SURFACES						DAMAGED – 8 SURFACES				
CASE	$C_{L_\alpha}(\frac{1}{rad})$	$\Delta C_{L_\alpha}(\frac{1}{rad})$	ΔC_{L_α} % difference of Case F	XCP	YCP	CASE	$C_{L_\alpha}(\frac{1}{rad})$	$\Delta C_{L_\alpha}(\frac{1}{rad})$	XCP	YCP	ΔC_{L_α} % difference of Damaged and Undamaged
1	3.5535	+.5243	+16.4%	1.2256	1.1589	1D	3.3465	+.5331	1.1989	1.1200	-5.8%
2	3.0292	-.3700	-0.8%	1.1438	1.1081	2D	2.8134	-.2611	1.1329	1.0900	-7.1%
3	3.3992	+.3032	+11.4%	1.2160	1.1229	3D	3.0745	+.1534	1.1954	1.0919	-9.5%
4	3.0960	+.0543	+1.4%	1.1865	1.1184	4D	2.9211	+.0426	1.1691	1.0898	-5.7%
5	3.0417	+.0732	-0.4%	1.1829	1.1176	5D	2.8785	+.0727	1.1662	1.0900	-5.3%
6	2.9685		-2.7%	1.1697	1.1141	6D	2.8058		1.1608	1.0961	-5.5%
N/A						7D*	3.0893		1.1966	1.1257	+1.6%†
8	3.0184	+.0953	-1.1%	1.1661	1.1181	8D	2.8611	+.0799	1.1604	1.0976	-5.2%
9	2.9231		-4.2%	1.1635	1.1209	9D	2.7812		1.1586	1.1012	-4.9%
N/A						10D**	3.0467		1.1810	1.1236	+0.9%††

*Case 5D without Kutta conditions imposed on hole
**Case 8D without Kutta conditions imposed on hole
†Compared with Case 5
††Compared with Case 8

TABLE X

COARSE MODEL

Pressure Weighting Function Selections

	Surface #	IC	LS
Undamaged	1	3	2
	2	2	2
	3	3	2
	4	2	2
	5	3	3
	6	2	3
Damaged	1	3	3
	2	2	2
	3	1	2
	4	3	1
	5	2	3

TABLE XI

COARSE MODEL

	$C_{L_\alpha}(\frac{1}{rad})$	$\Delta C_{L_\alpha}(\%)$	XCP	YCP
Undamaged	2.9930		1.1547	1.1033
		+1.51%		
Damaged	3.0383		1.1745	1.1116

TABLE XII

81

TABLE XIII

LOCATION OF PRESSURE TAPS ON T-38 STABILIZER

Spanwise Positions % semispan	Chordwise Positions % local chord
17.4	0
33.9	1.25
50.4	2.5
58.7	5.0
66.9	10
71.1	15
75.2	20
79.3	30
83.5	40
91.7	50
	60
	70
	80
	90
	95
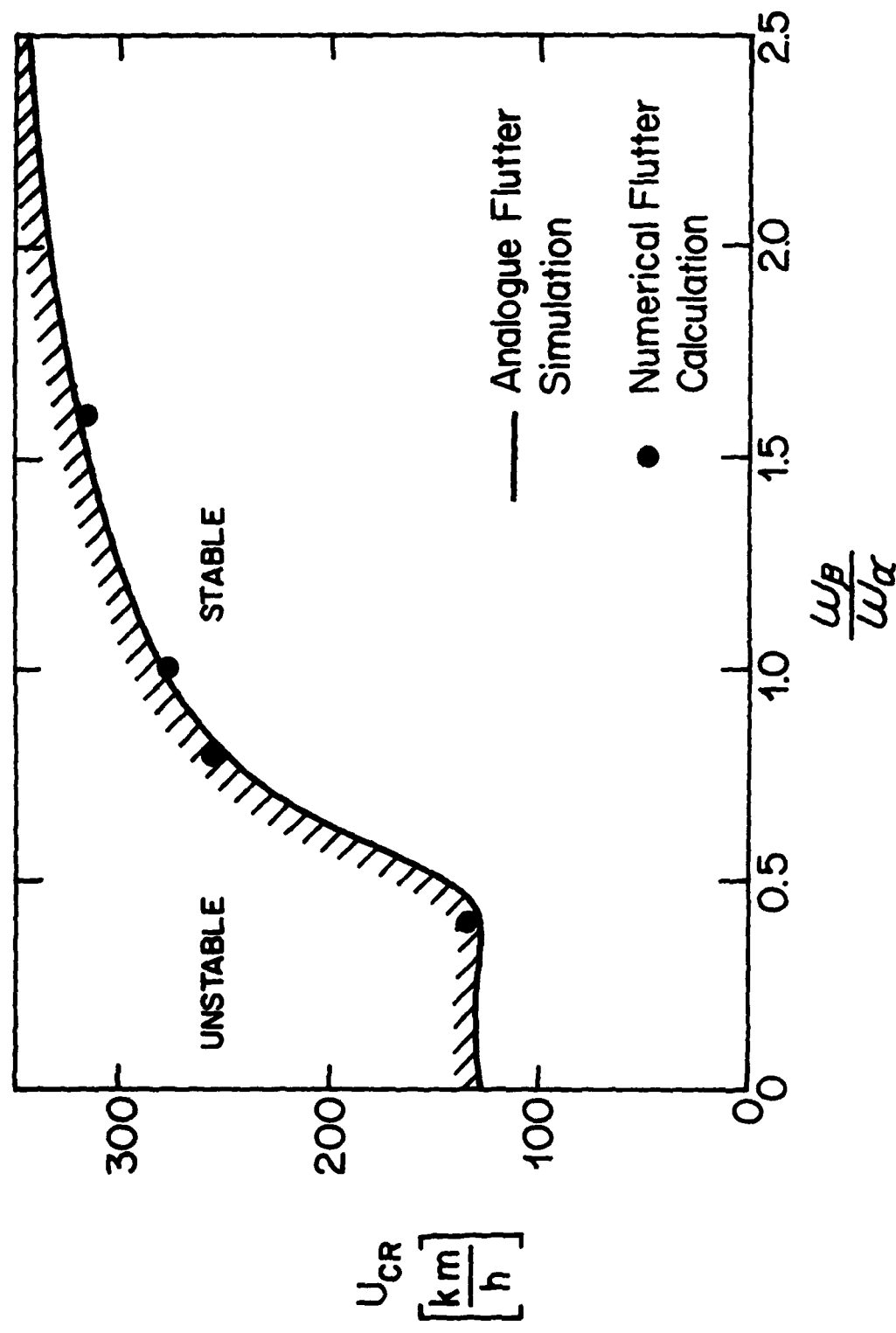
Critical Speed of Wing Aileron System for Simulated Control Damage

(Taken from Reference 5)

Figure 1

83

a) Finite element lumped mass modeling of wing structure along
    its elastic axis

i = 1   2   3   4   5   6

NOTE: Locations
of the two aero-
dynamic damage
sites investigated
① - 80% semi-span
② - 90% semi-span

reference
axis

35.25
TYP
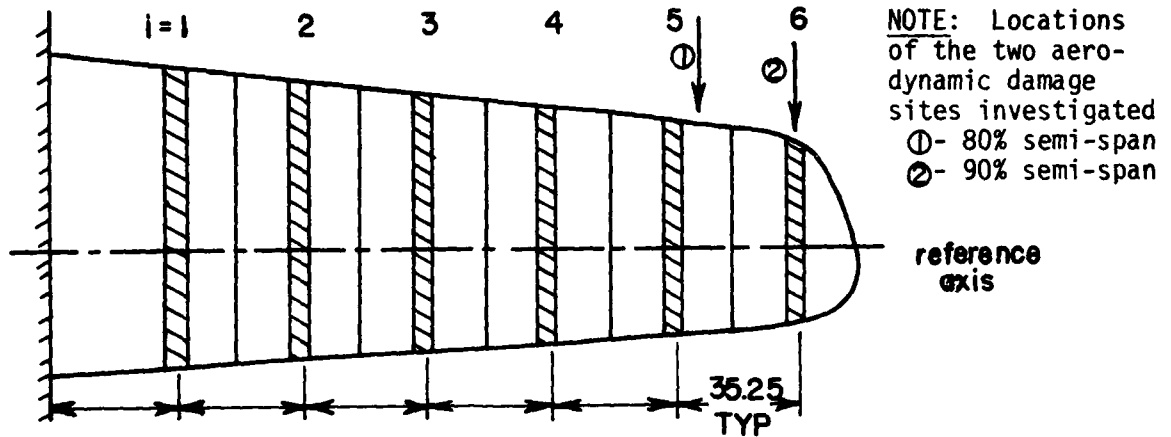
b) Two spar stressed skin semimonocoque wing structure

front
spar   skin   rear
                                    spar

trailing
edge

nose torque   main torque   stiffeners
box   box

c) Strip theory aerodynamic modeling

-b   O ba bc be +b $\bar{x} = bx$

h

C_h

C_α

V

α

C_β
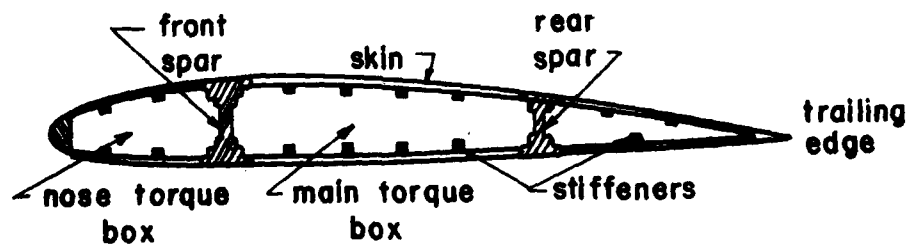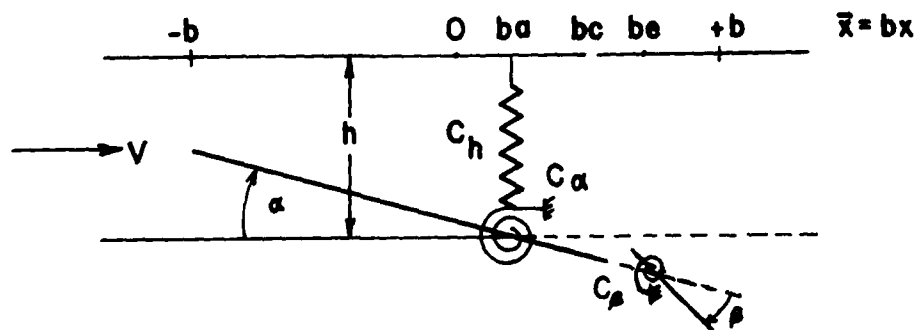
AEROELASTIC MODELING EMPLOYING AN ELASTIC AXIS BEAM TYPE
STRUCTURE AND A STRIP THEORY AERODYNAMIC APPROXIMATION

Figure 2

84

MICROCOPY RESOLUTION TEST CHART
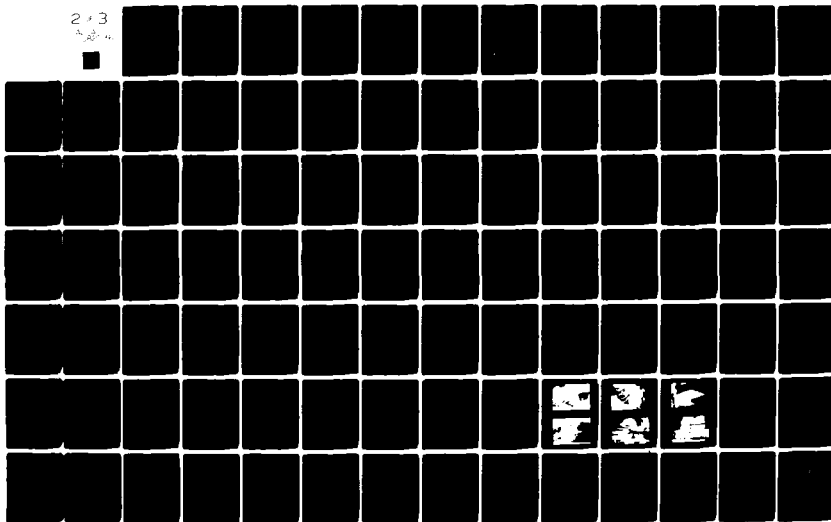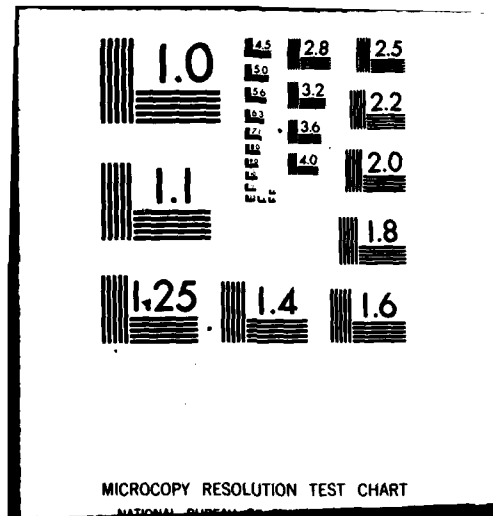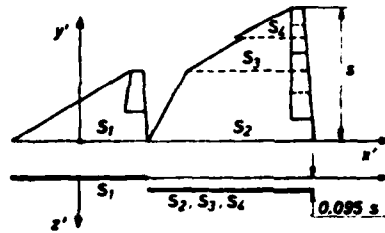
FLUTTER SPEED REDUCTION
DUE TO LEADING-EDGE VORTEX EFFECT
(Taken from Reference 6)

Figure 3
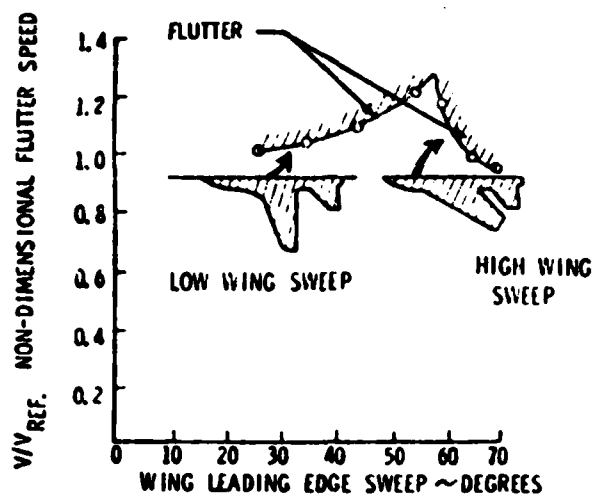
Figure 4a - WING-FUSELAGE-TAIL FLUTTER

A

B
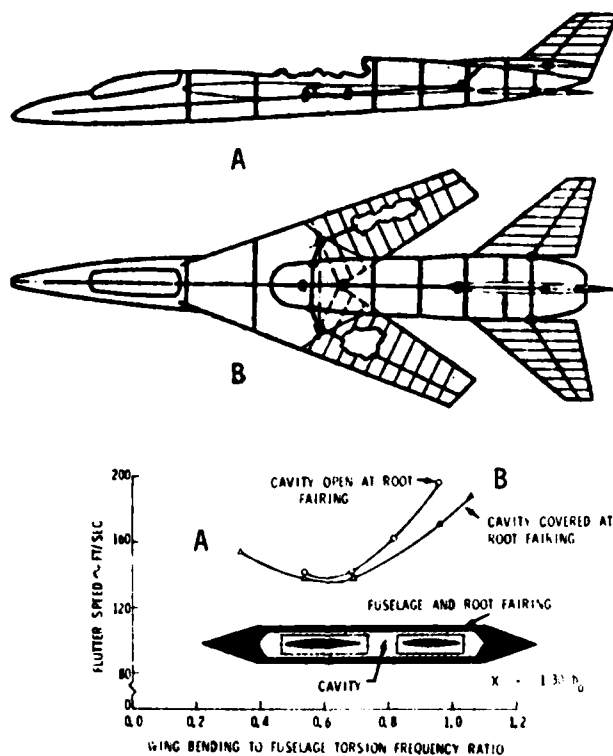
Figure 4b - FUSELAGE CAVITY EFFECTS ON FLUTTER
SPEEDS, 70 DEGREES WING SWEEP (EXPERIMENTAL DATA)

PLAUSIBLE REDUCTION IN WING TAIL FLUTTER SPEEDS OF
VARIABLE GEOMETRY AIRCRAFT THAT MIGHT BE AFFECTED
BY BALLISTIC DAMAGE TO FUSELAGE AND/OR WINGS

Figure 4

86
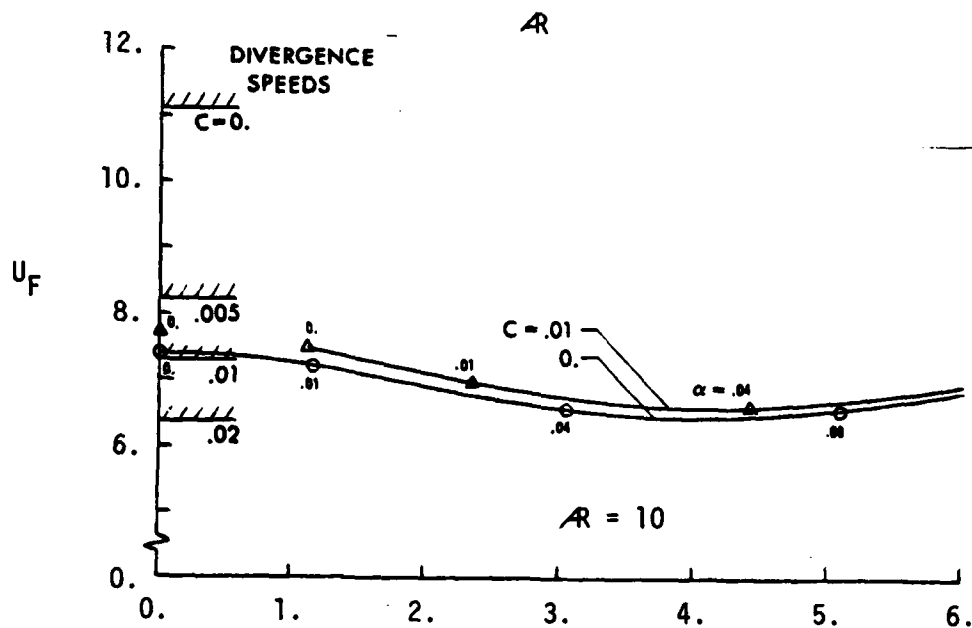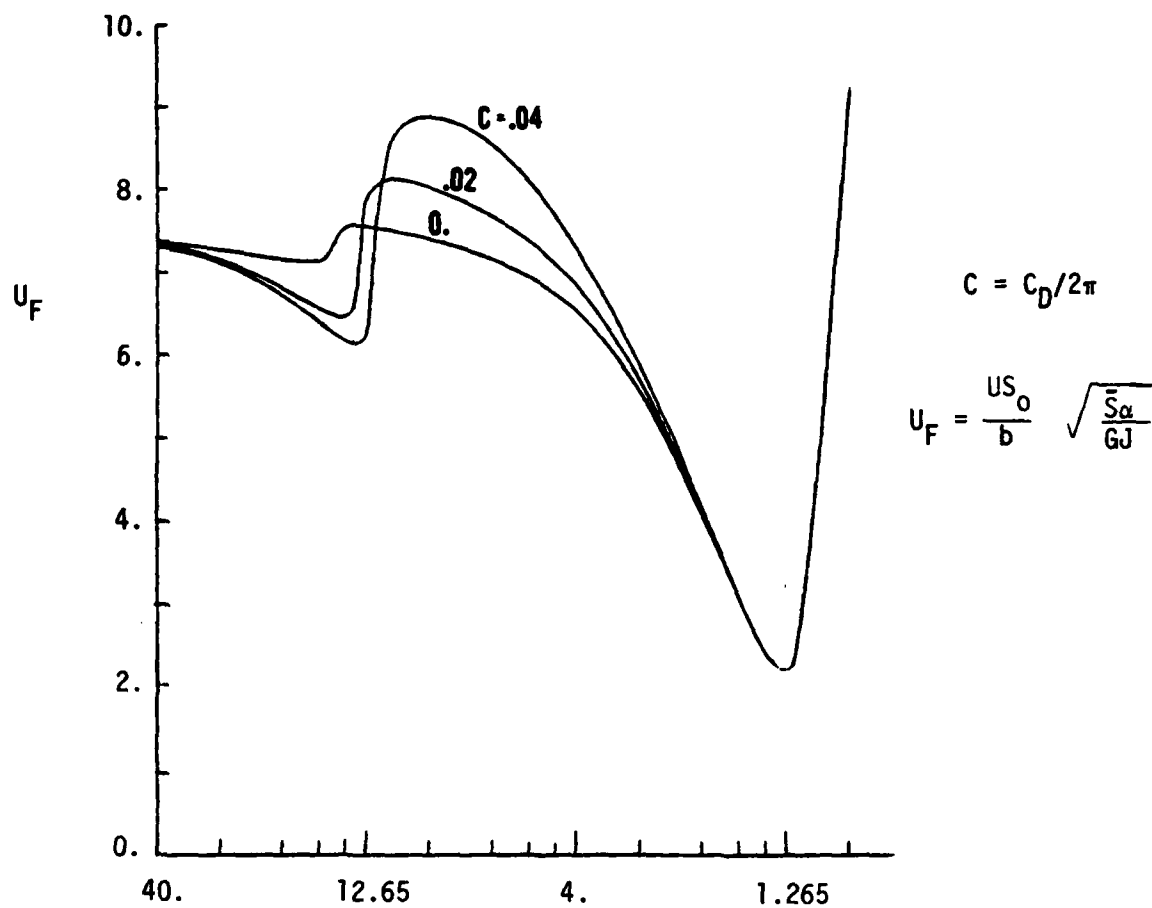
DEPENDENCE OF FLUTTER & DIVERGENCE SPEEDS ON DRAG PARAMETER
AND ASPECT RATIO PARAMETER (Taken from Reference 4)

Figure 5
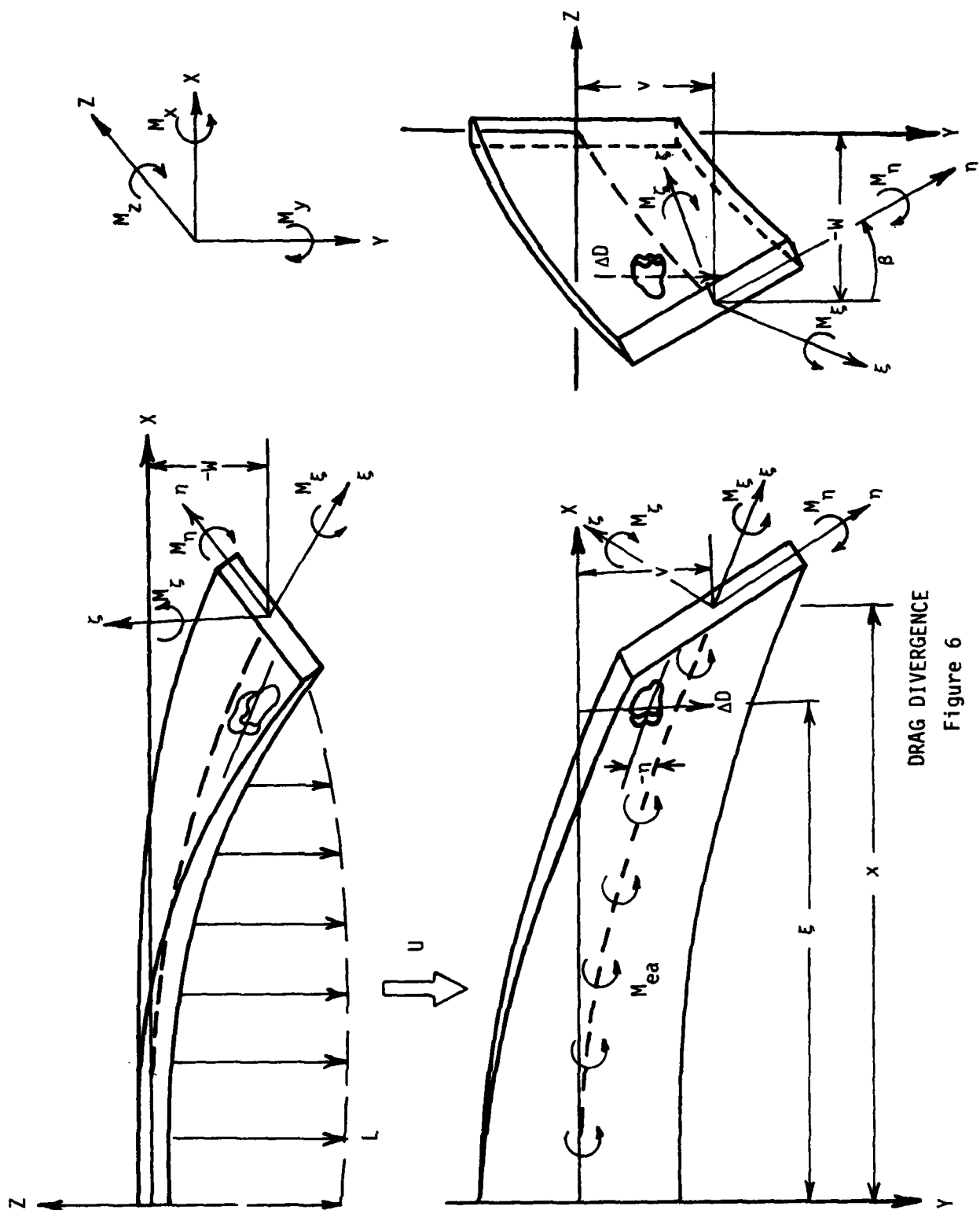
DRAG DIVERGENCE
Figure 6

88
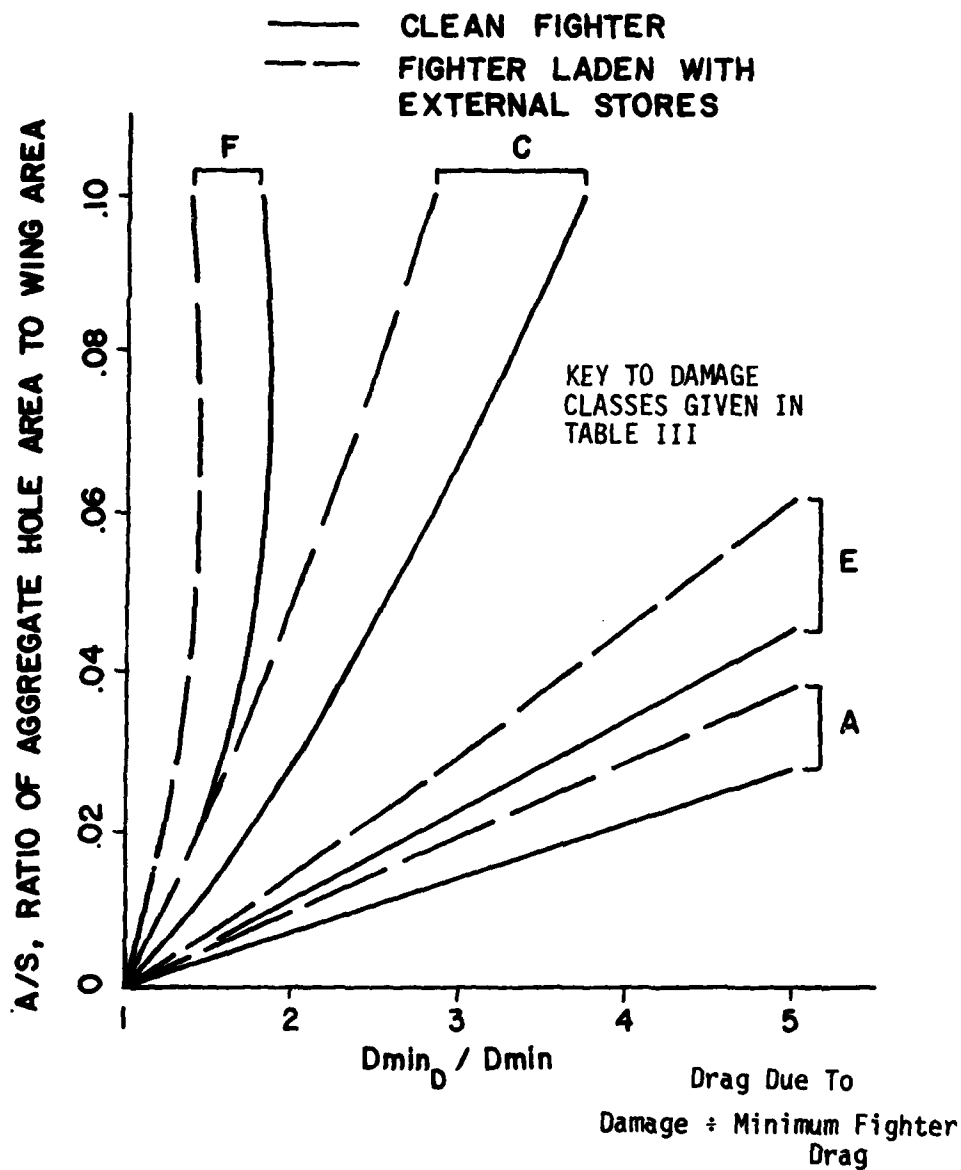
RELATIONSHIPS BETWEEN MAGNITUDE OF
DAMAGE AND INCREASE OF MINIMUM
DRAG FOR A GENERIC FIGHTER

Figure 7

89
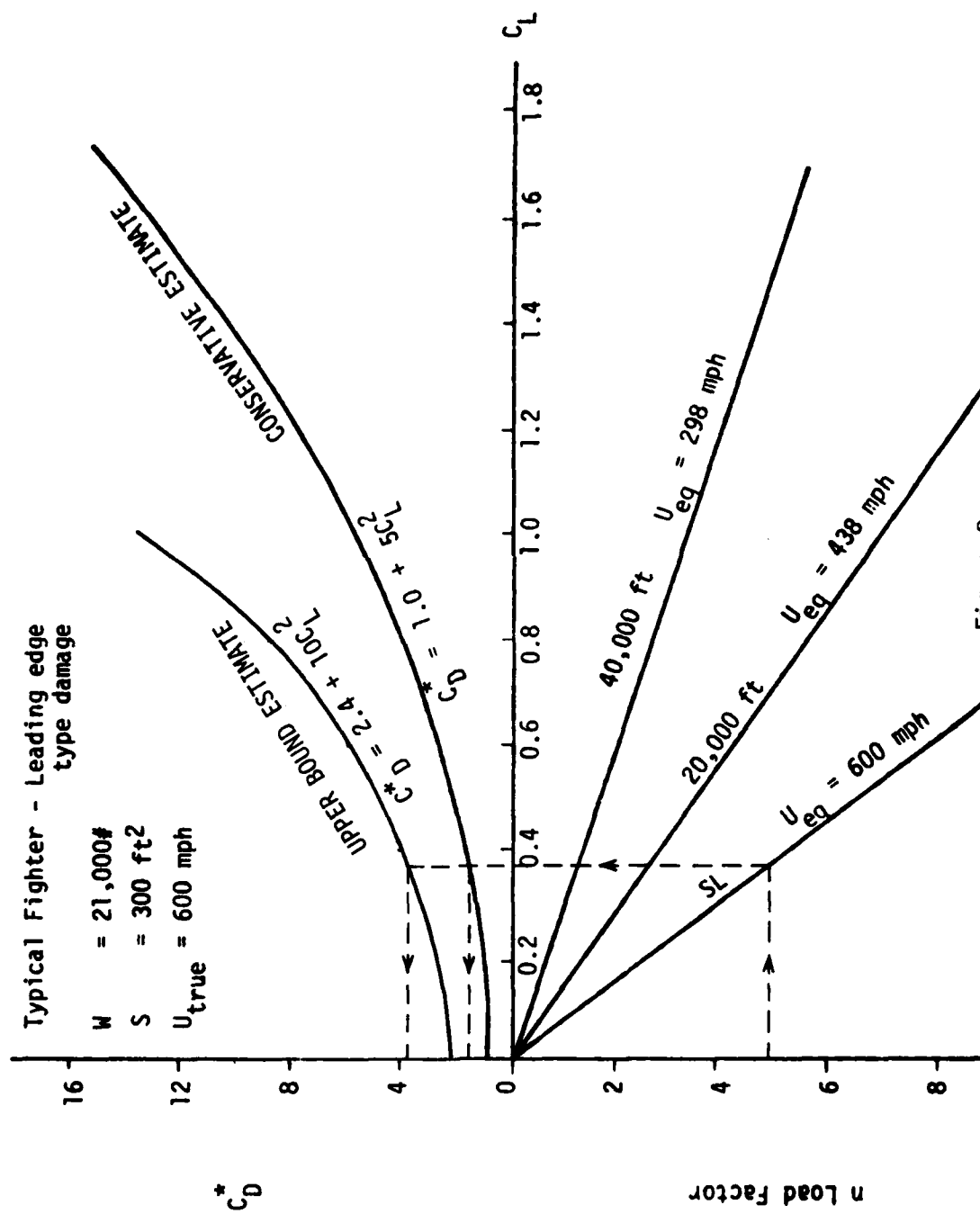
Figure 8

Conservative and Upper Bound Estimates on the Damage Induced Drag Coefficient C_D^*
for Various Maneuvering Load Factors and Combat Altitudes

90

Typical Fighter – Leading Edge Type Damage

$W = 21,000\#$
$S = 300\ ft^2$
$U_{true} = 600\ mph$
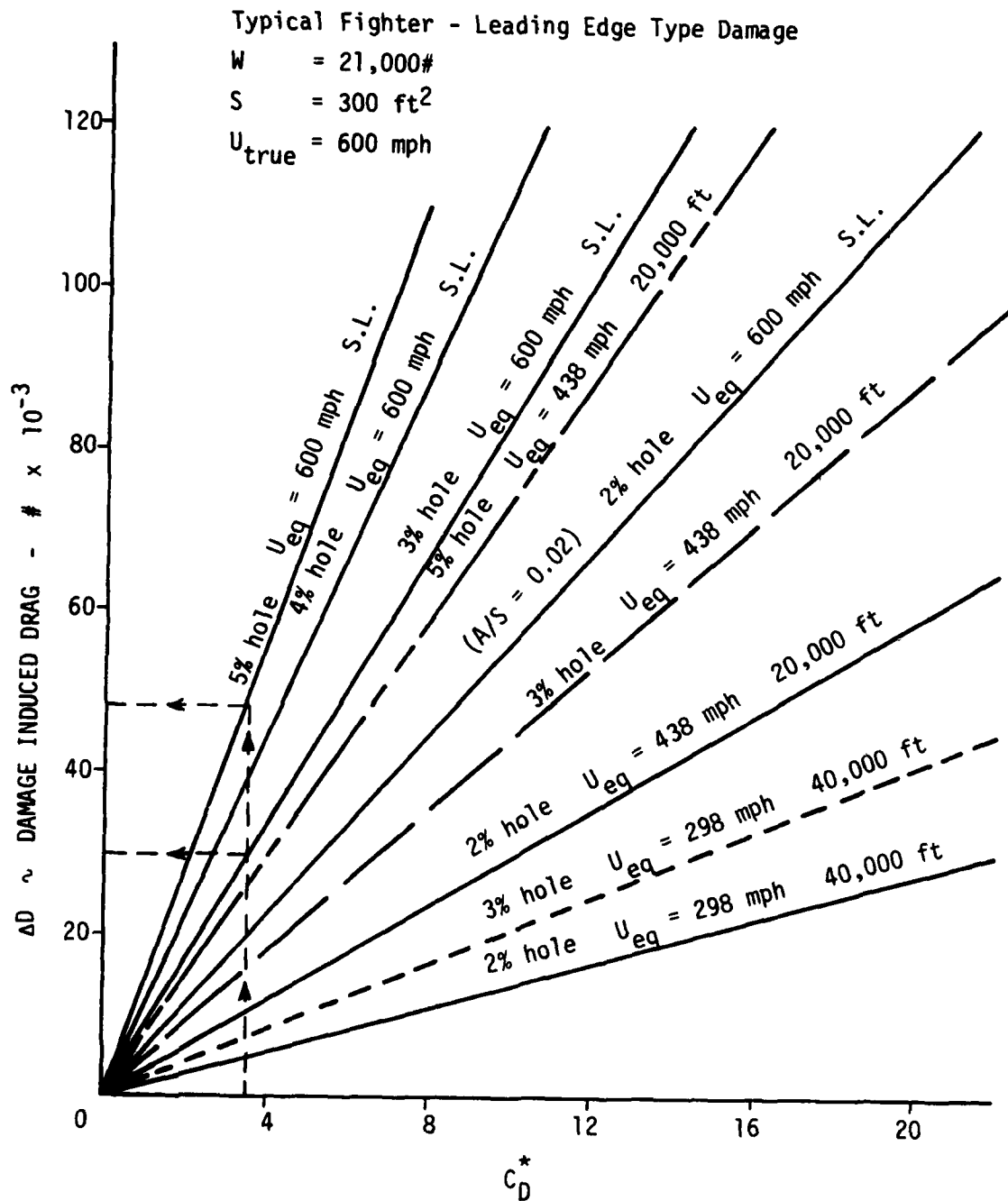
$$\Delta D = C_D^* A q = C_D^* \left(\frac{A}{S}\right) S q$$

DAMAGE INDUCED DRAG FORCE FOR VARIOUS SIZE DAMAGE
AREAS AND ALTITUDES FOR A TRUE MANEUVERING SPEED OF 600 MPH

Figure 9

91
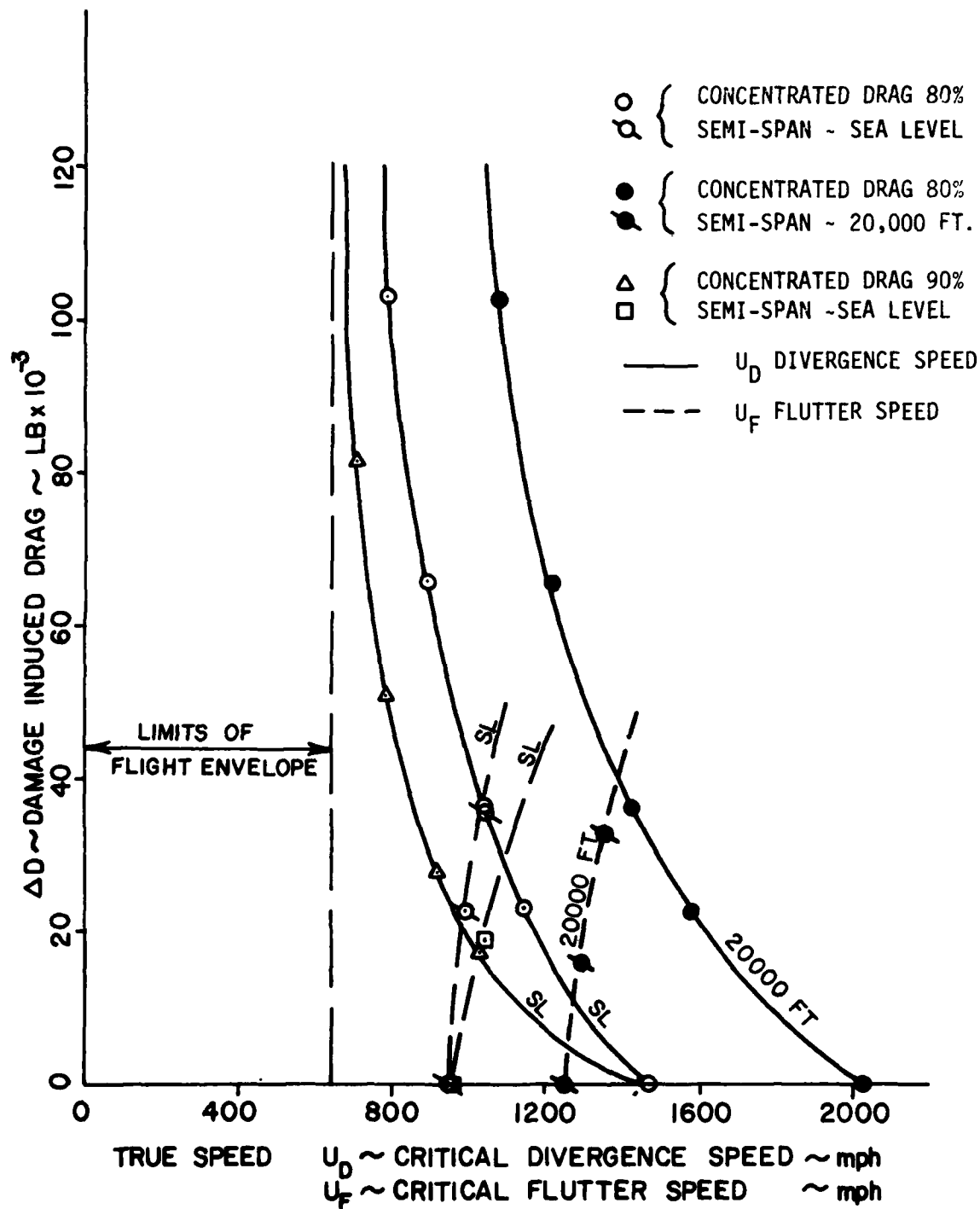
INFLUENCE OF AERODYNAMIC DAMAGE IN THE FORM OF
DAMAGE INDUCED DRAG (NO STRUCTURAL DAMAGE) ON THE FLUTTER
AND DIVERGENCE SPEEDS OF THE STATISTICAL FIGHTER WING
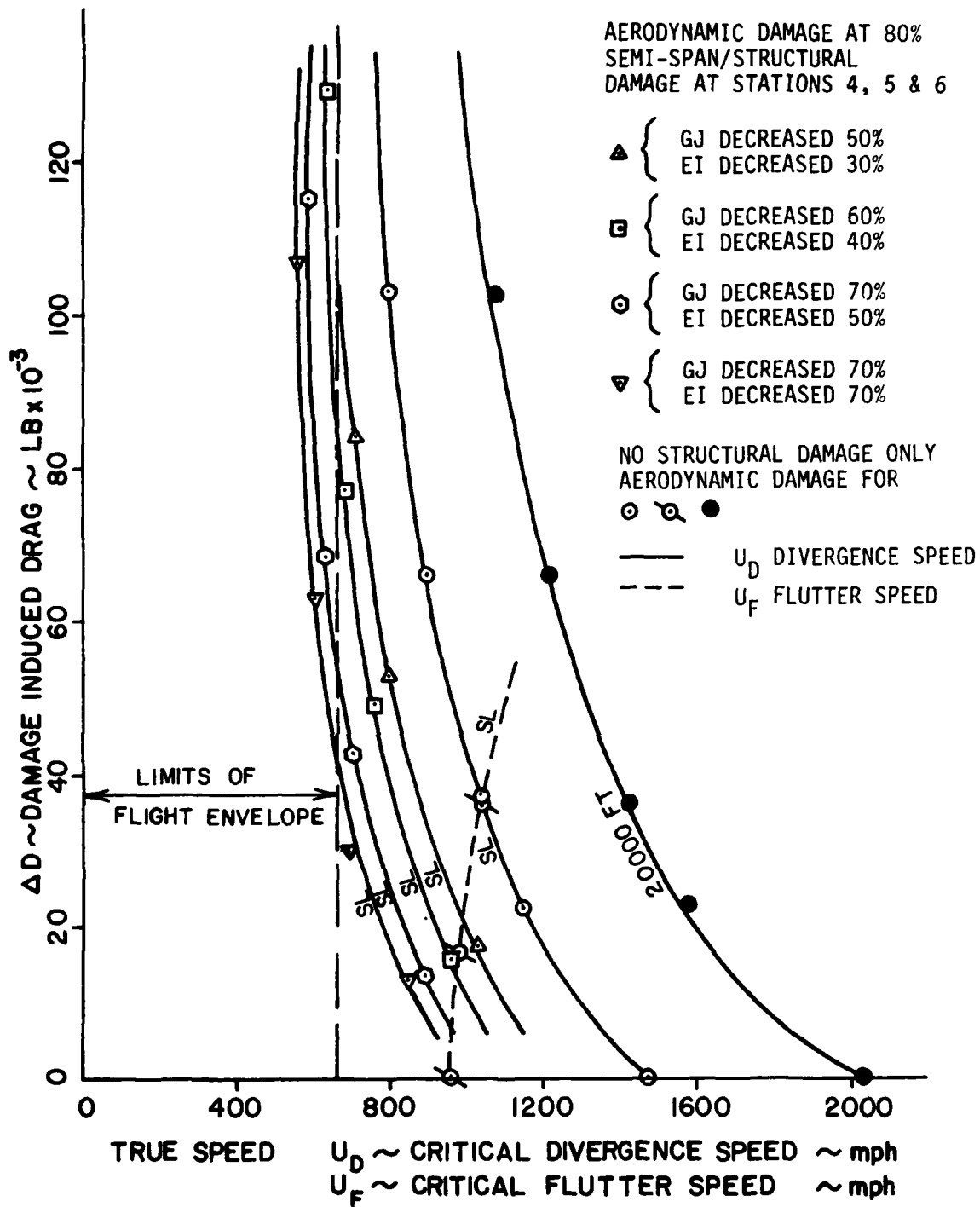
Figure 10

INFLUENCE OF COMBINED AERODYNAMIC AND STRUCTURAL DAMAGE
ON THE DIVERGENCE SPEED OF THE STATISTICAL FIGHTER
WING - AERODYNAMIC DAMAGE SITE AT 80% SEMI-SPAN

Figure 10 Cont'd.

△ { GJ DECREASED 50%
    EI DECREASED 30%

□ { GJ DECREASED 60%
    EI DECREASED 40%

⊙ { GJ DECREASED 70%
    EI DECREASED 50%

▽ { GJ DECREASED 70%
    EI DECREASED 70%

NO STRUCTURAL DAMAGE ONLY
AERODYNAMIC DAMAGE FOR
⊙ ⚲

———— U_D DIVERGENCE SPEED

– – – U_F FLUTTER SPEED

$\Delta D \sim$ DAMAGE INDUCED DRAG $\sim$ LB x 10^{-3}

120 100 80 60 40 20 0

LIMITS OF
FLIGHT ENVELOPE

0   400   800   1200   1600   2000

TRUE SPEED

$U_D \sim$ CRITICAL DIVERGENCE SPEED $\sim$ mph
$U_F \sim$ CRITICAL FLUTTER SPEED $\sim$ mph
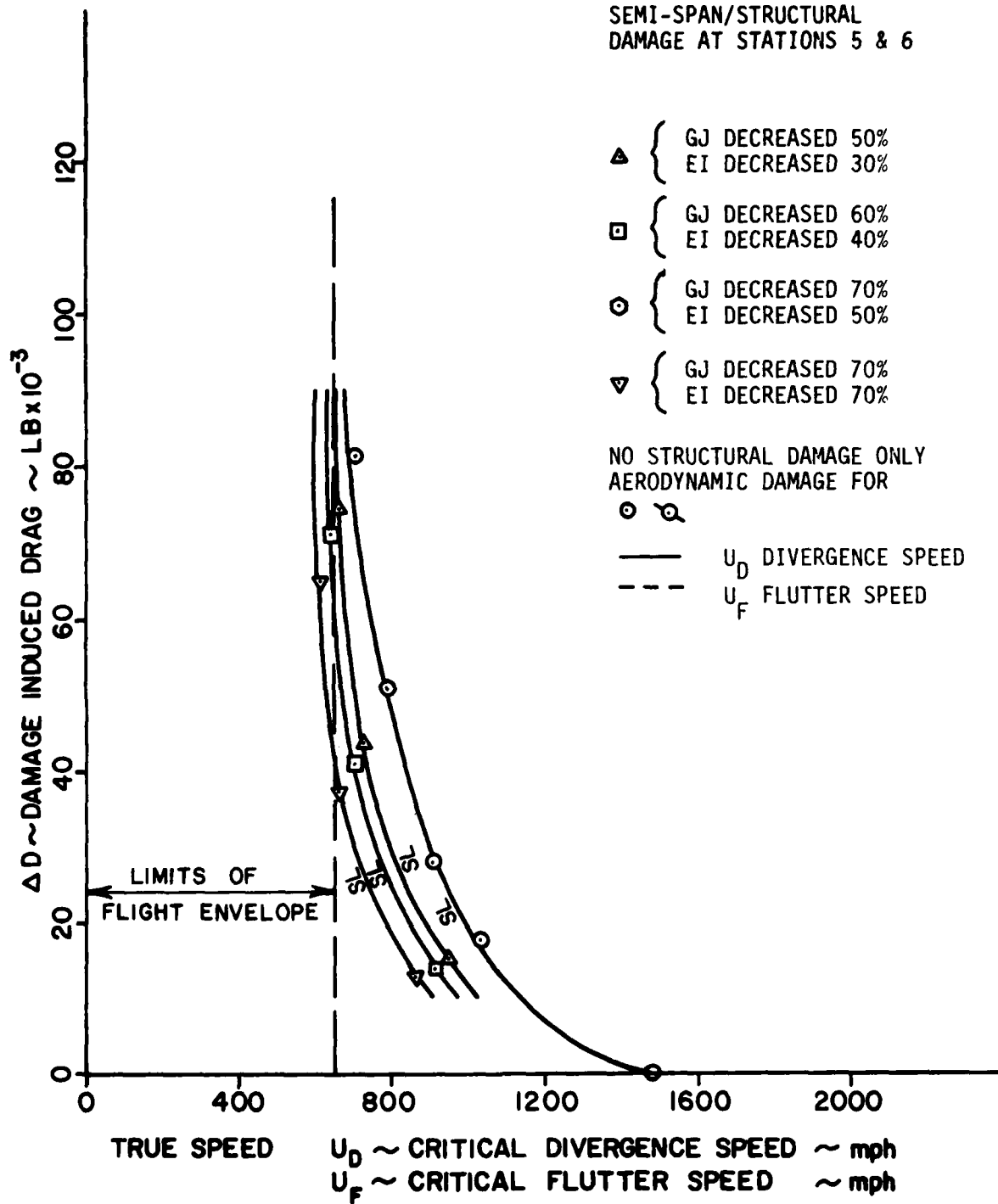
INFLUENCE OF COMBINED AERODYNAMIC AND STRUCTURAL DAMAGE
ON THE DIVERGENCE SPEED OF THE STATISTICAL FIGHTER WING –
AERODYNAMIC DAMAGE SITE AT 90% SEMI-SPAN

Figure 10 Cont'd.
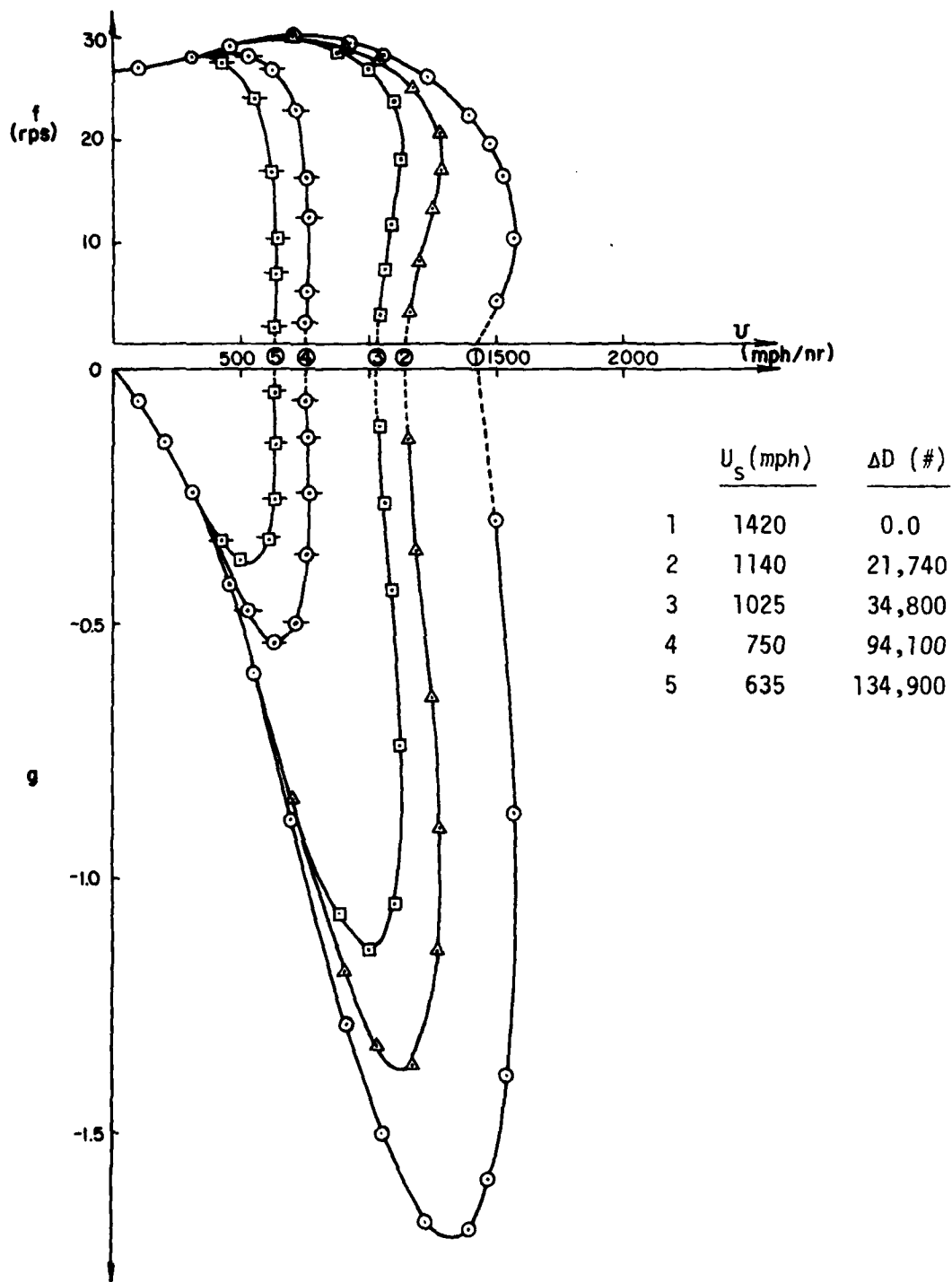
PARAMETER STUDY OF v-g AND v-ω CURVES
FOR A RANGE OF DAMAGE INDUCED DRAG LEVELS

Figure 11

M_∞

Influence point
(ξ, η, ζ)

y, η

Downwash point
(x, y, z)

x, ξ
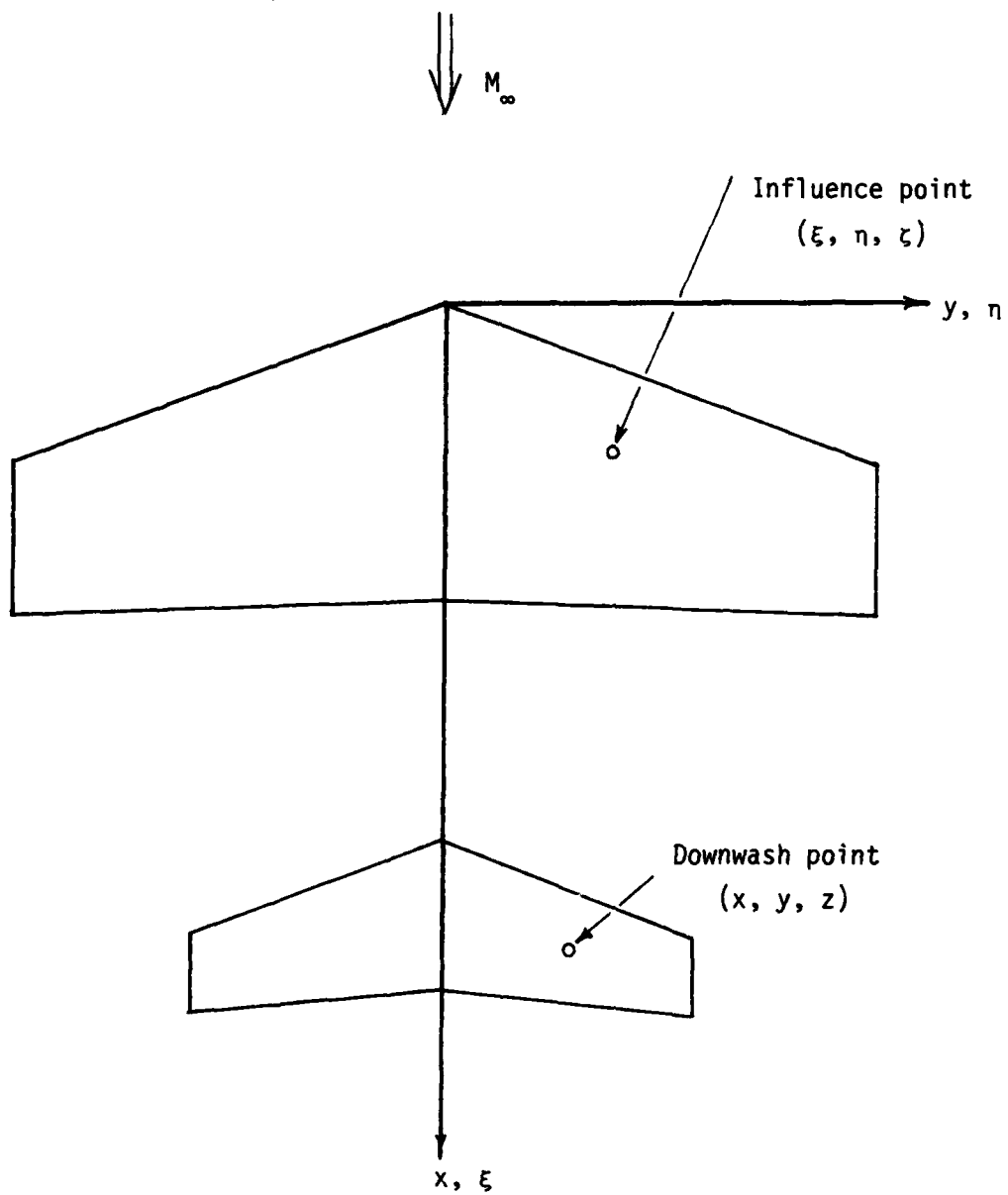
GENERAL SOURCE POINT AND FIELD POINT DESCRIPTIONS

Figure 12

96

SURFACE AND LOADING TYPES IN THE AERODYNAMIC PROGRAM
Figure 13

97

CHORDWISE INTERDIGITATION

$$\bar{m} = 3 \qquad J = 3$$

LE   TE

$$\xi_1 \quad \underline{x}_1 \quad \xi_2 \quad \underline{x}_2 \quad \xi_3 \quad \underline{x}_3$$
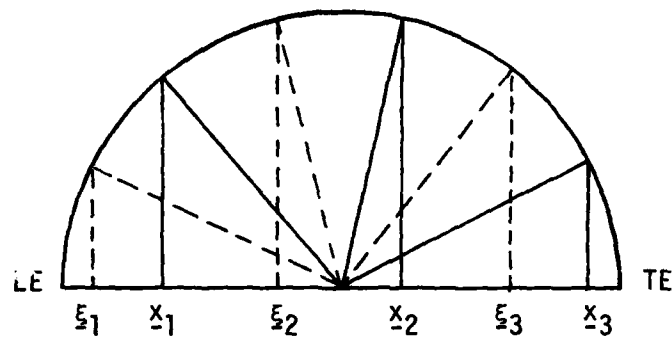
Figure 14

SPANWISE TRANSFORMATION

$$S' = 10$$

$\eta_1' \quad \eta_2' \quad \eta_3' \quad \eta_4' \quad \eta_5' \quad \eta_6' \quad \eta_7' \quad \eta_8' \quad \eta_9' \quad \eta_{10}'$

-1 $+1$

$\underline{\eta}_5 \quad \underline{\eta}_6 \quad \underline{\eta}_7 \quad \underline{\eta}_8 \quad \underline{\eta}_9 \quad \underline{\eta}_2 \quad \underline{\eta}_3 \quad \underline{\eta}_4$

$\underline{\eta}_{10} \quad \underline{\eta}_1$

Figure 15

98

Y

(37.53, 60.85)

(66.19, 60.85)

o Integration
point (ξ, η, ζ)

o Downwash
point (x, y, z)

(0.0, 0.0)

Reflecting Plane

X

(61.25, 0.0)

SINGLE SURFACE MODEL

Figure 16

99
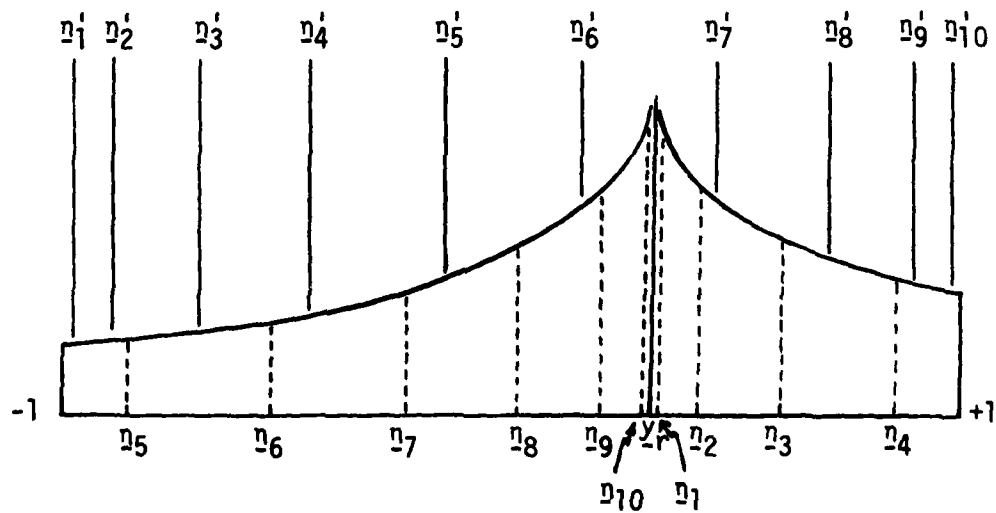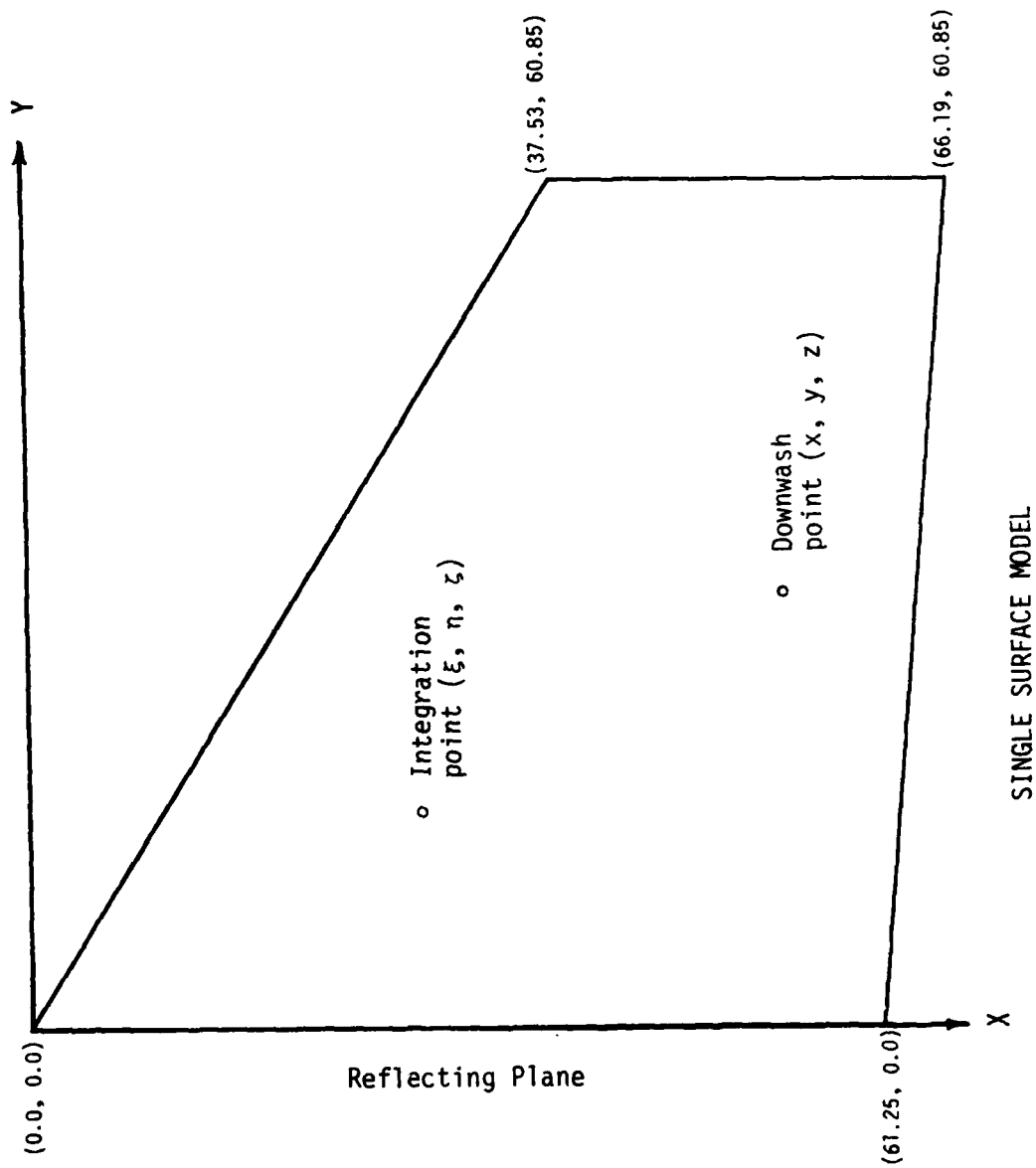
WEIGHTING FUNCTION STUDY
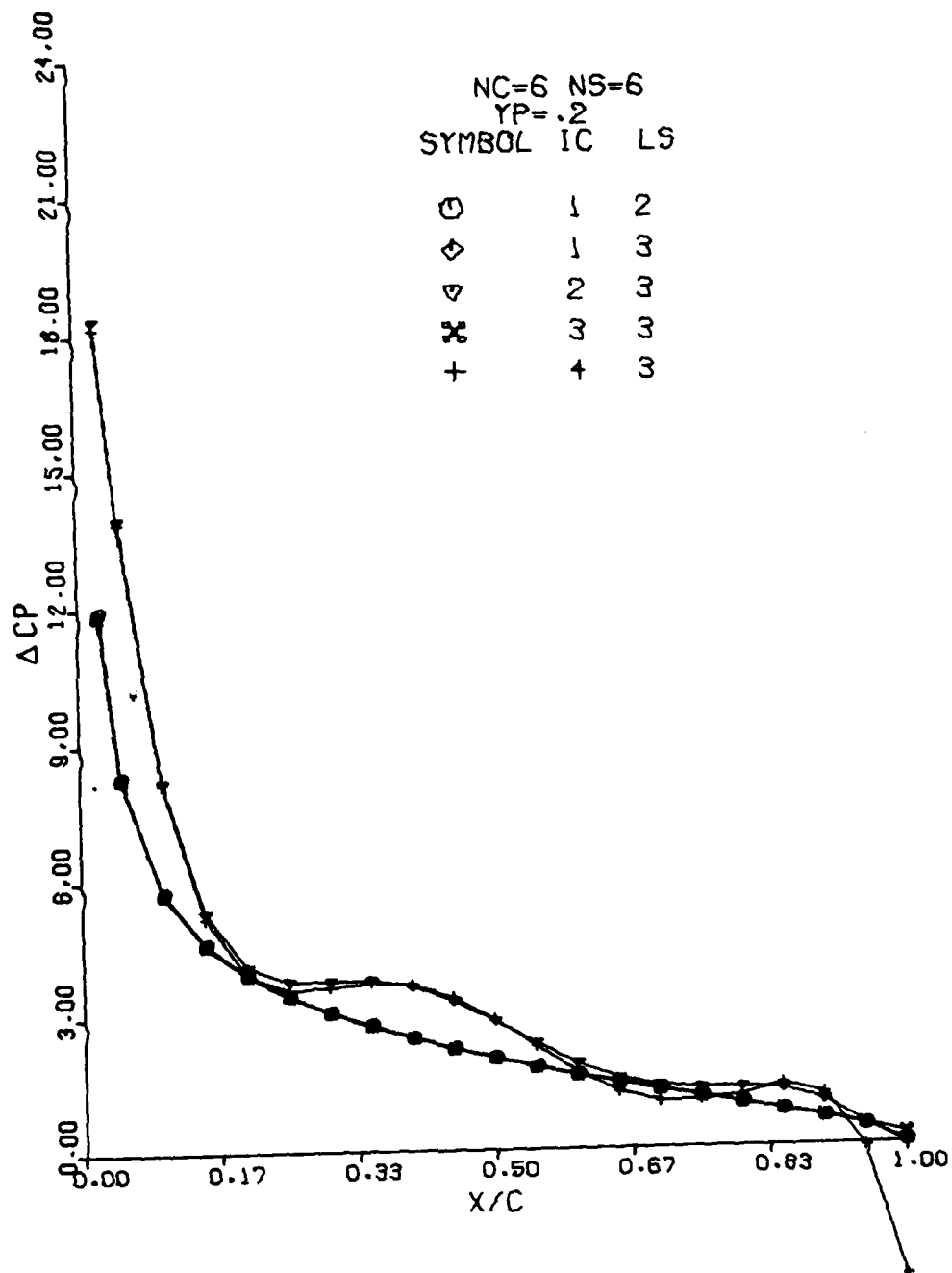
Figure 17

WEIGHTING FUNCTION STUDY
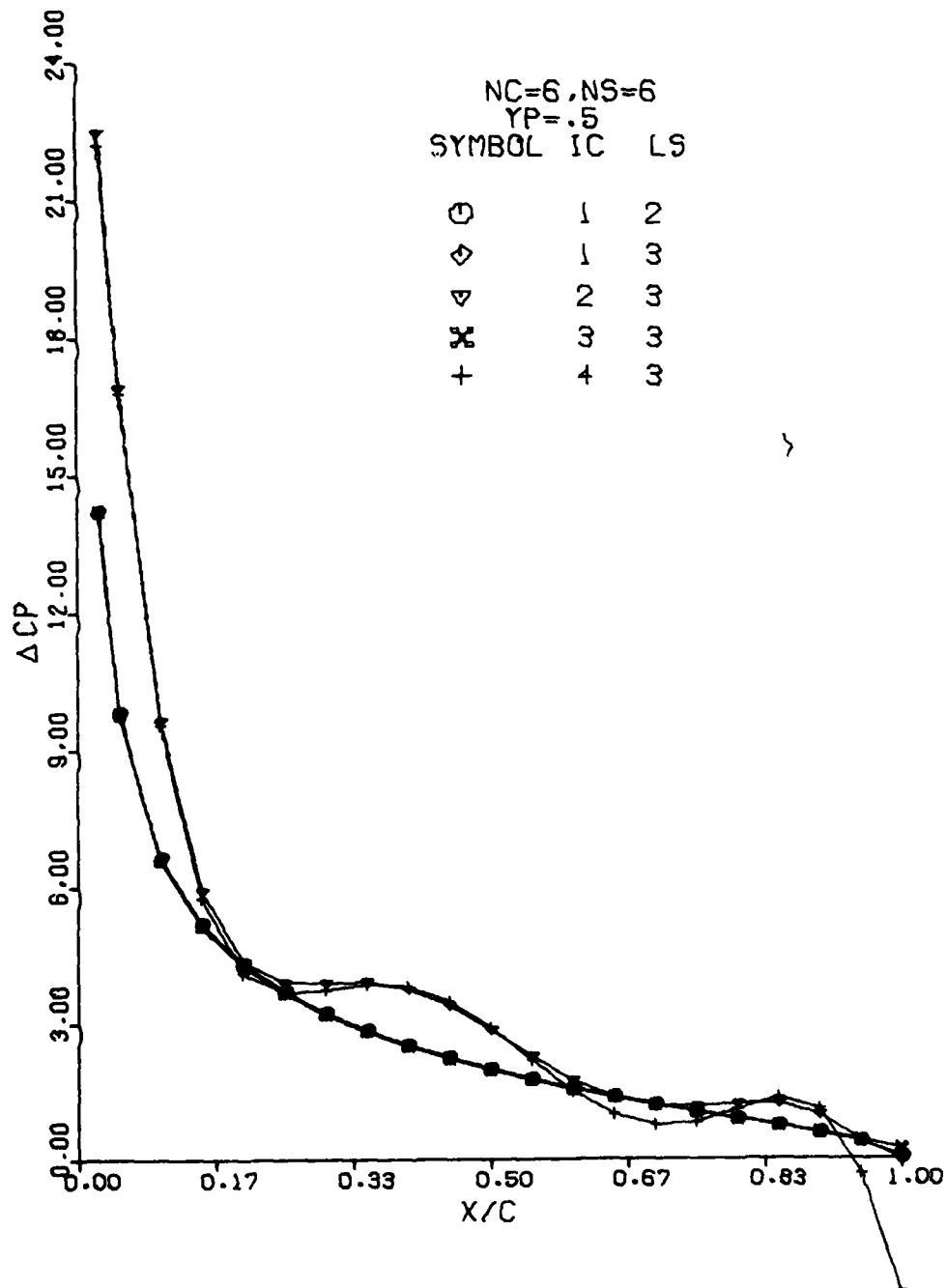
Figure 18

WEIGHTING FUNCTION STUDY

NC=6,NS=6
YP=.9

SYMBOL	IC	LS
⊕	1	2
◇	1	3
▽	2	3
✖	3	3
+	4	3

Figure 19

102
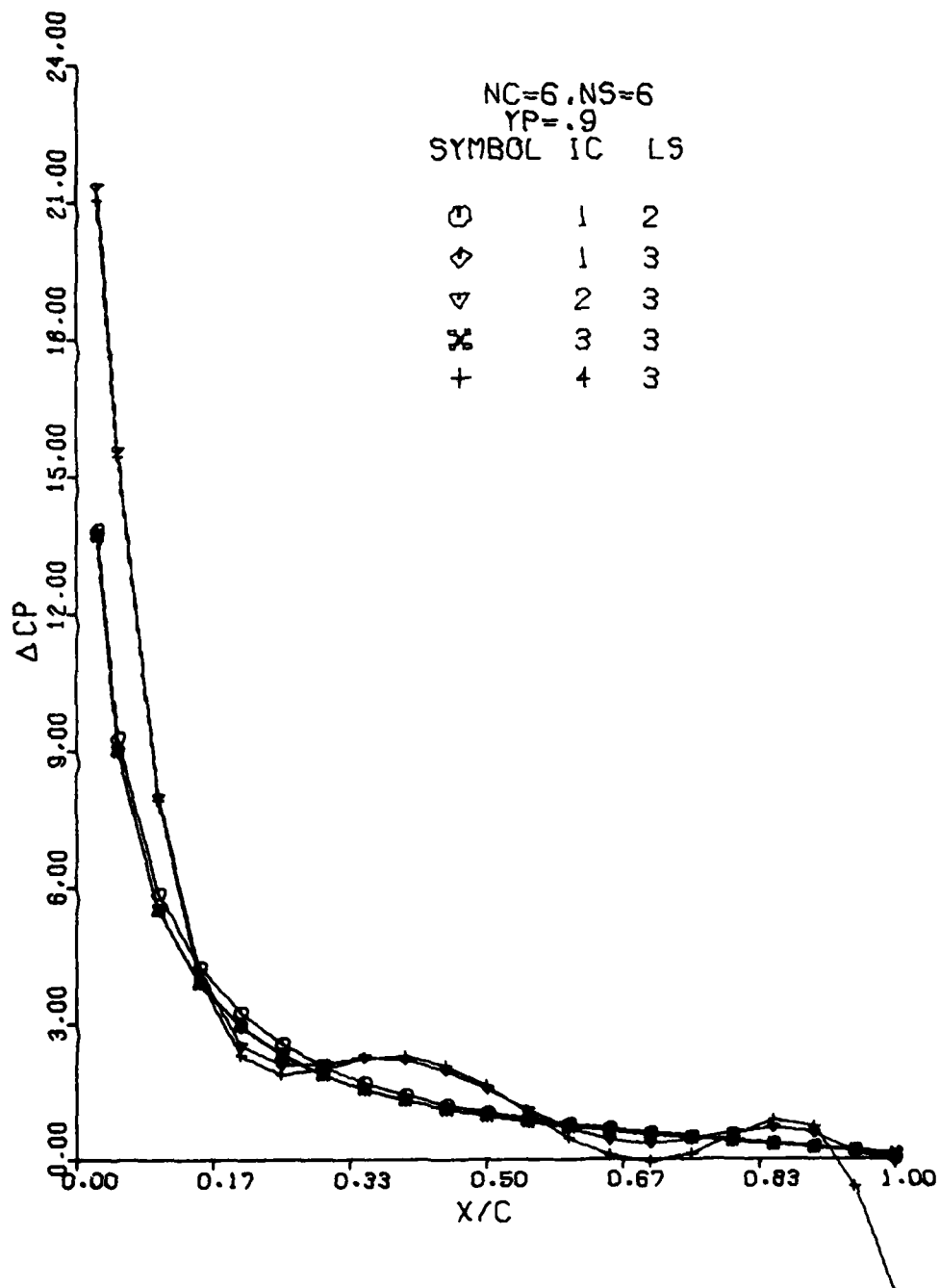
WEIGHTING FUNCTION STUDY

Figure 20

103
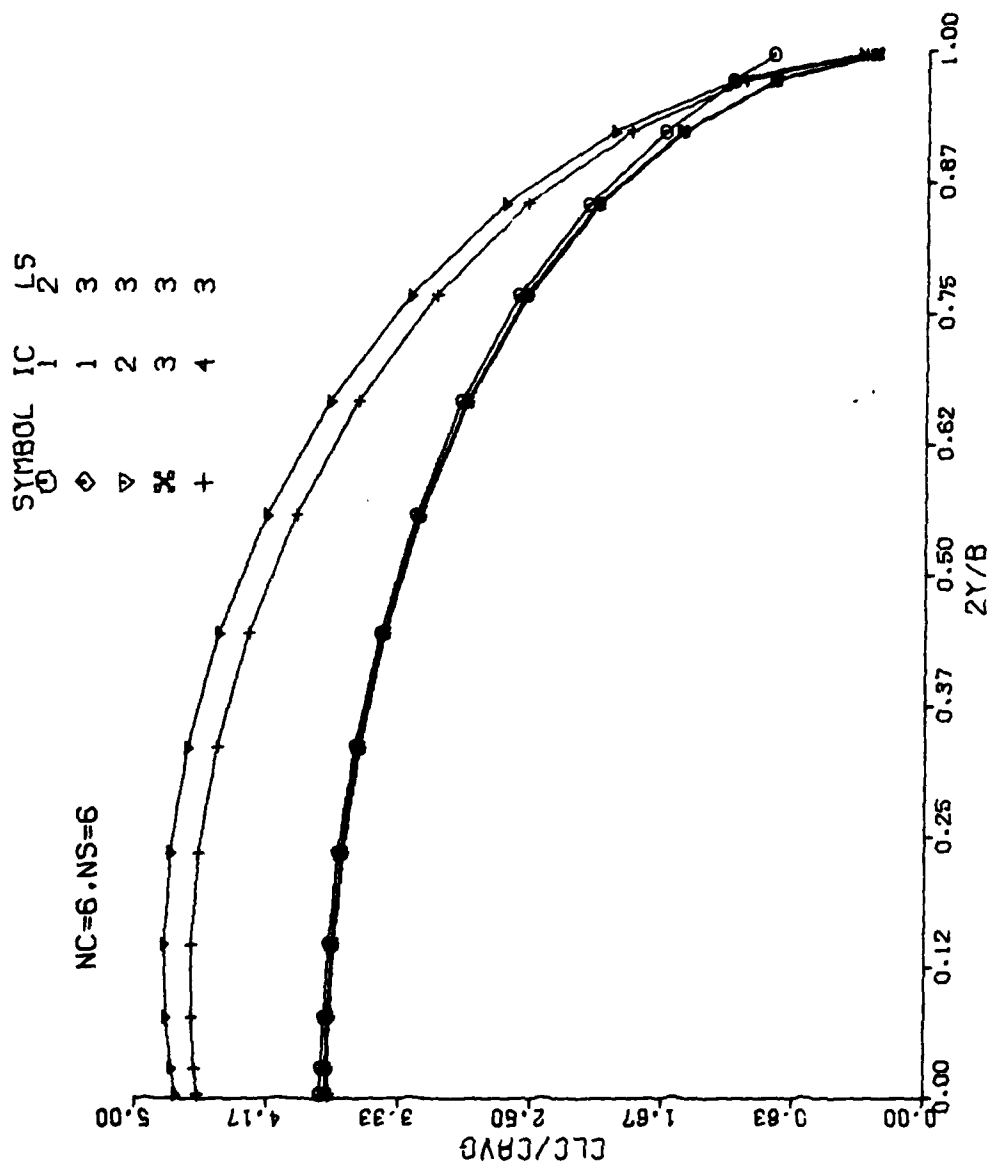
WEIGHTING FUNCTION STUDY

Figure 21

104
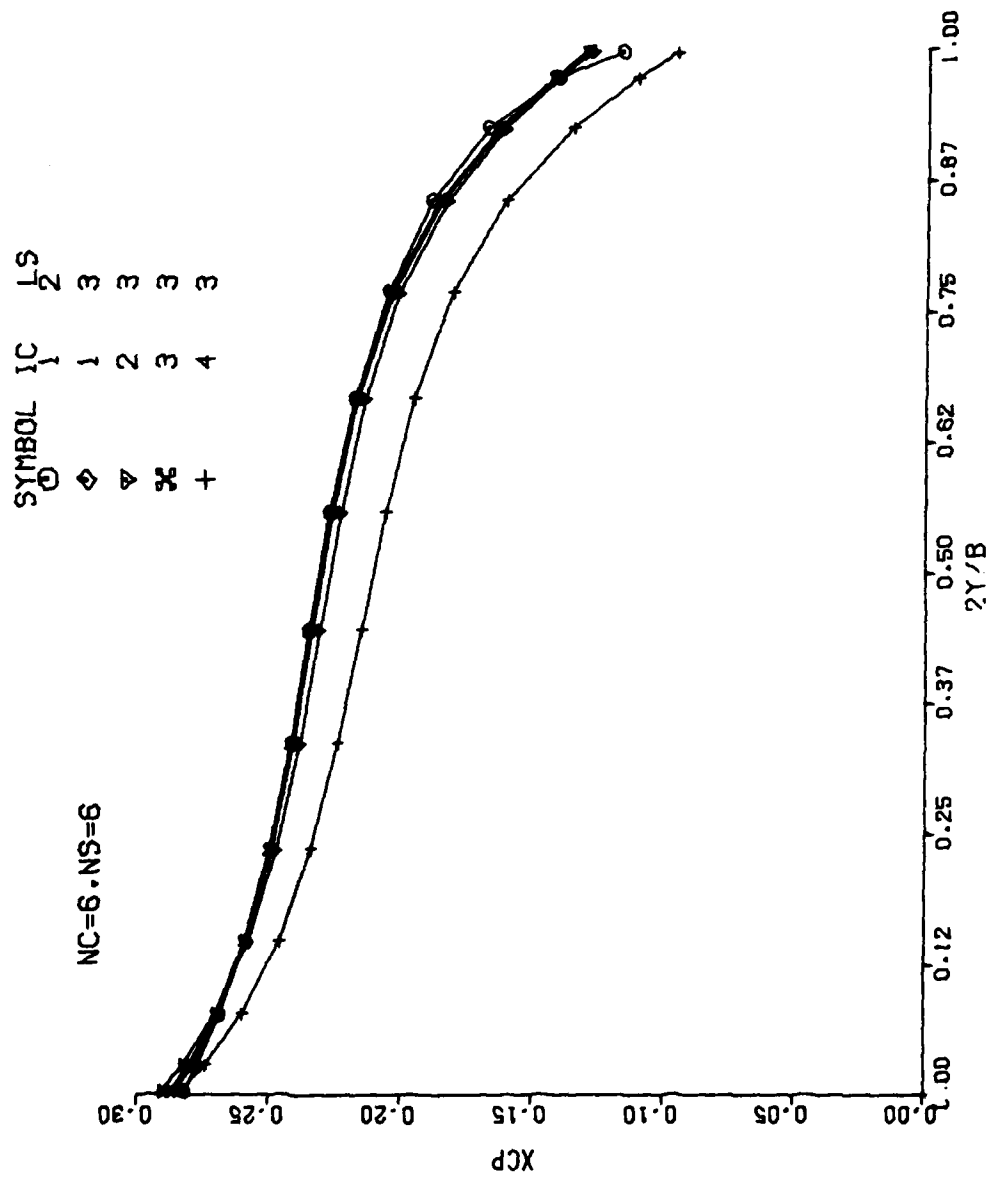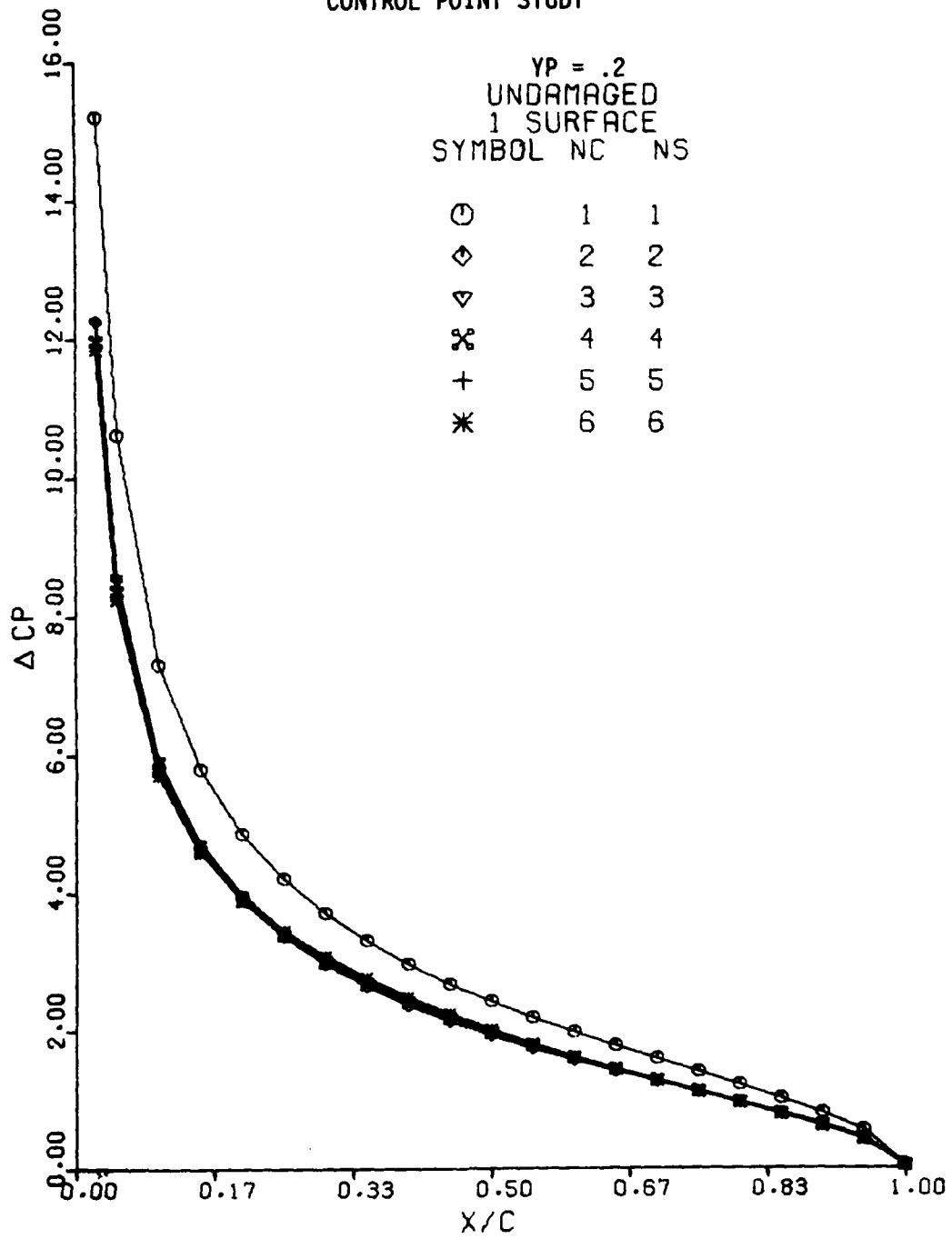
Figure 22

CONTROL POINT STUDY
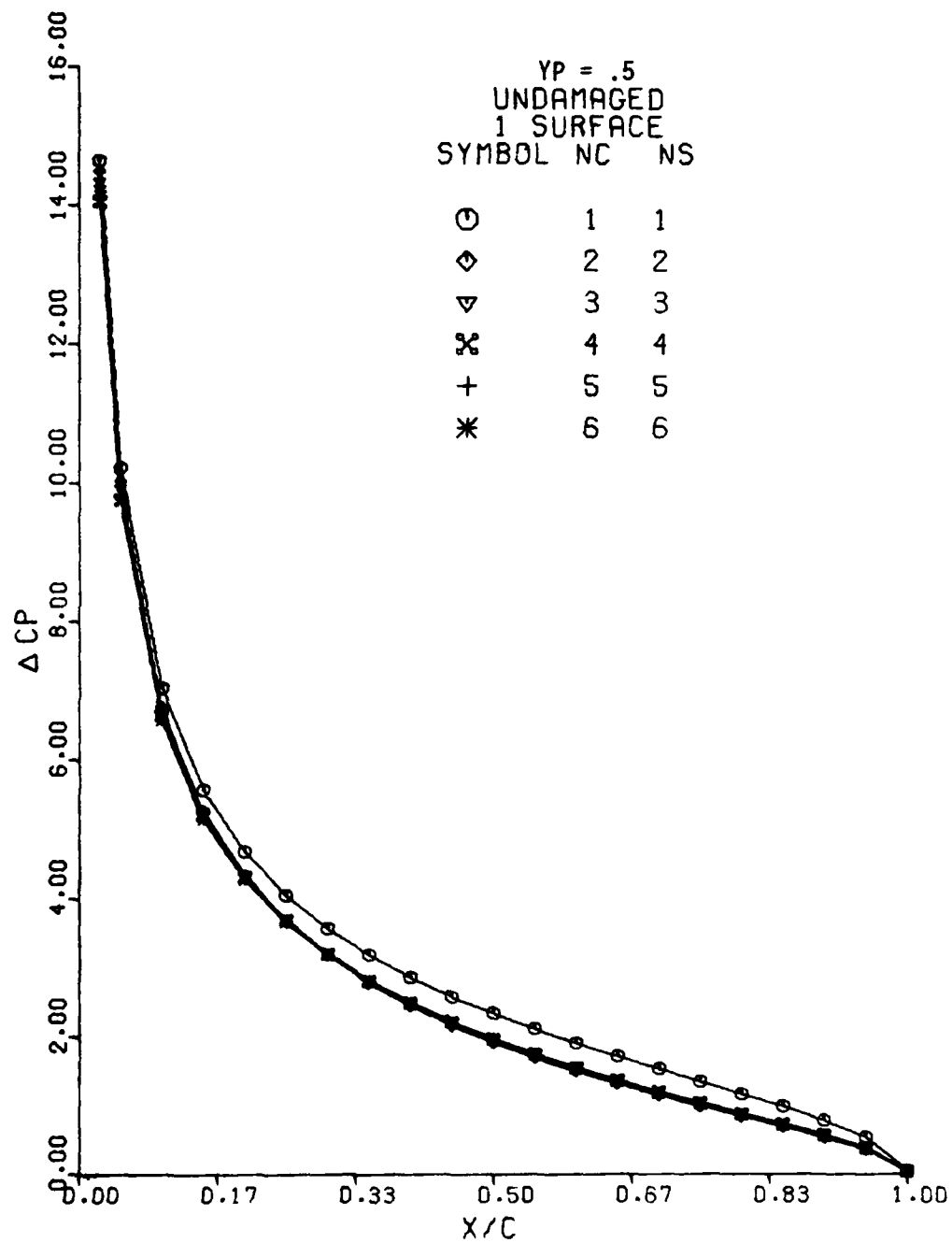
Figure 23

CONTROL POINT STUDY

Figure 24

CONTROL POINT STUDY

UNDAMAGED
1 SURFACE

SYMBOL	NC	NS
⊙	1	1
◇	2	2
▽	3	3
✕	4	4
+	5	5
✳	6	6

Figure 25

108
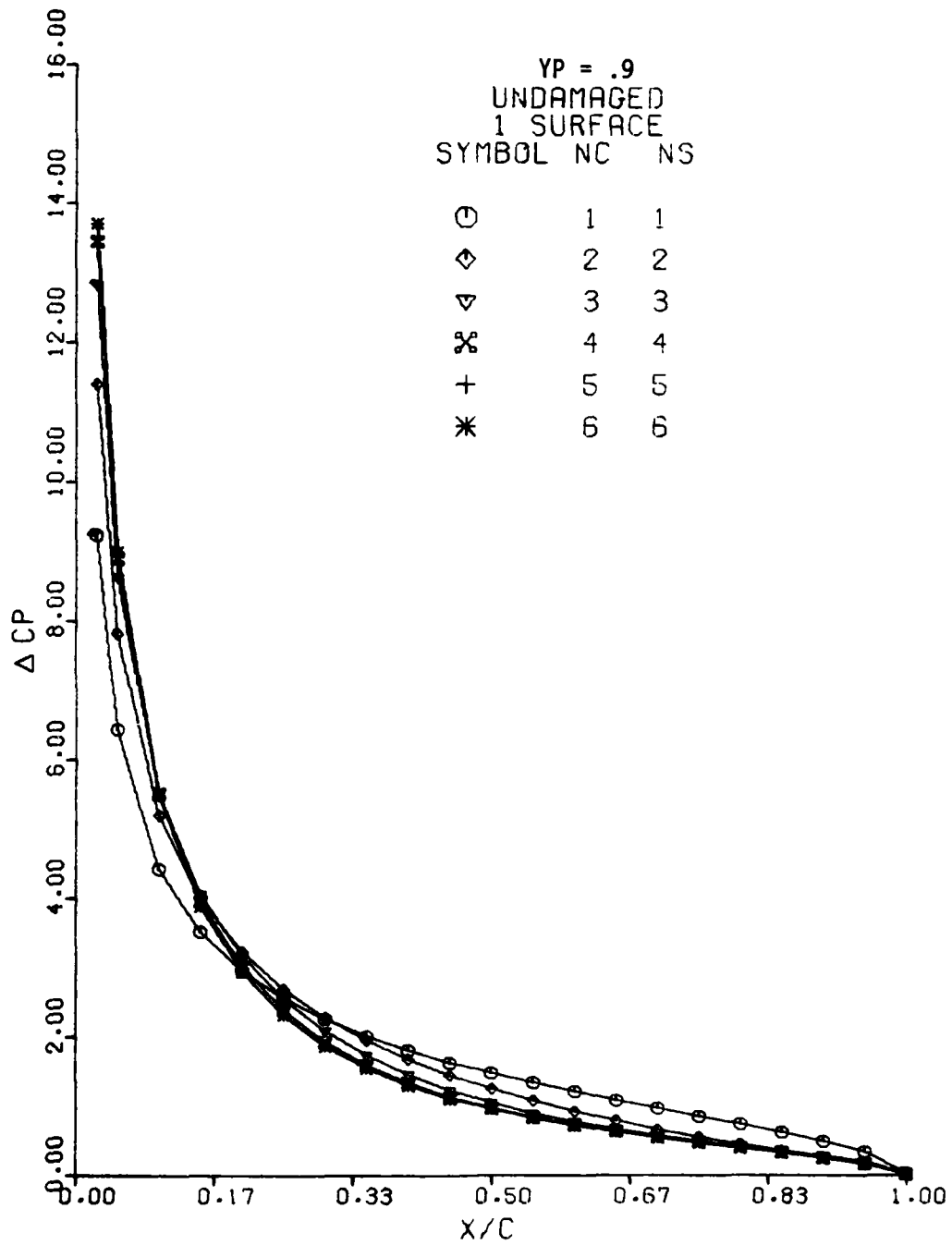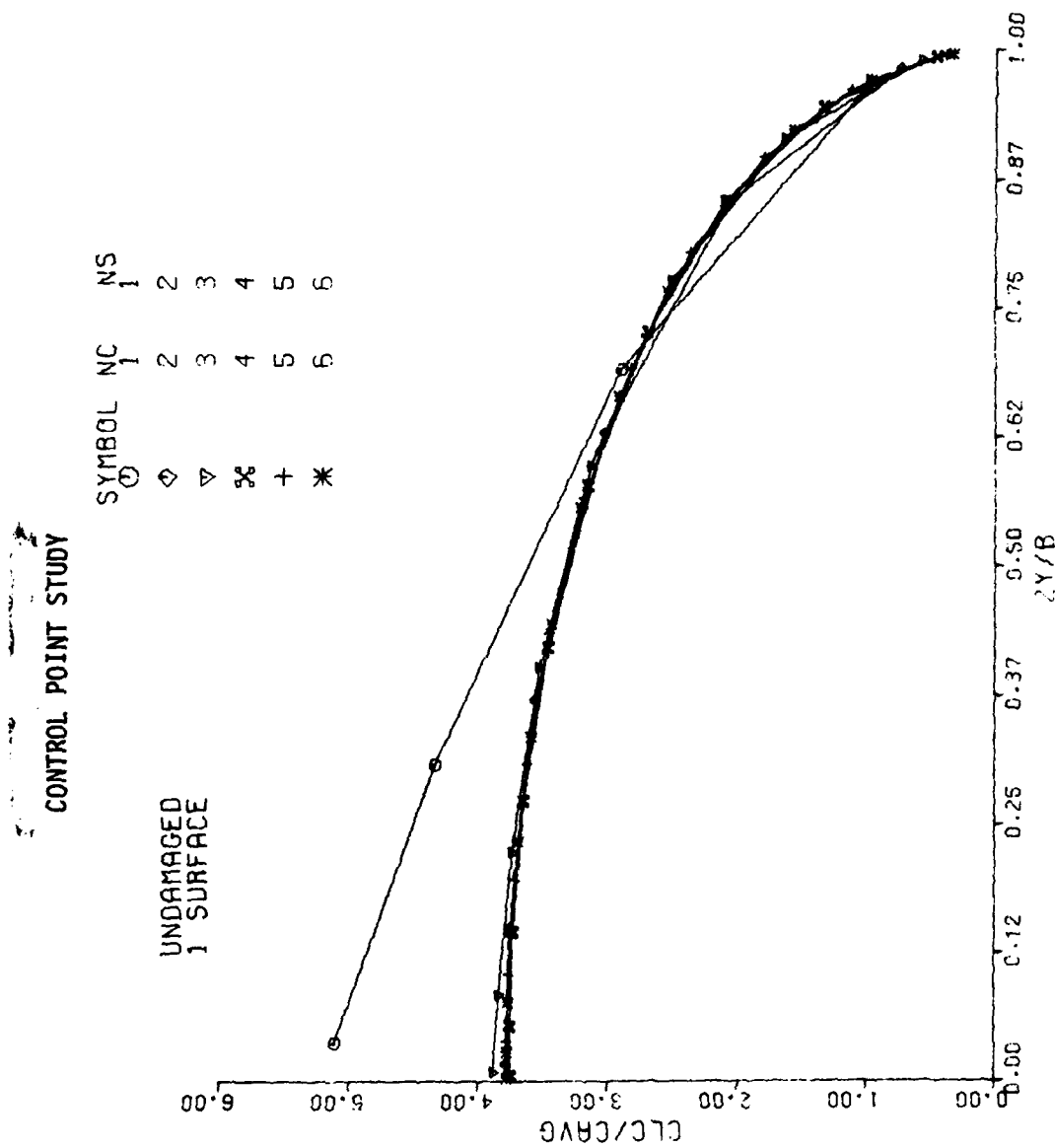
CONTROL POINT STUDY

Figure 26

109
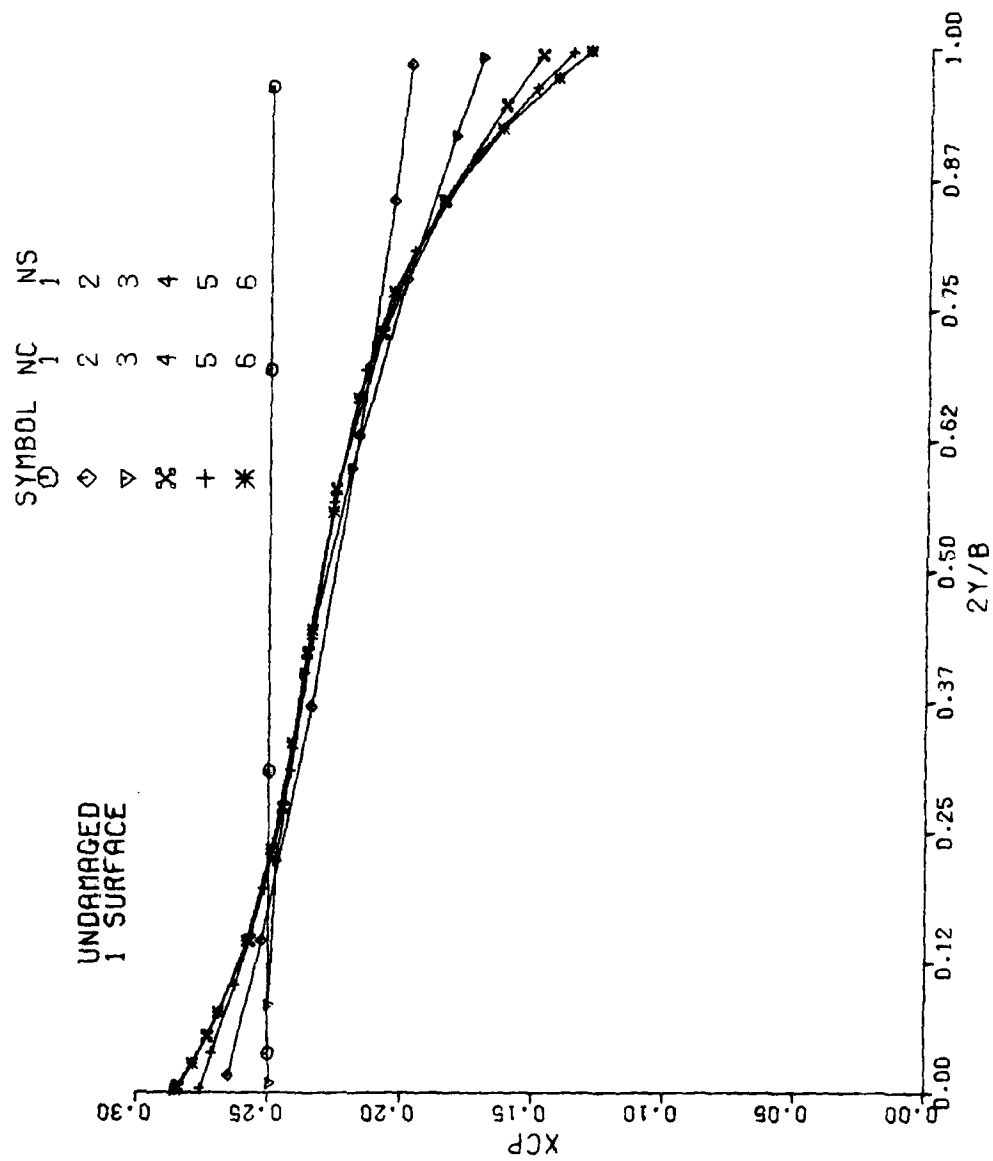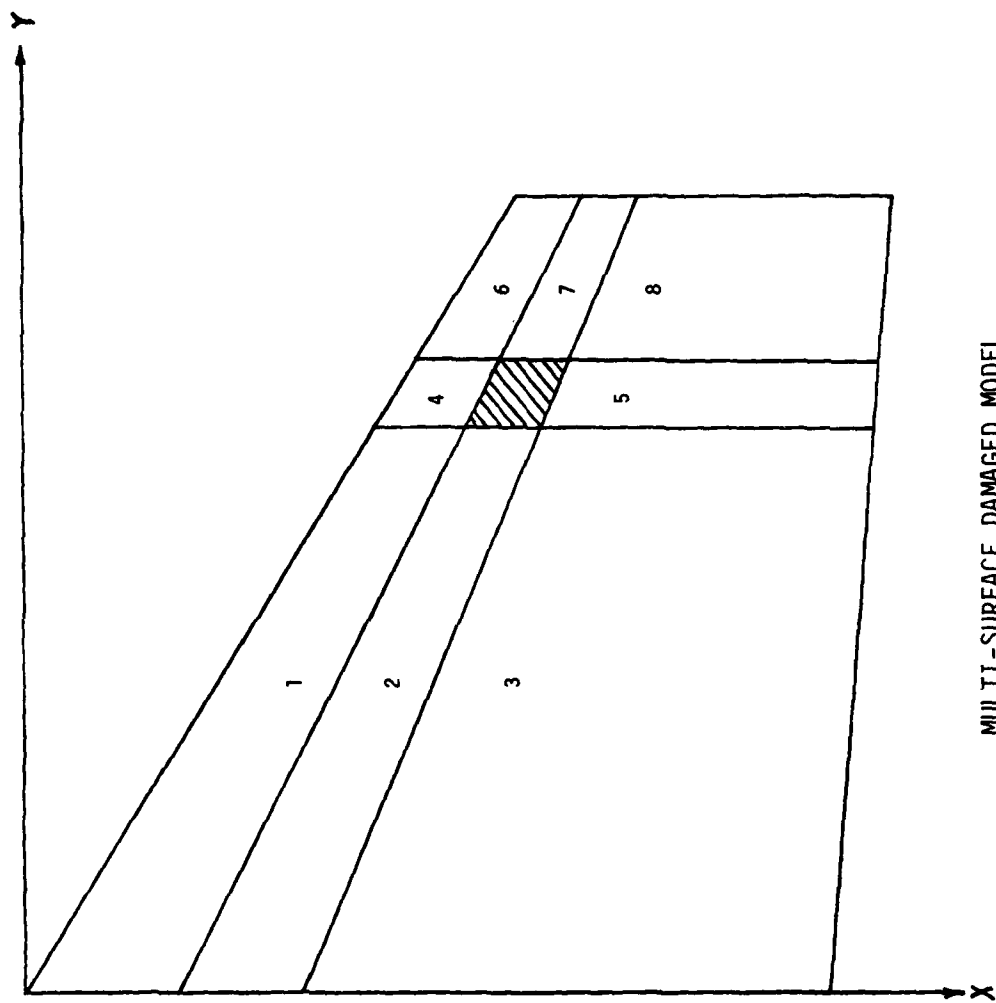
MULTI-SURFACE DAMAGED MODEL

Figure 27

110
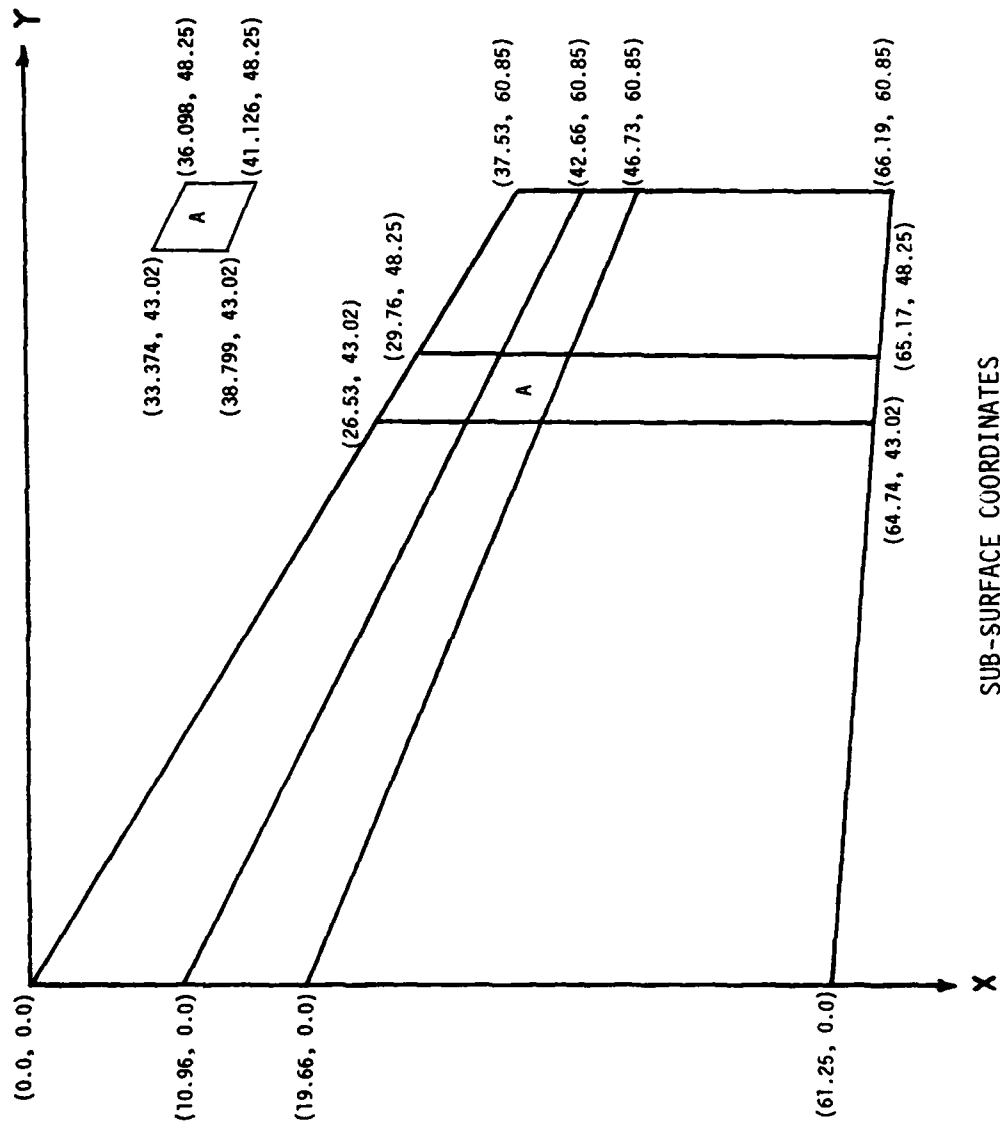
SUB-SURFACE COORDINATES

Figure 28

111
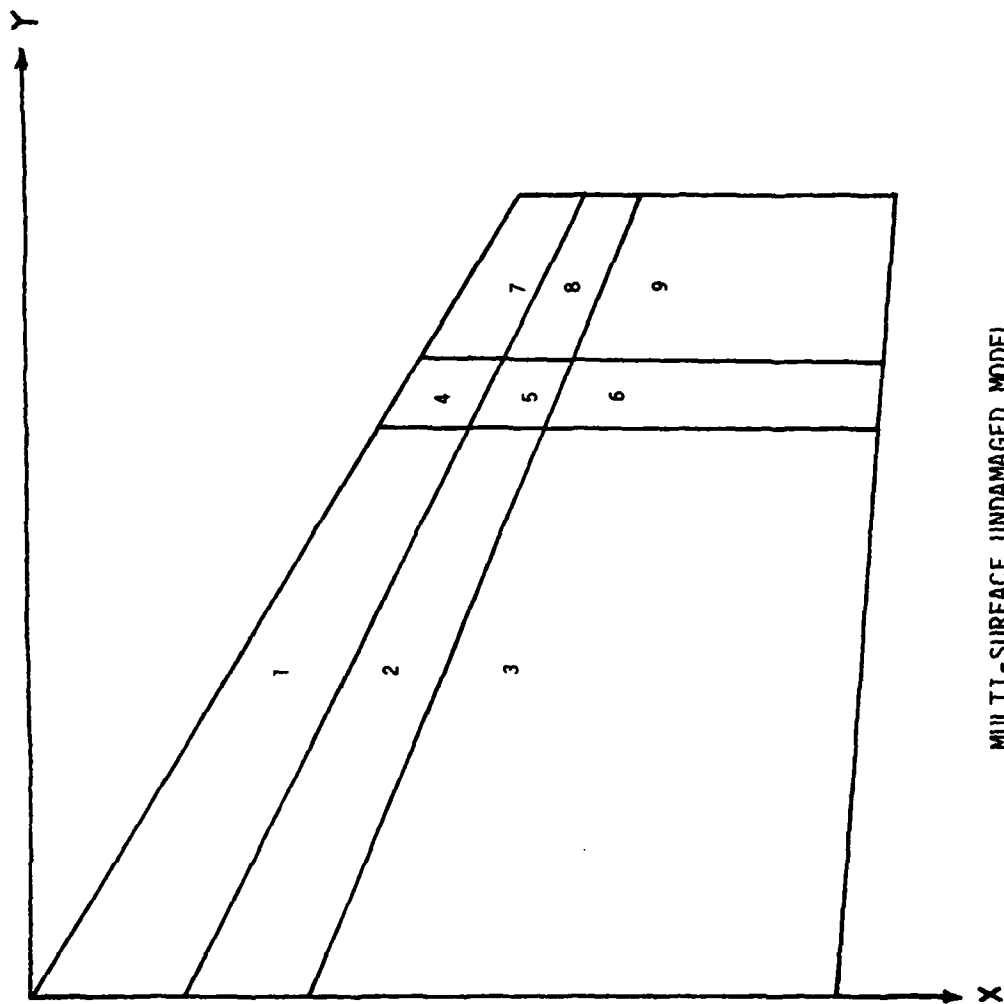
MULTI-SURFACE UNDAMAGED MODEL

Figure 29

112
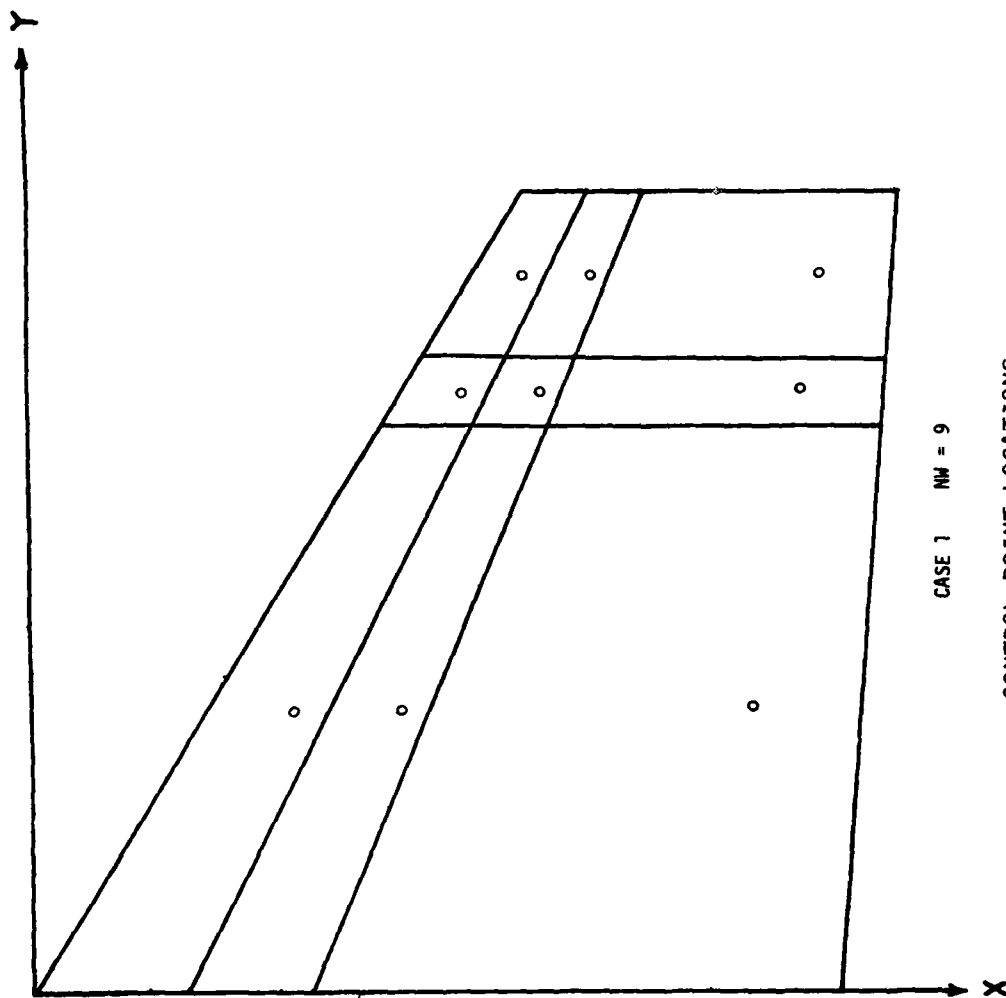
CASE 1   NW = 9

CONTROL POINT LOCATIONS

Figure 30

113
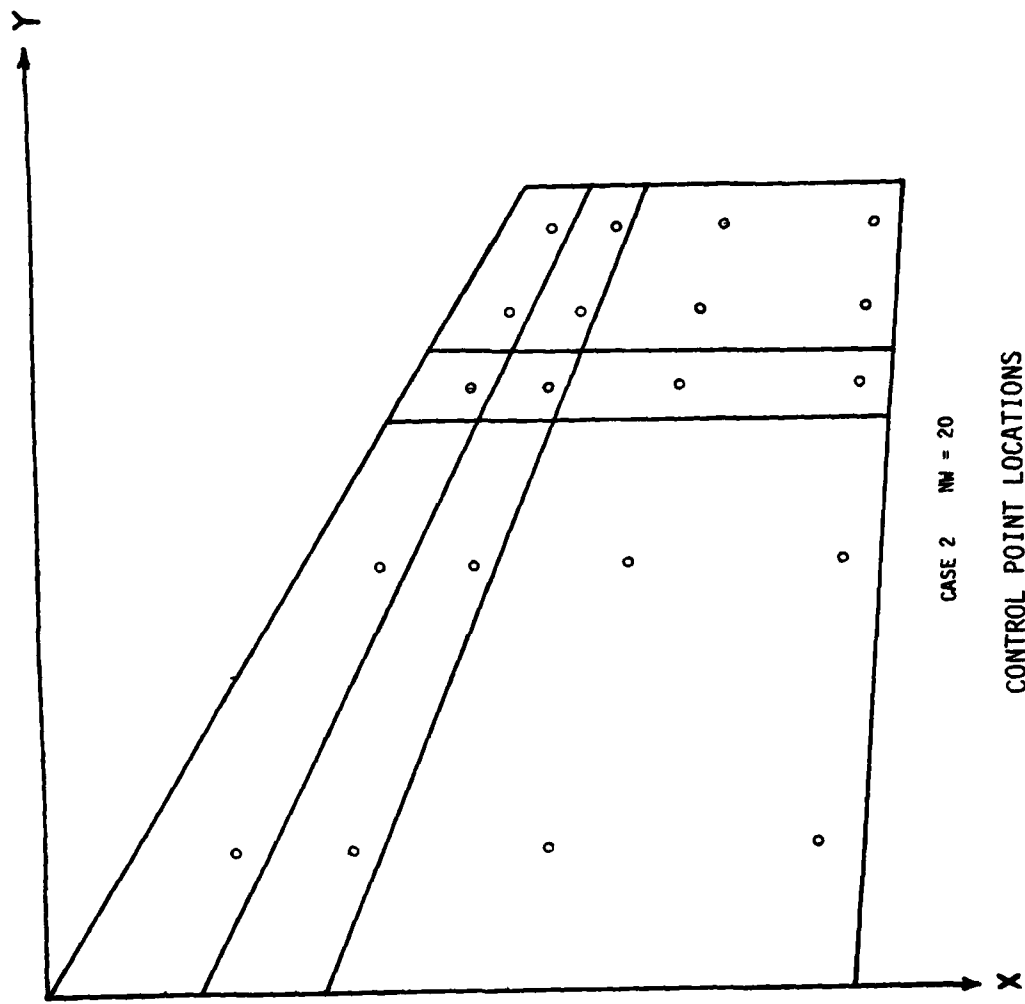
CASE 2   NW = 20

CONTROL POINT LOCATIONS

Figure 31

114

CASE 3   NW = 36

CONTROL POINT LOCATIONS

Figure 32

115

CASE 4   NM = 56

CONTROL POINT LOCATIONS

Figure 33

116

CASE 5   NW = 64
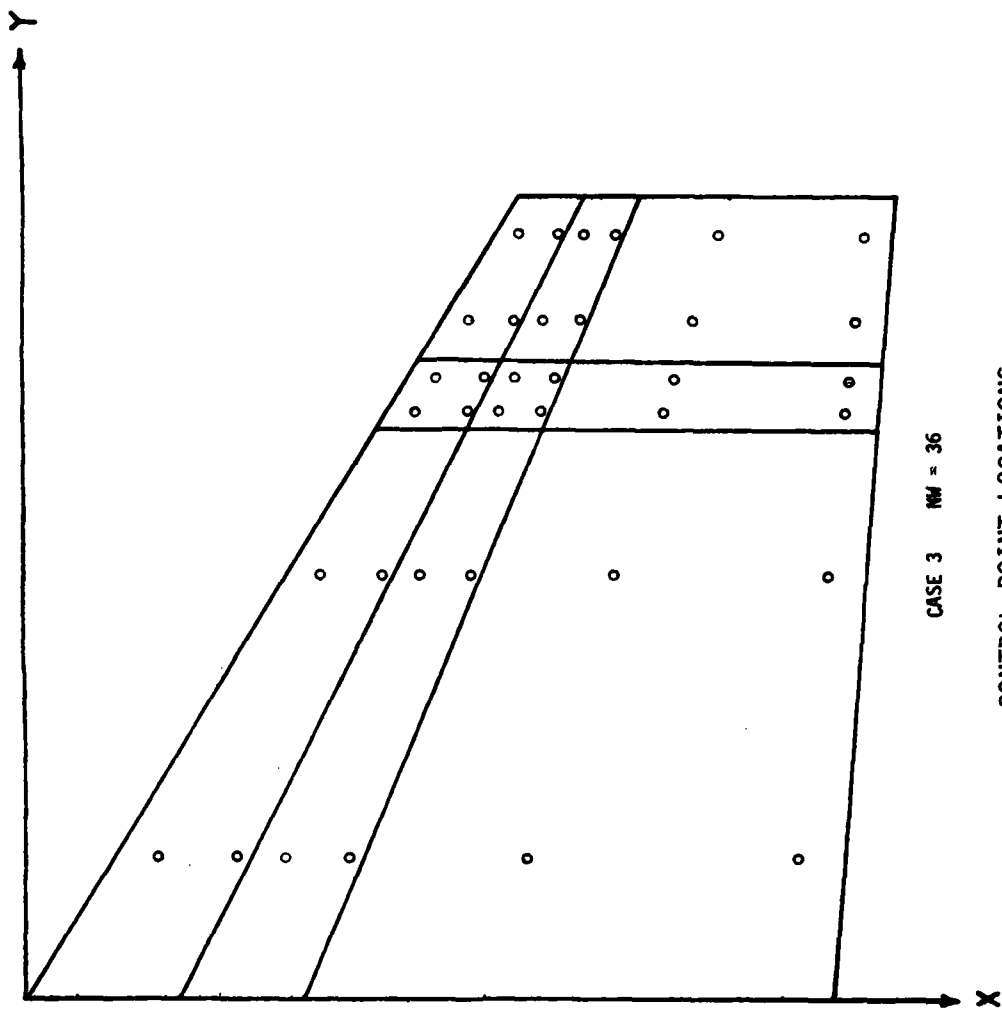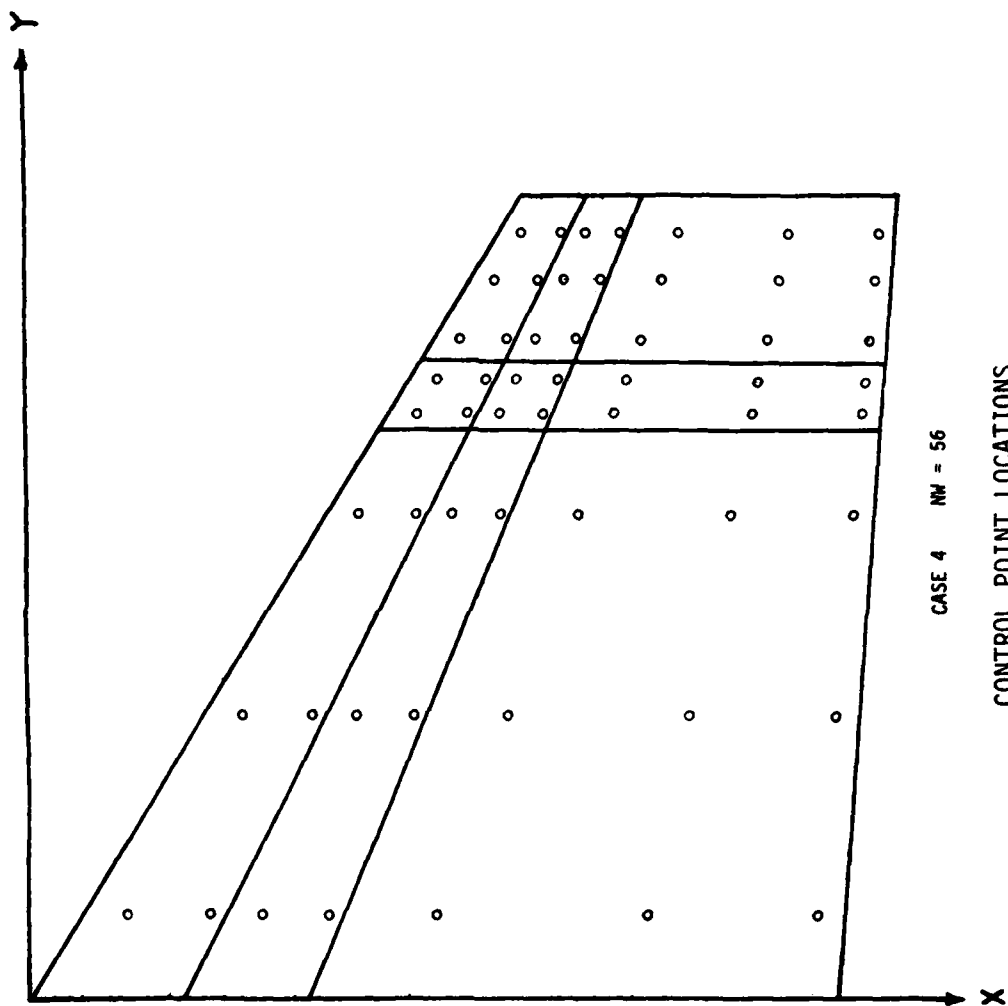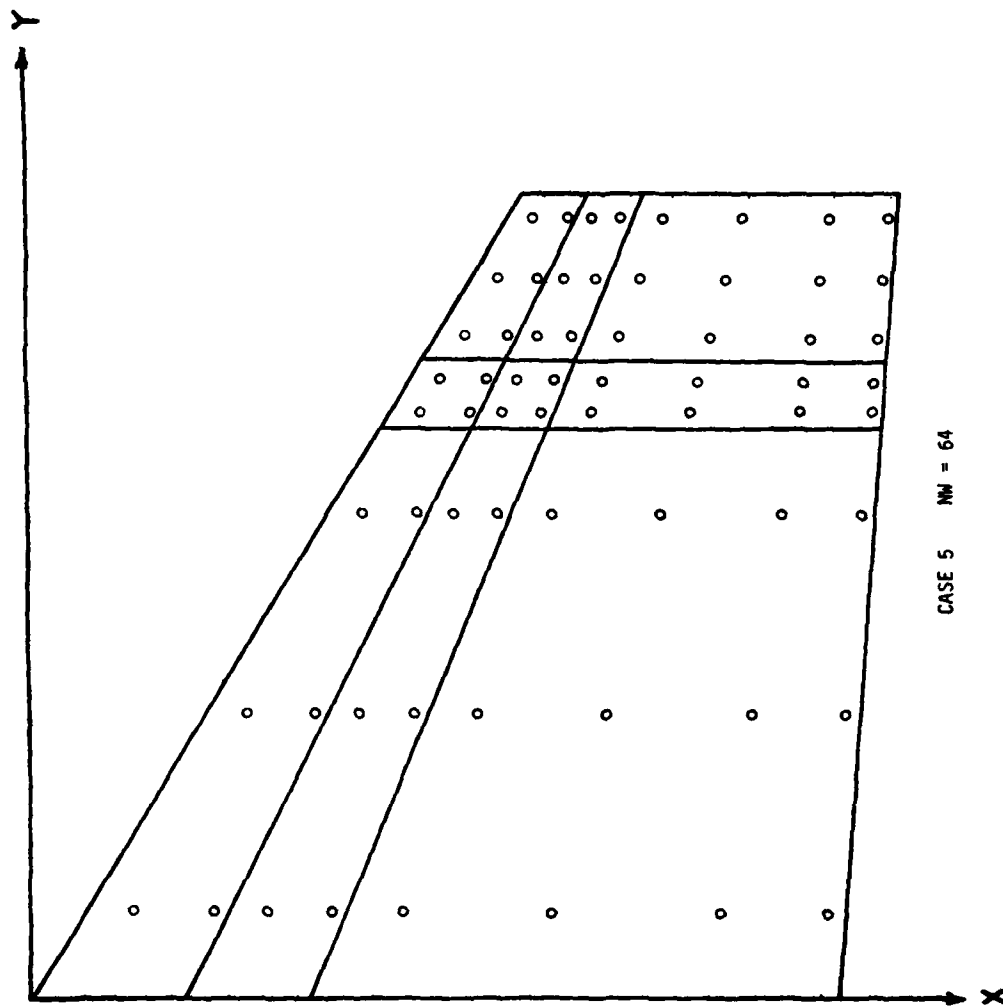
CONTROL POINT LOCATIONS

Figure 34

117
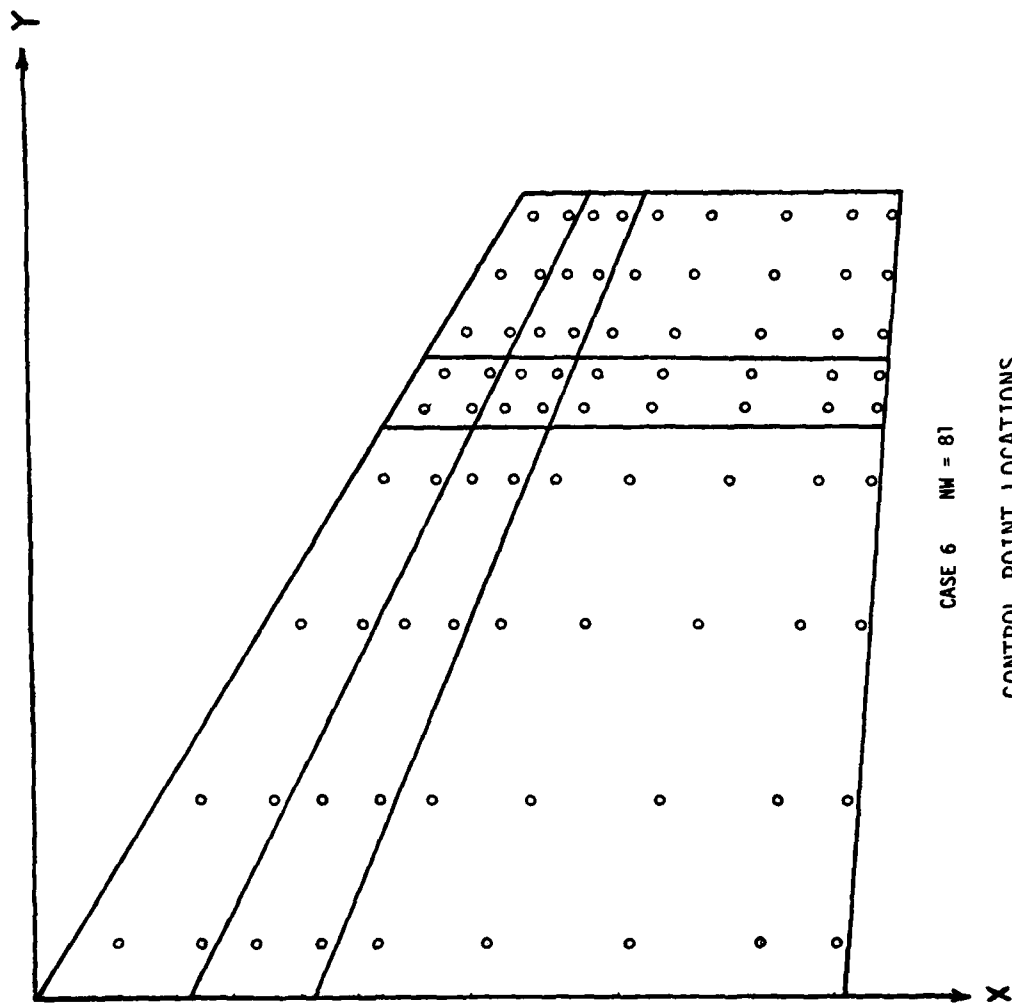
CASE 6   NW = 81

CONTROL POINT LOCATIONS

Figure 35

118
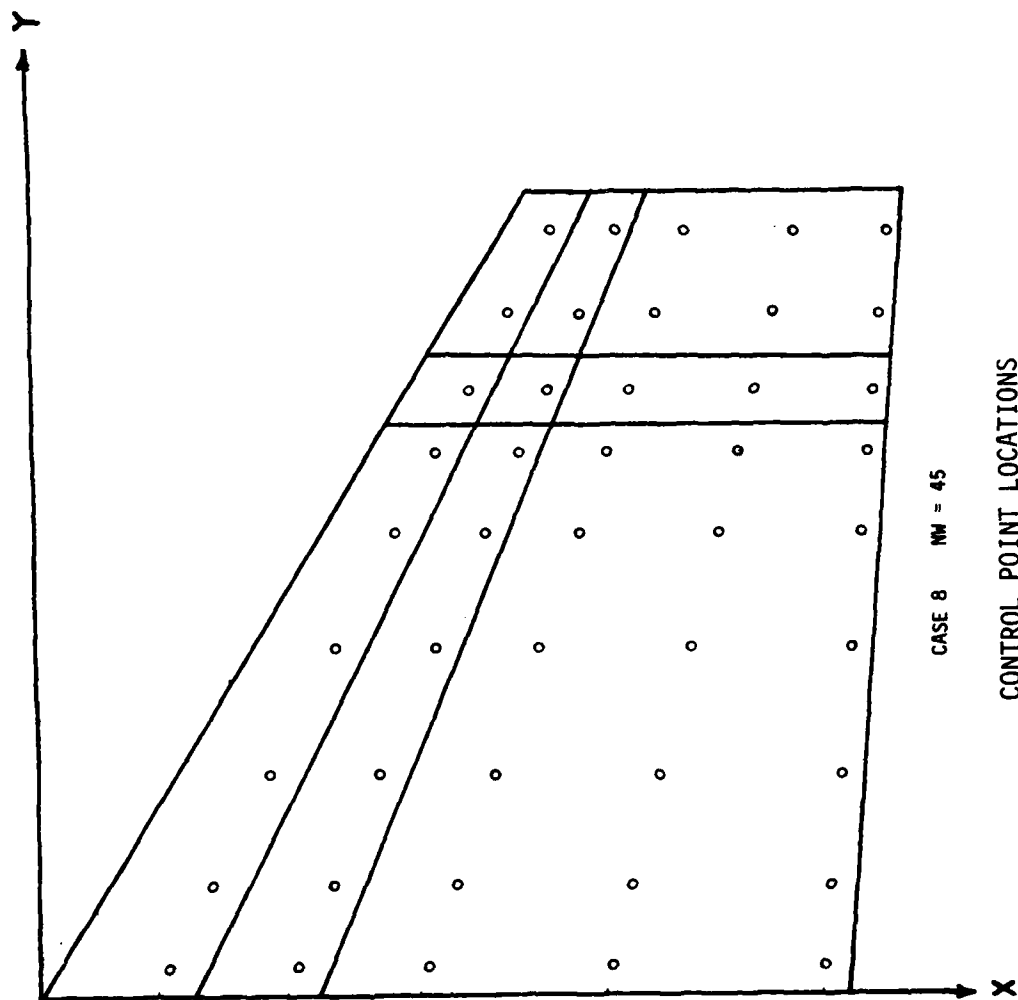
CASE 8   NN = 45

CONTROL POINT LOCATIONS

Figure 36

119

CASE 9   NW = 54
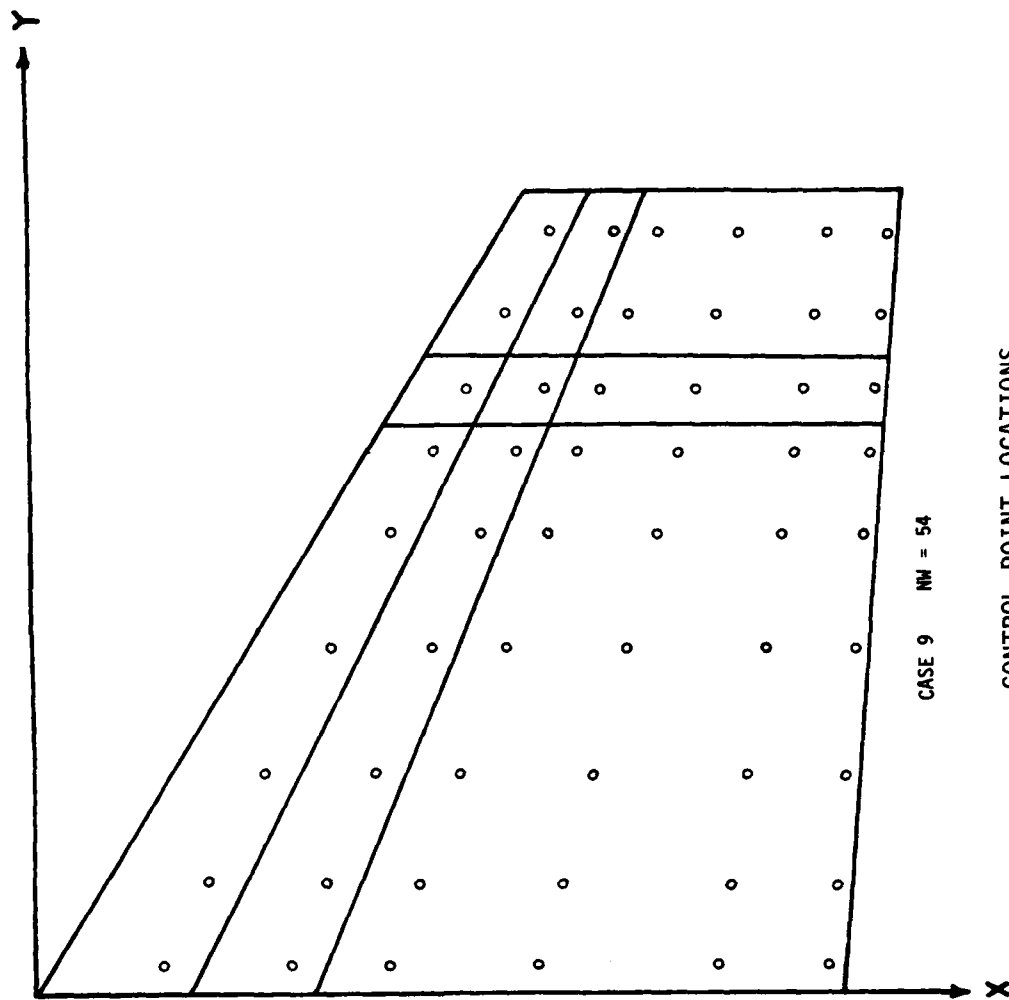
CONTROL POINT LOCATIONS

Figure 37

120
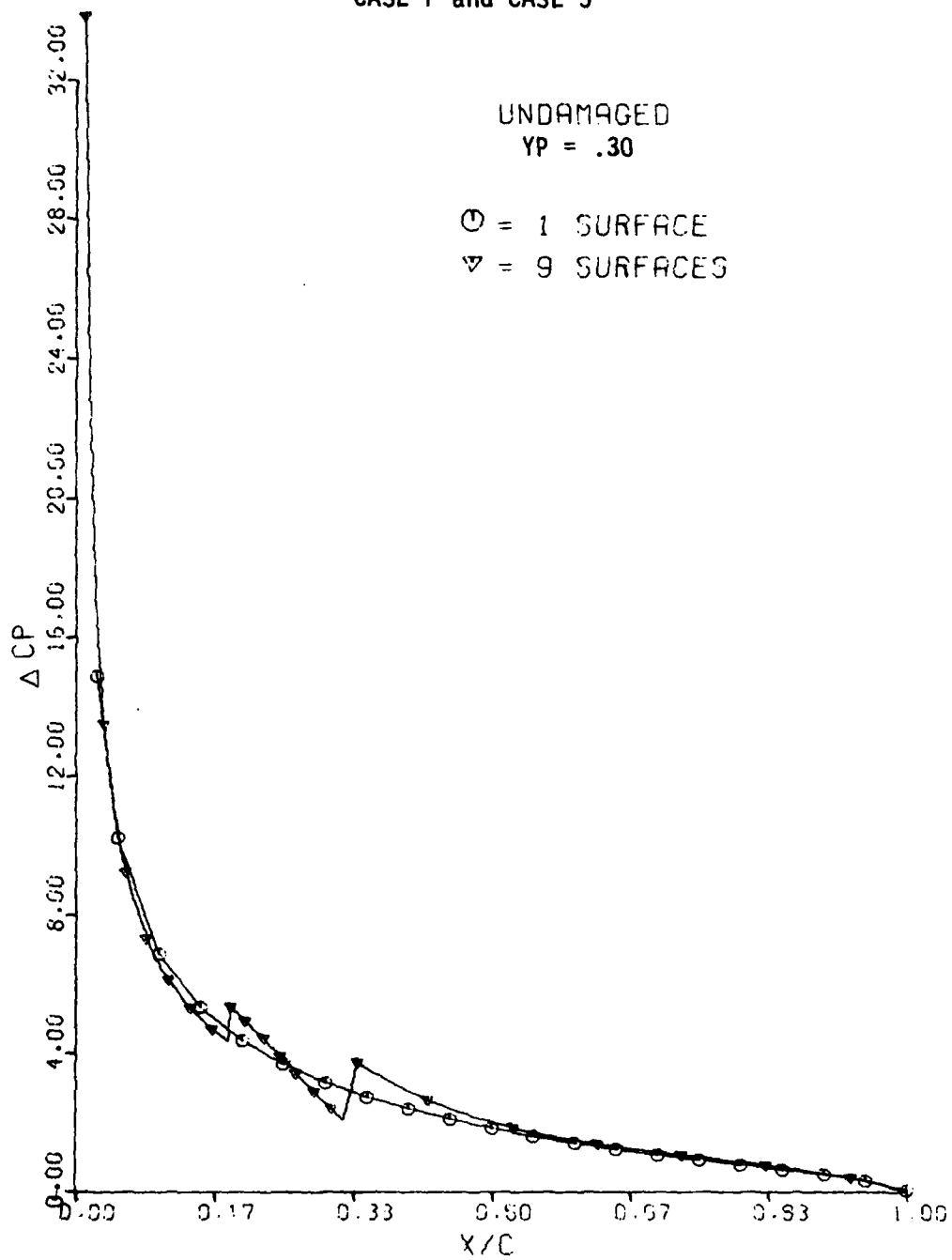
CASE F and CASE 5

Figure 38

CASE F and CASE 5

UNDAMAGED
YP = .65

⊙ = 1 SURFACE
▽ = 9 SURFACES

Figure 39

122
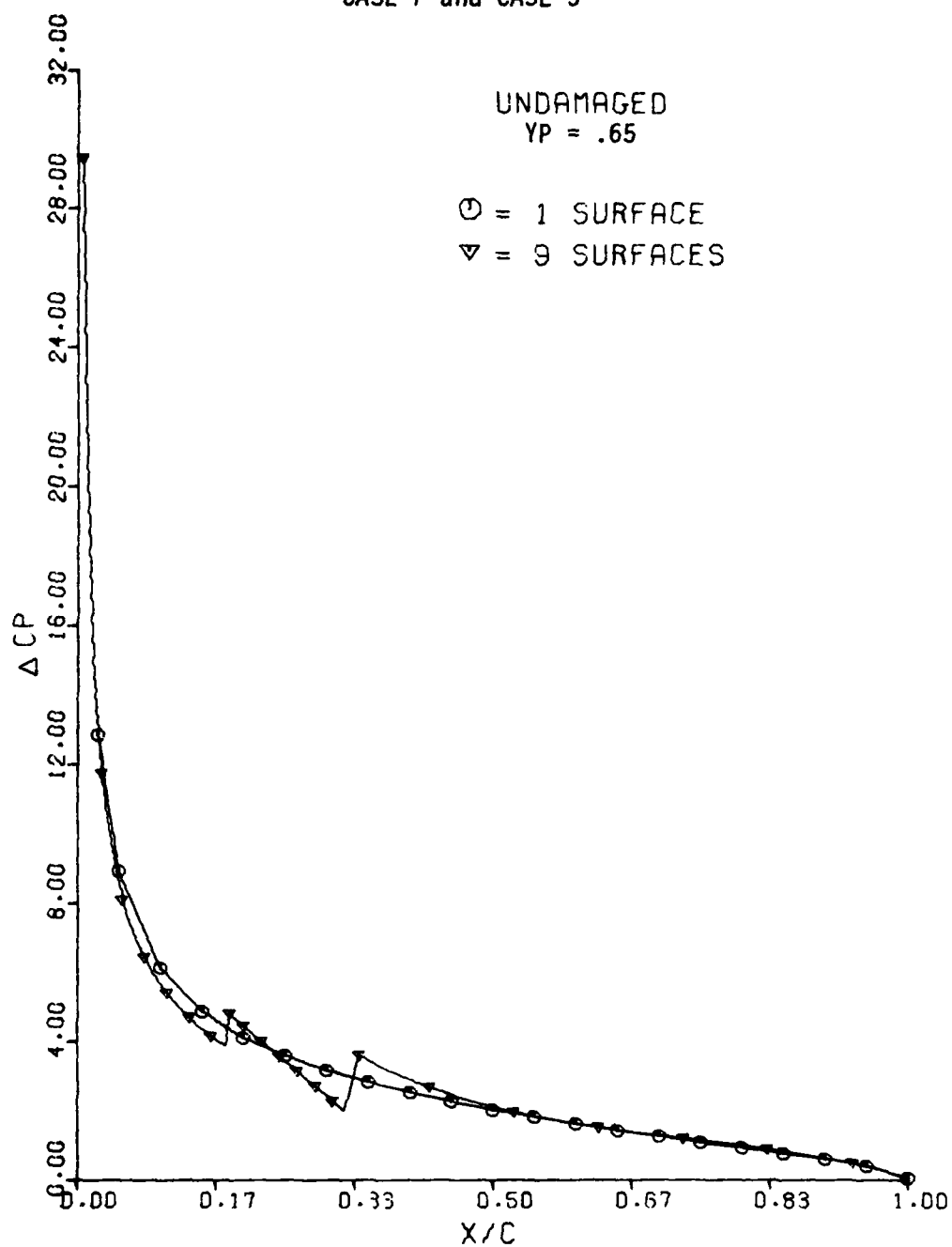
CASE F and CASE 5

Figure 40

123
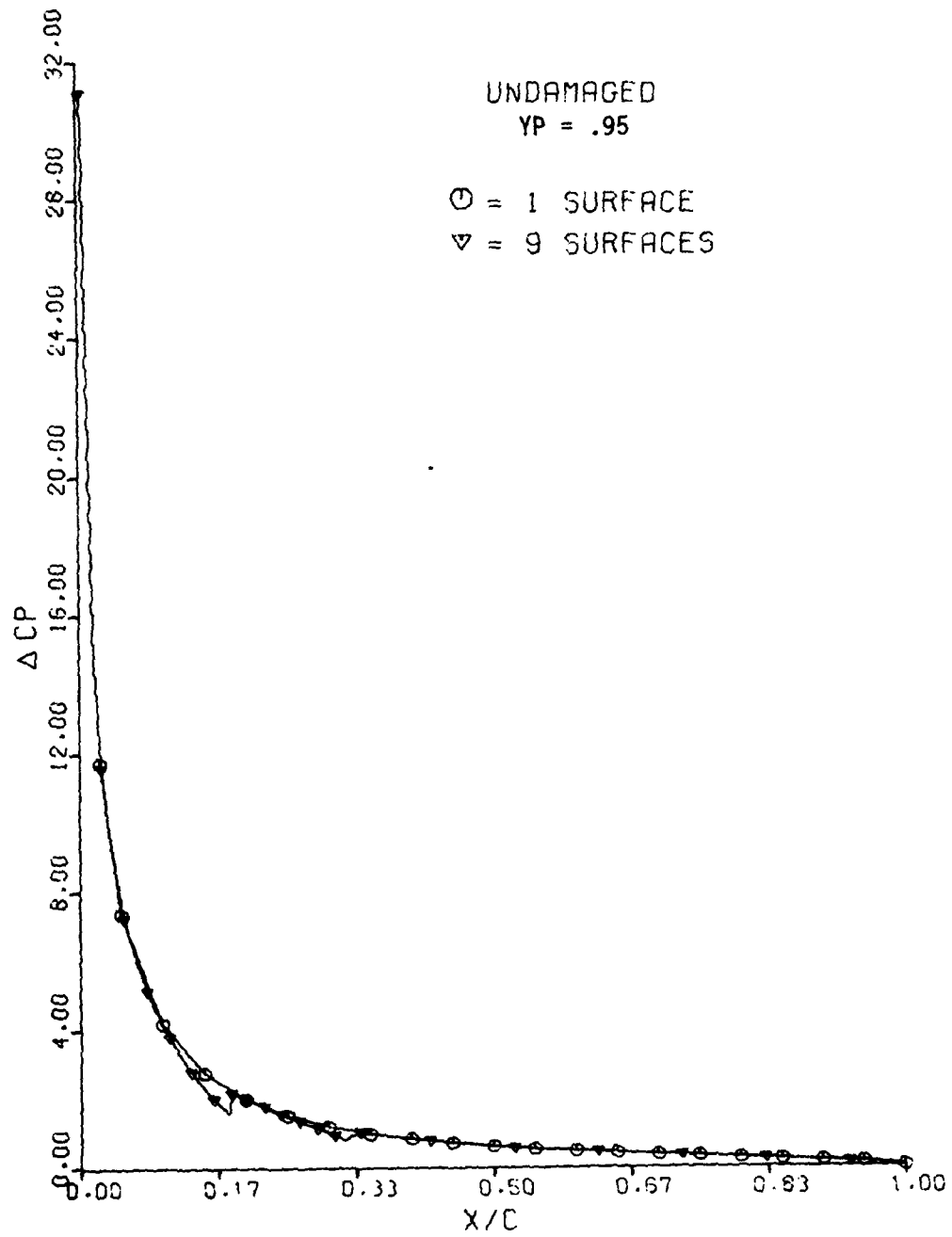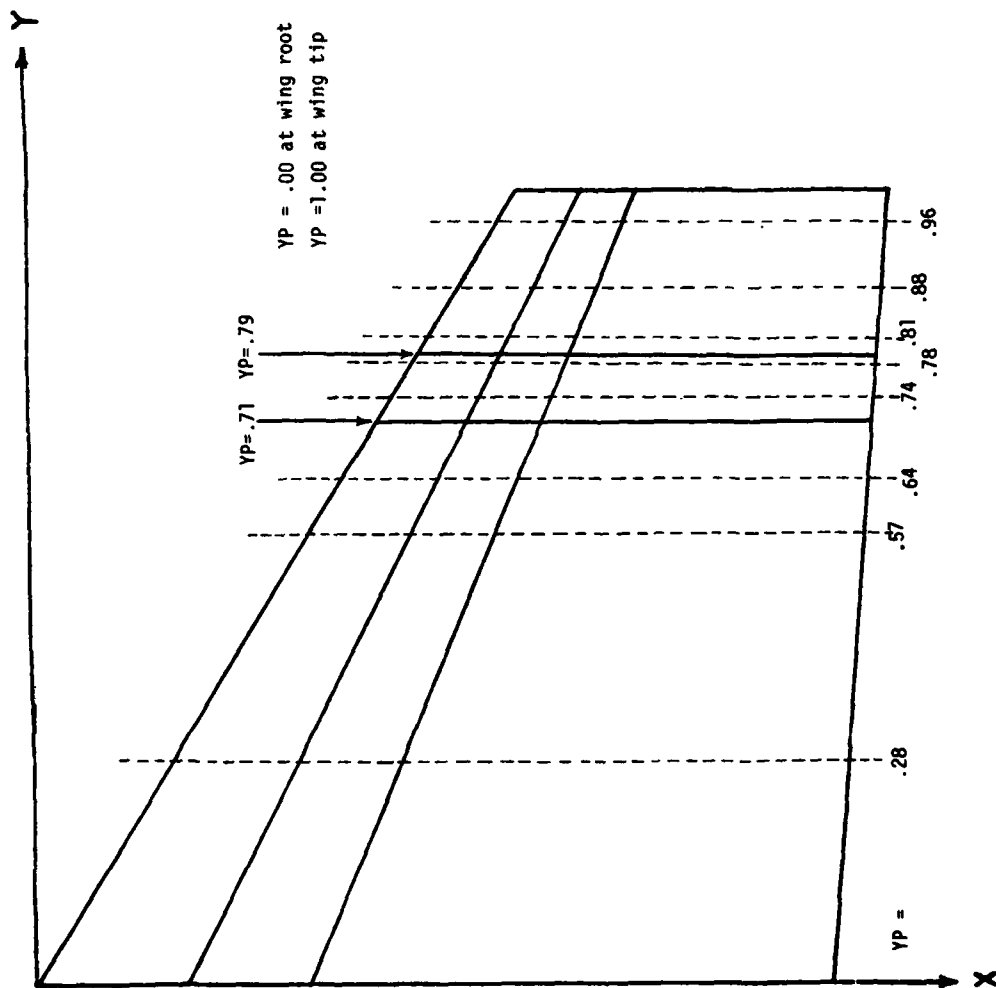
ΔCP PLOT LOCATIONS

Figure 41

CASE 5 and CASE 5D
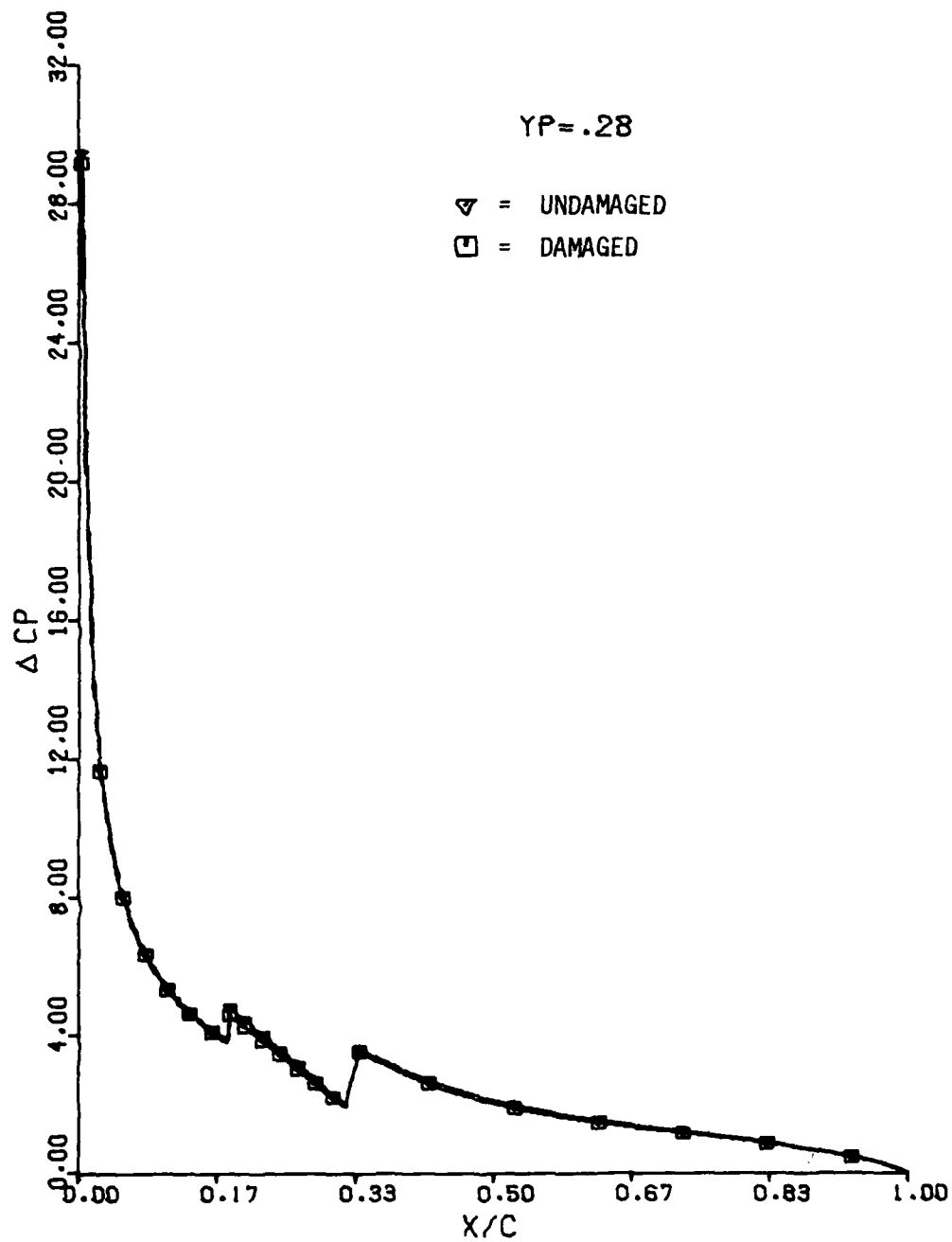
Figure 42
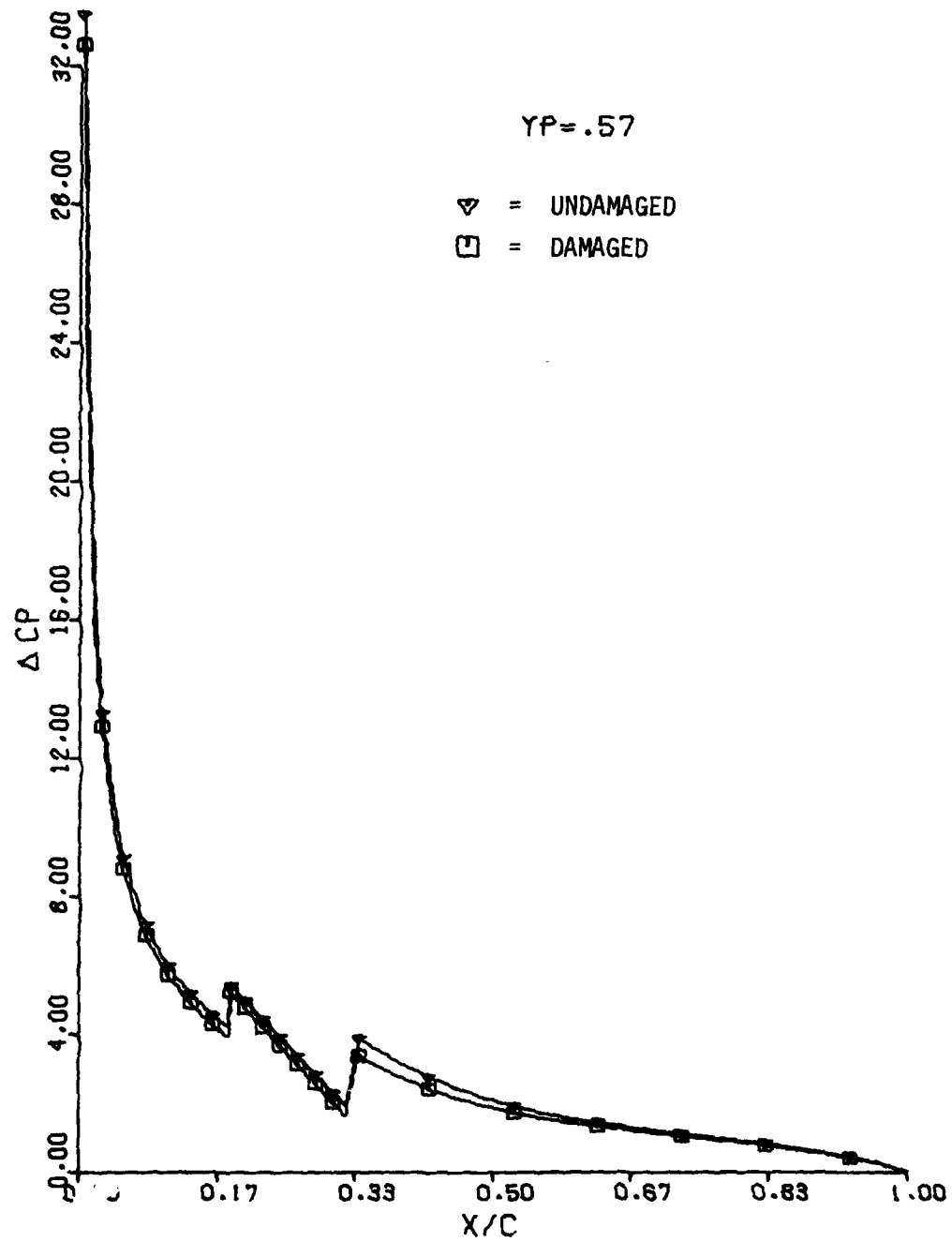
125

CASE 5 and CASE 5D

YP=.57

▽ = UNDAMAGED

⬚ = DAMAGED

Figure 43

126

CASE 5 and CASE 5D

YP=.64

▽ = UNDAMAGED
◻ = DAMAGED

Figure 44

127

CASE 5 and CASE 5D

Figure 45

128

CASE 5 and CASE 5D

YP=.78

▽ =UNDAMAGED
▢ =DAMAGED

Figure 46

CASE 5 and CASE 5D

YP=.81

▽ = UNDAMAGED
◻ = DAMAGED

Figure 47

130
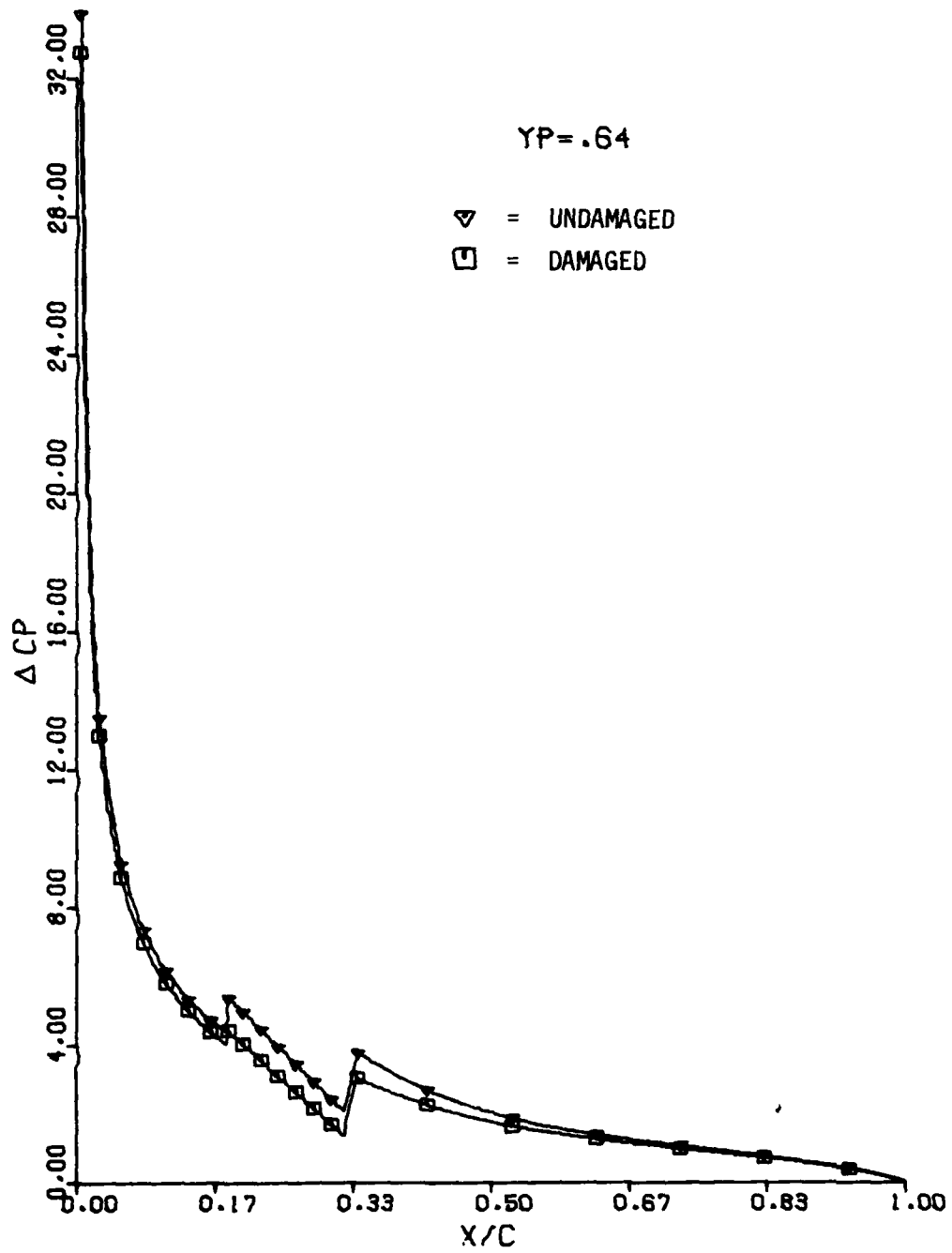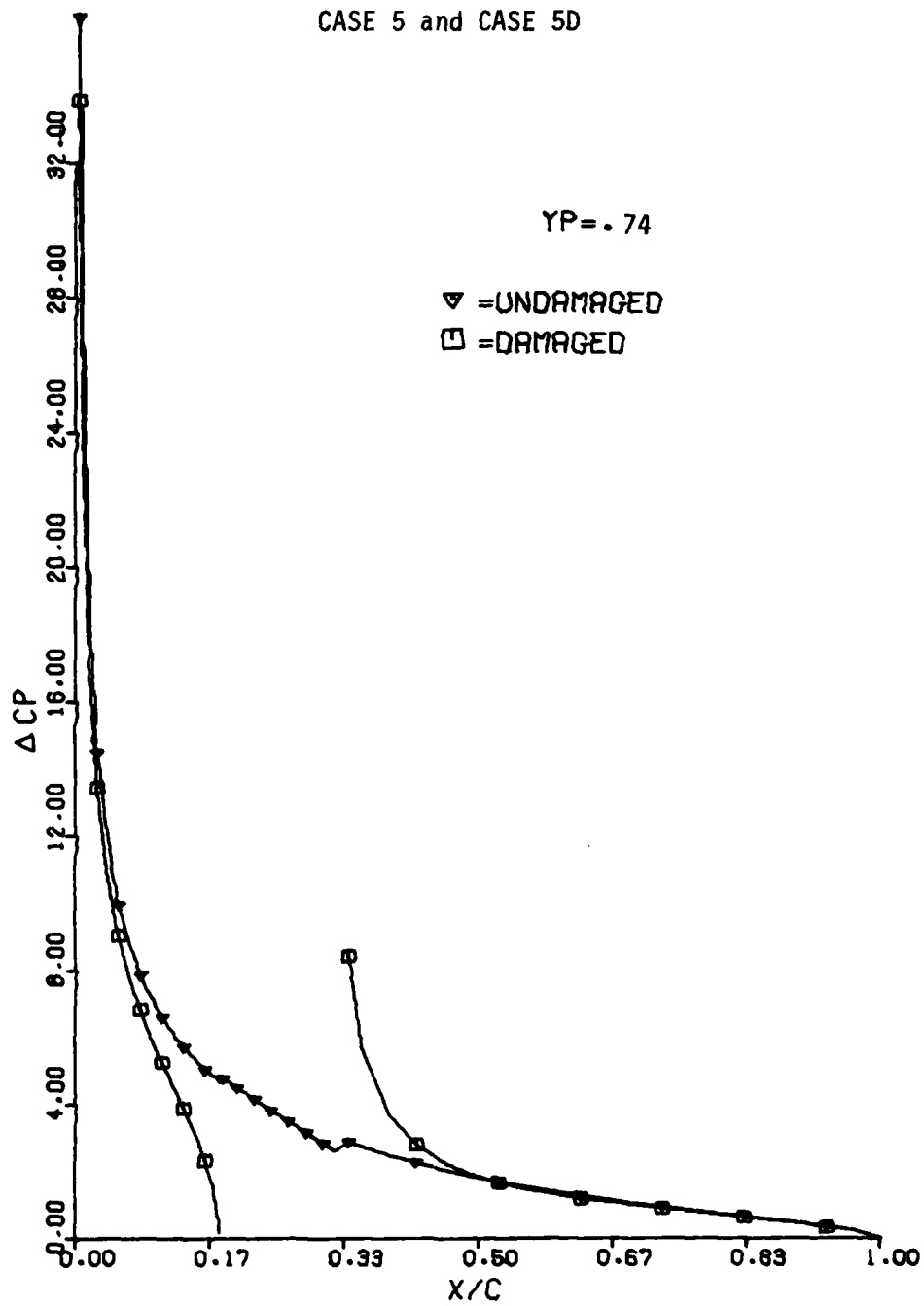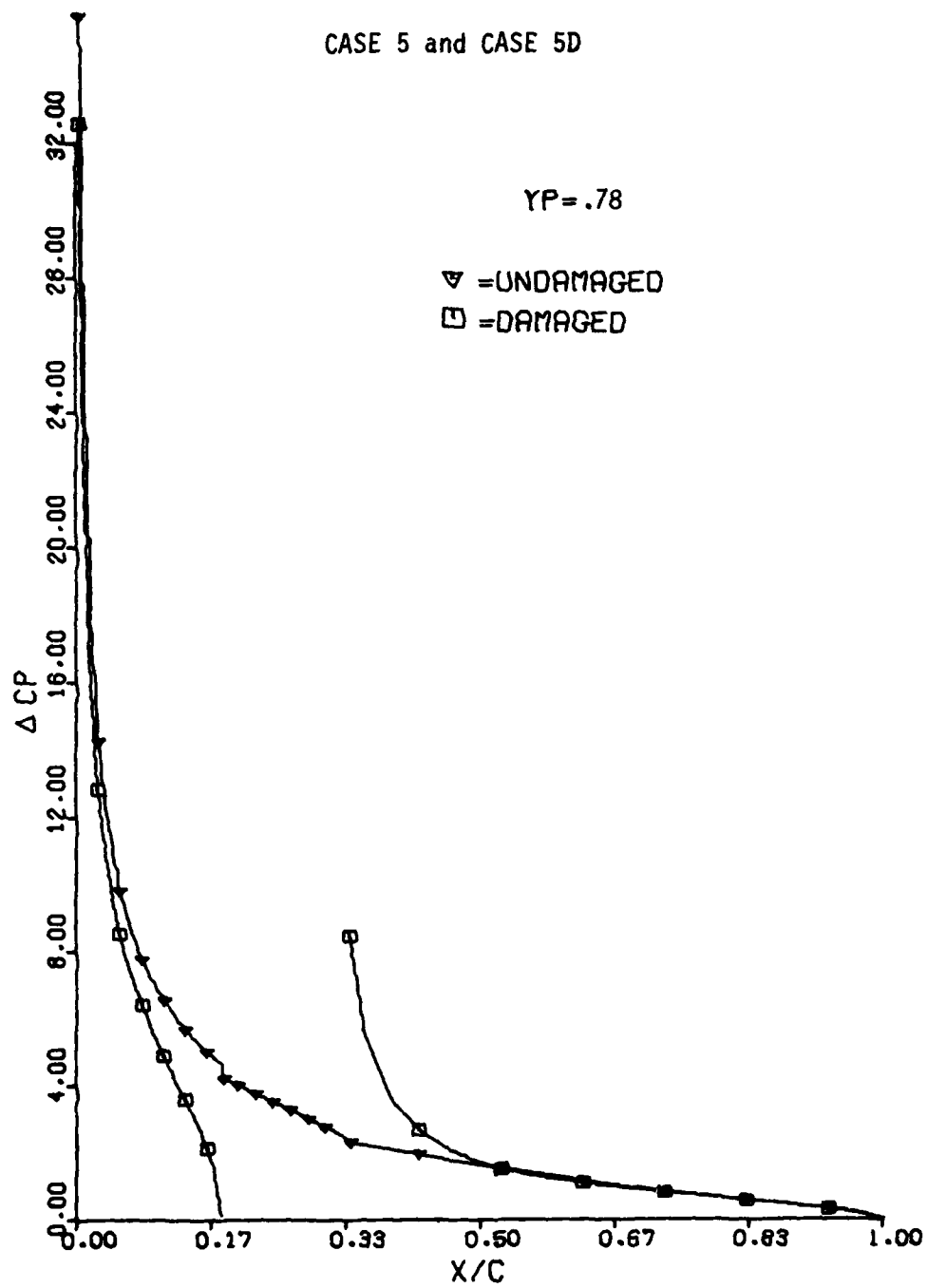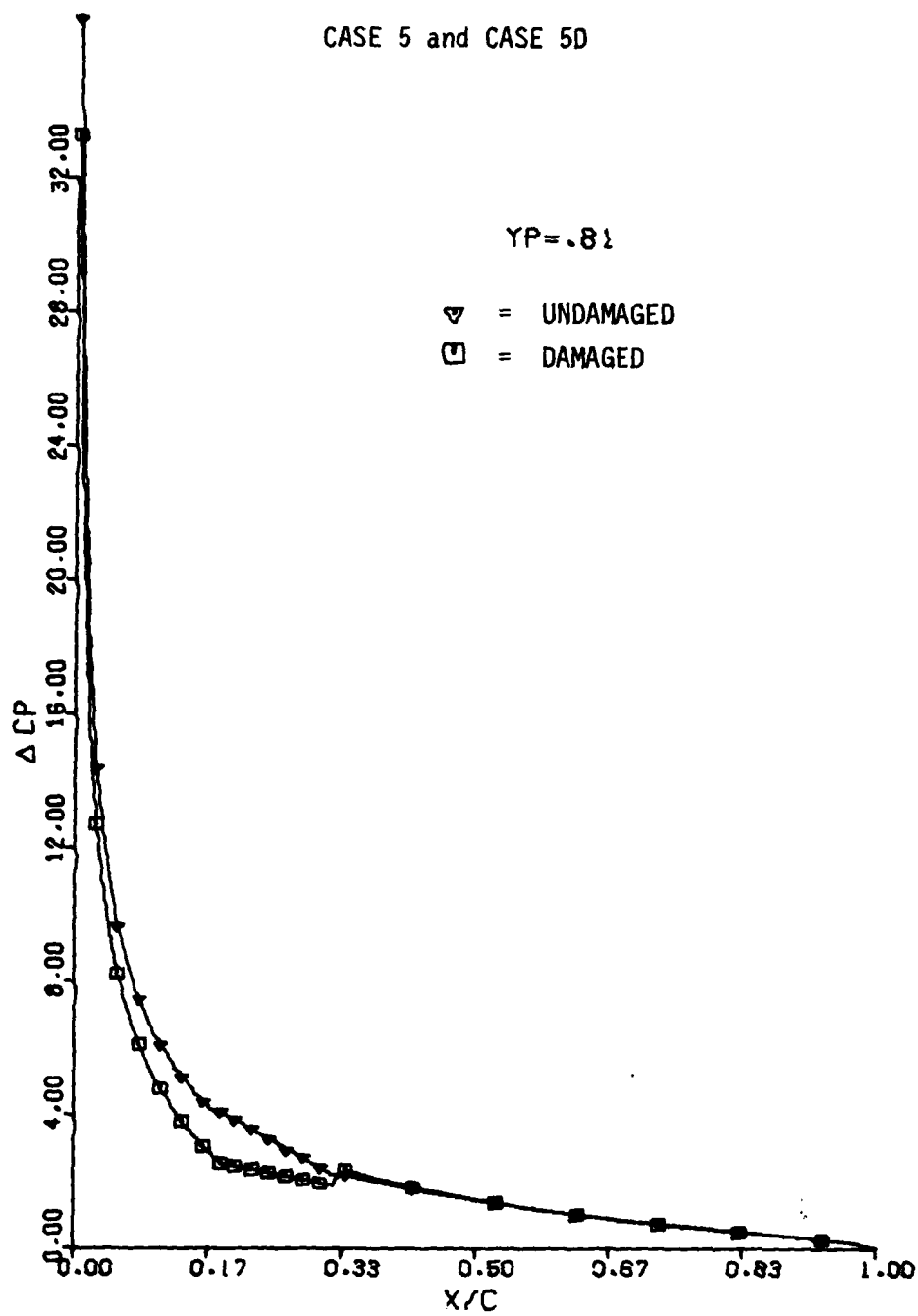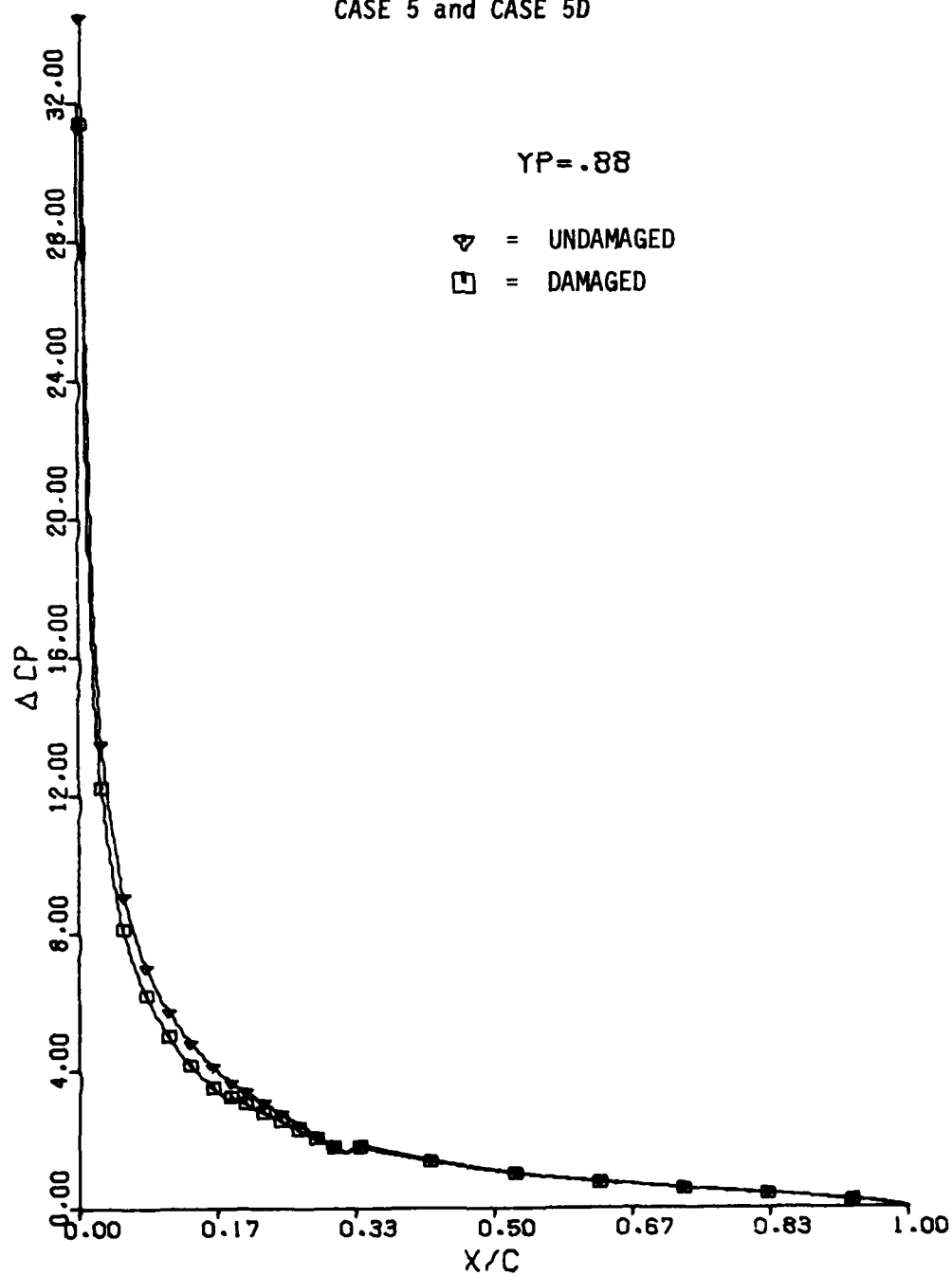
CASE 5 and CASE 5D

Figure 48

CASE 5 and CASE 5D

YP=.96

▽ = UNDAMAGED

⊡ = DAMAGED

Figure 49

132

CASE F

⊙ = UNDAMAGED, 1 SURFACE

AND
CASE 5

▽ = UNDAMAGED, 9 SURFACES

Figure 50

133

CASE 5
AND
CASE 50

▽ = UNDAMAGED, 9 SURFACES
⊡ = DAMAGED, 8 SURFACES

CLC/CAVG

2Y/B

0.00 0.12 0.25 0.37 0.50 0.62 0.75 0.87 1.00

0.00 0.80 1.60 2.40 3.20 4.00

Figure 51

134

CASE F   ⊙ = UNDAMAGED, 1 SURFACE
AND
CASE 5D   ⊡ = DAMAGED,   8 SURFACES

2Y/B

CLC/CAVG

Figure 52

135

CASE 5 ▽ = UNDAMAGED, 9 SURFACES

AND

CASE 7D ◇ = DAMAGED, 8 SURFACES, No Kutta Conditions

Figure 53

136

CASE 5D   □ = DAMAGED, 8 SURFACES

AND

CASE 7D   ◇ = DAMAGED, 8 SURFACES, No Kutta Conditions

Figure 54

137

CASE F   ⊕ = UNDAMAGED, 1 SURFACE
AND
CASE 7D   ◇ = DAMAGED, 8 SURFACES, No Kutta Condition

Figure 55

138

CASE F and CASE 8

UNDAMAGED

YP=.35

○ = 1 SURFACE
△ = 9 SURFACES

Figure 56

139

CASE F and CASE 8

UNDAMAGED
YP=.65

Figure 57

CASE F and CASE 8

UNDAMAGED
YP=.95

⊙ = 1 SURFACE
▲ = 9 SURFACES

Figure 58

ΔCP PLOT LOCATIONS

Figure 59

142

CASE 8 and CASE 8D

YP=.53

△ = UNDAMAGED
✳ = DAMAGED

Figure 60

143

CASE 8 and CASE 8D

YP=.67

▲ = UNDAMAGED

✳ = DAMAGED

Figure 61

CASE 8 and CASE 8D

YP=.73

△ = UNDAMAGED

✳ = DAMAGED

Figure 62

145

CASE 8 and CASE 8D

YP=.79

△ = UNDAMAGED

※ = DAMAGED

Figure 63

146
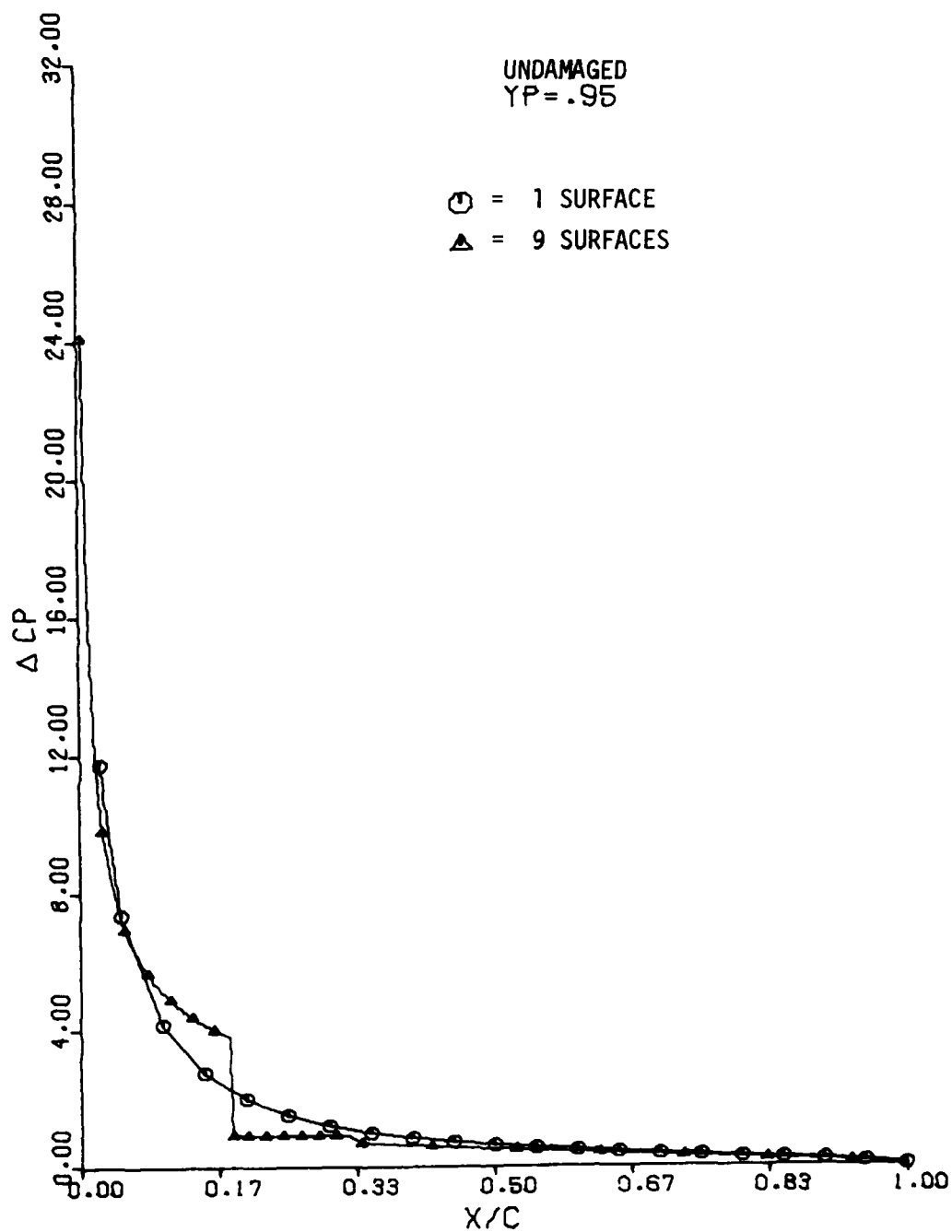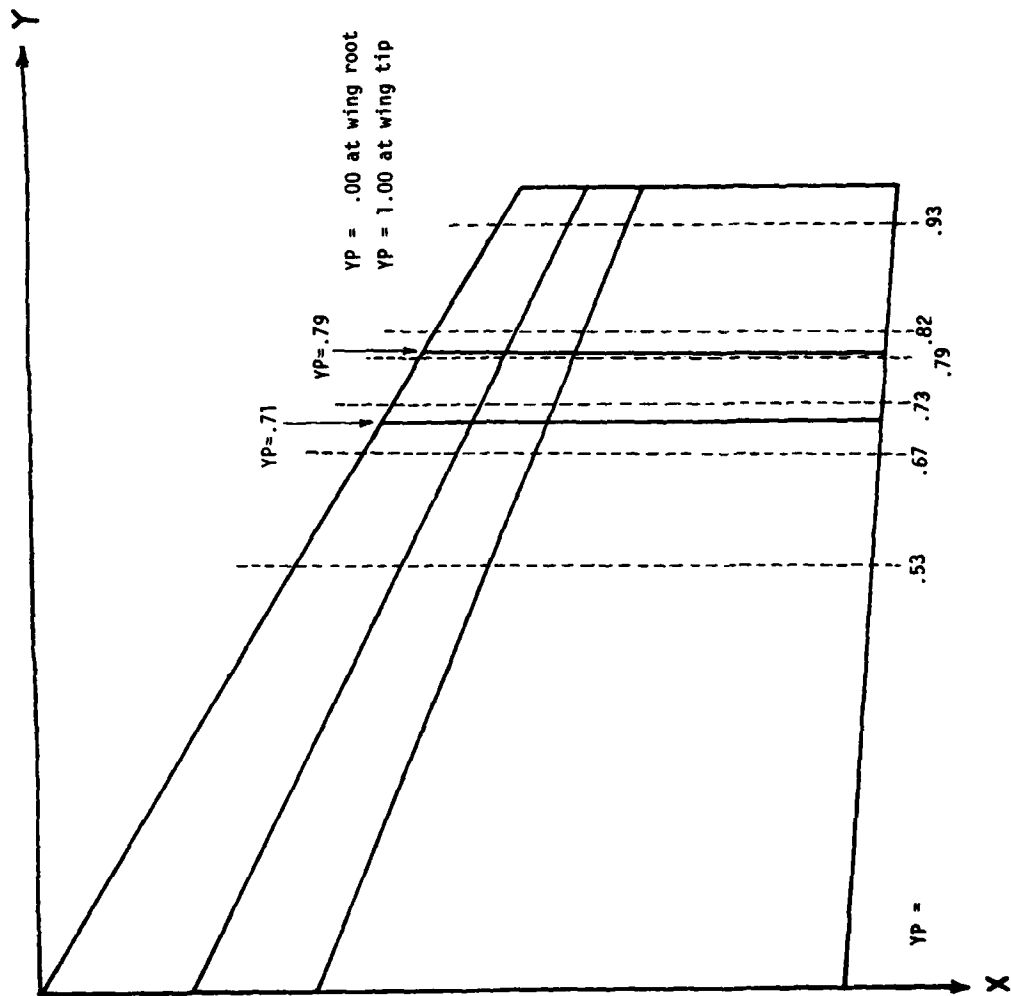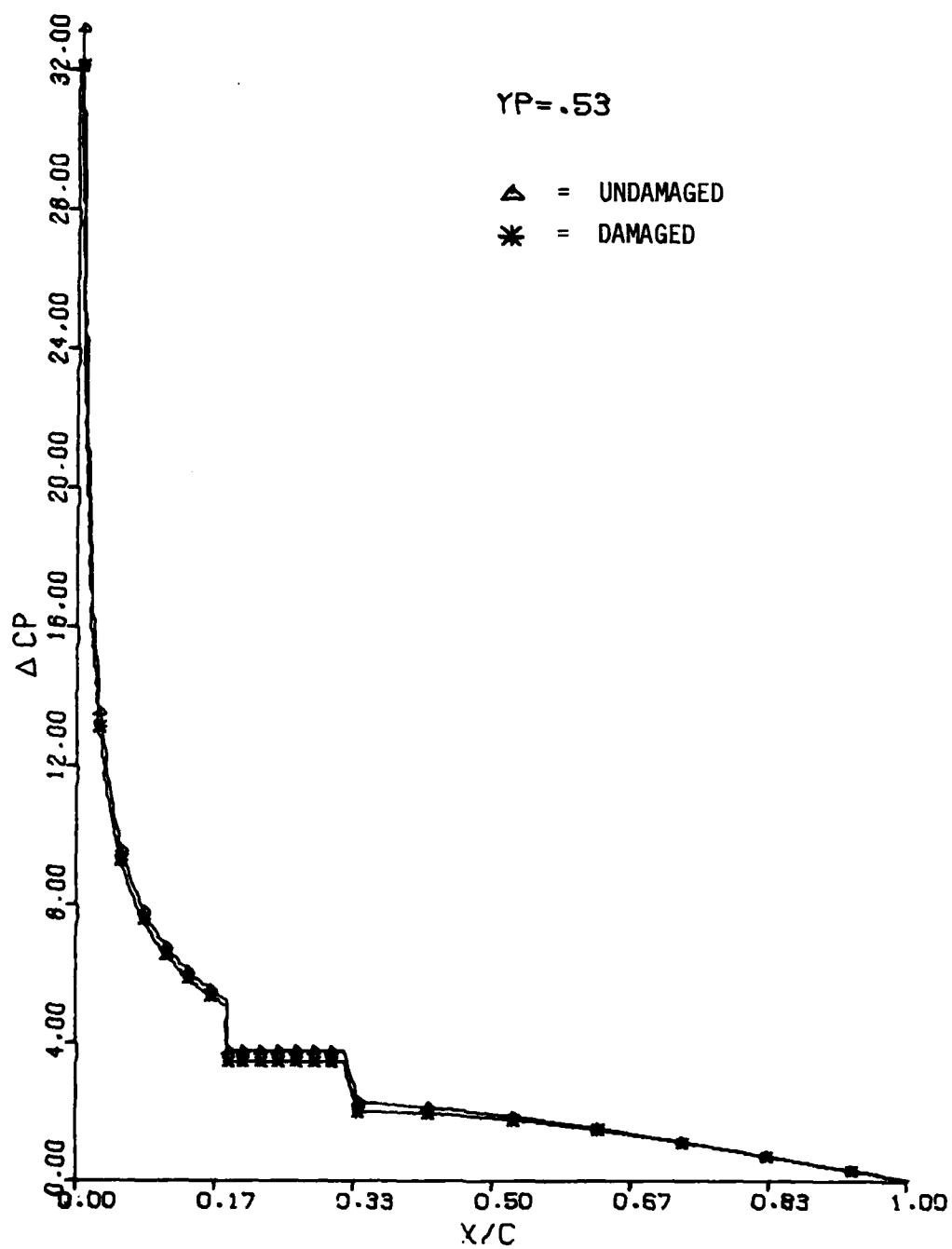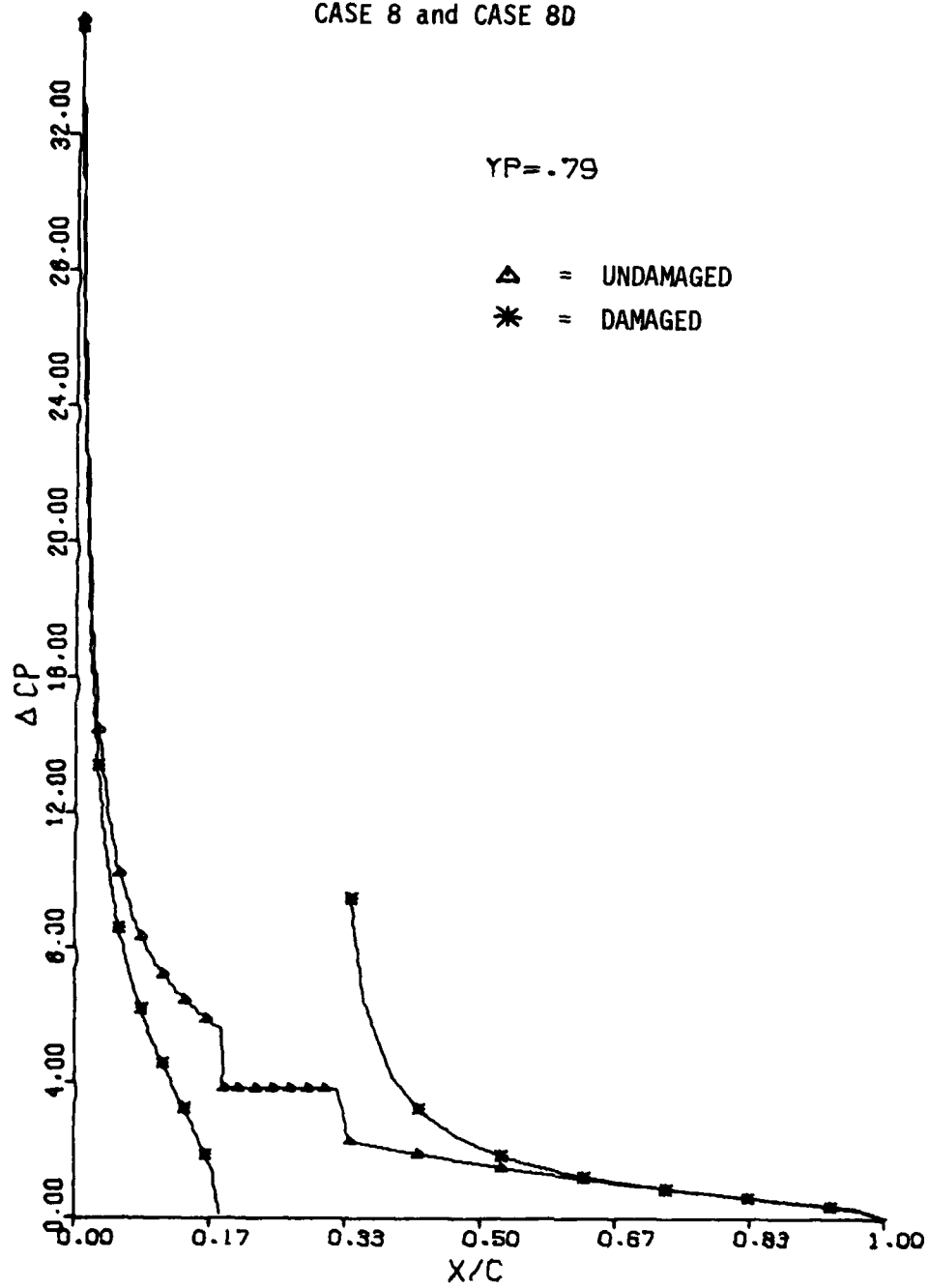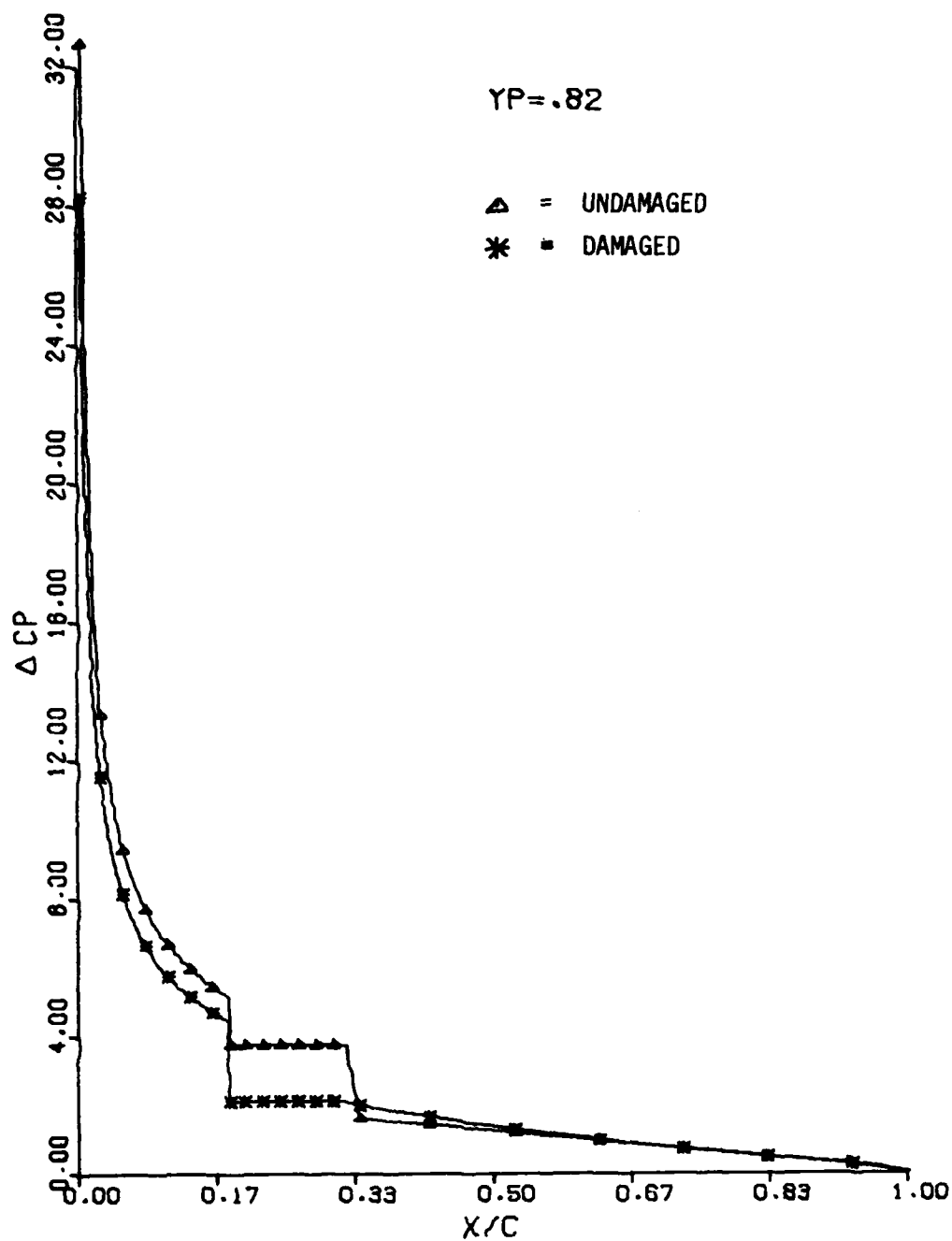
CASE 8 and CASE 8D

Figure 64

CASE 8 and CASE 8D

YP=.93

△ = UNDAMAGED
※ = DAMAGED

Figure 65

148

Figure 66

149

CASE 8
AND
CASE 8D

△ = UNDAMAGED, 9 SURFACES
✳ = DAMAGED, 8 SURFACES

CLC/CAVG

2Y/B

Figure 67

150

CASE F ⊙ = UNDAMAGED, 1 SURFACE
AND
CASE 8D ✳ = DAMAGED, 8 SURFACES

Figure 68

151
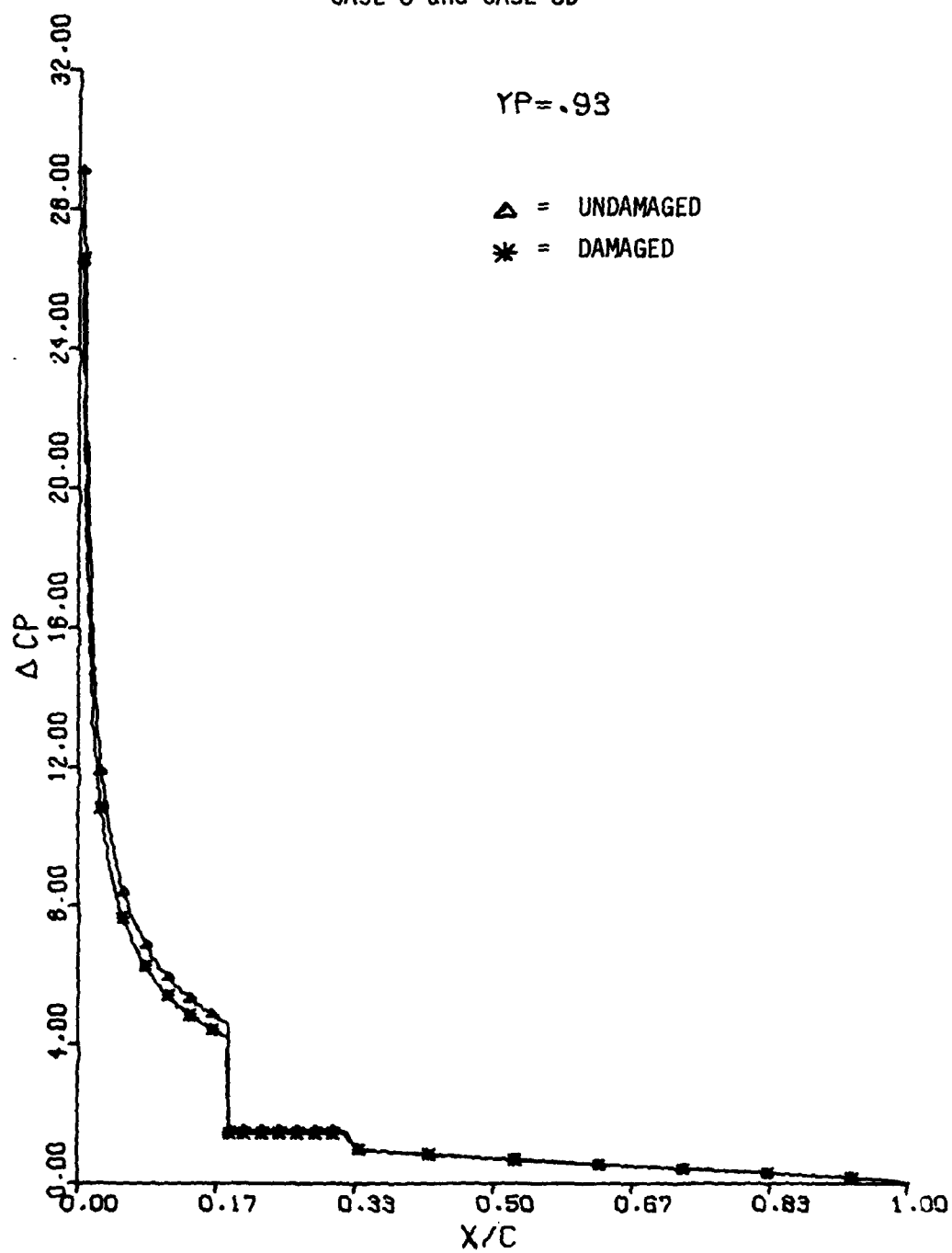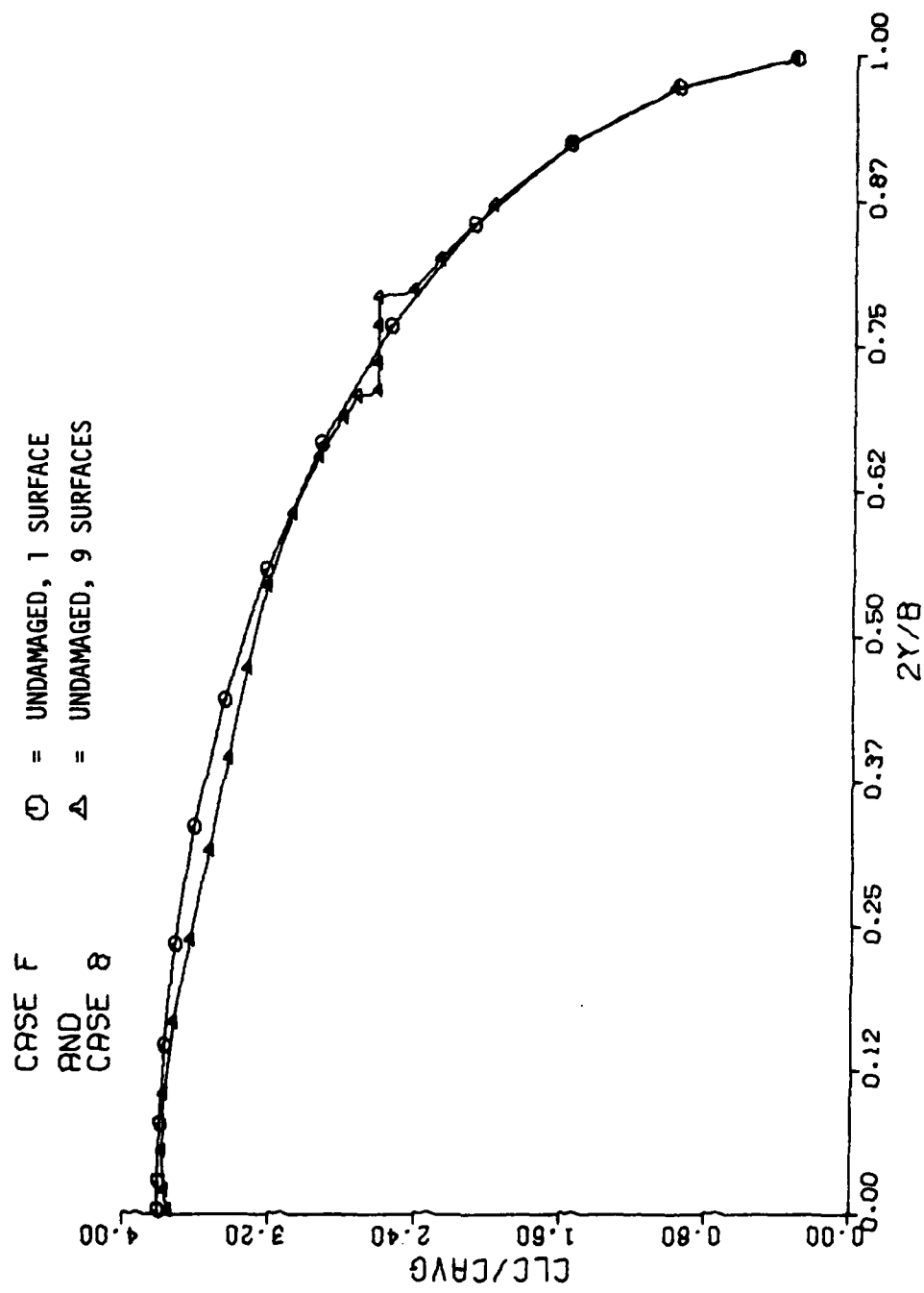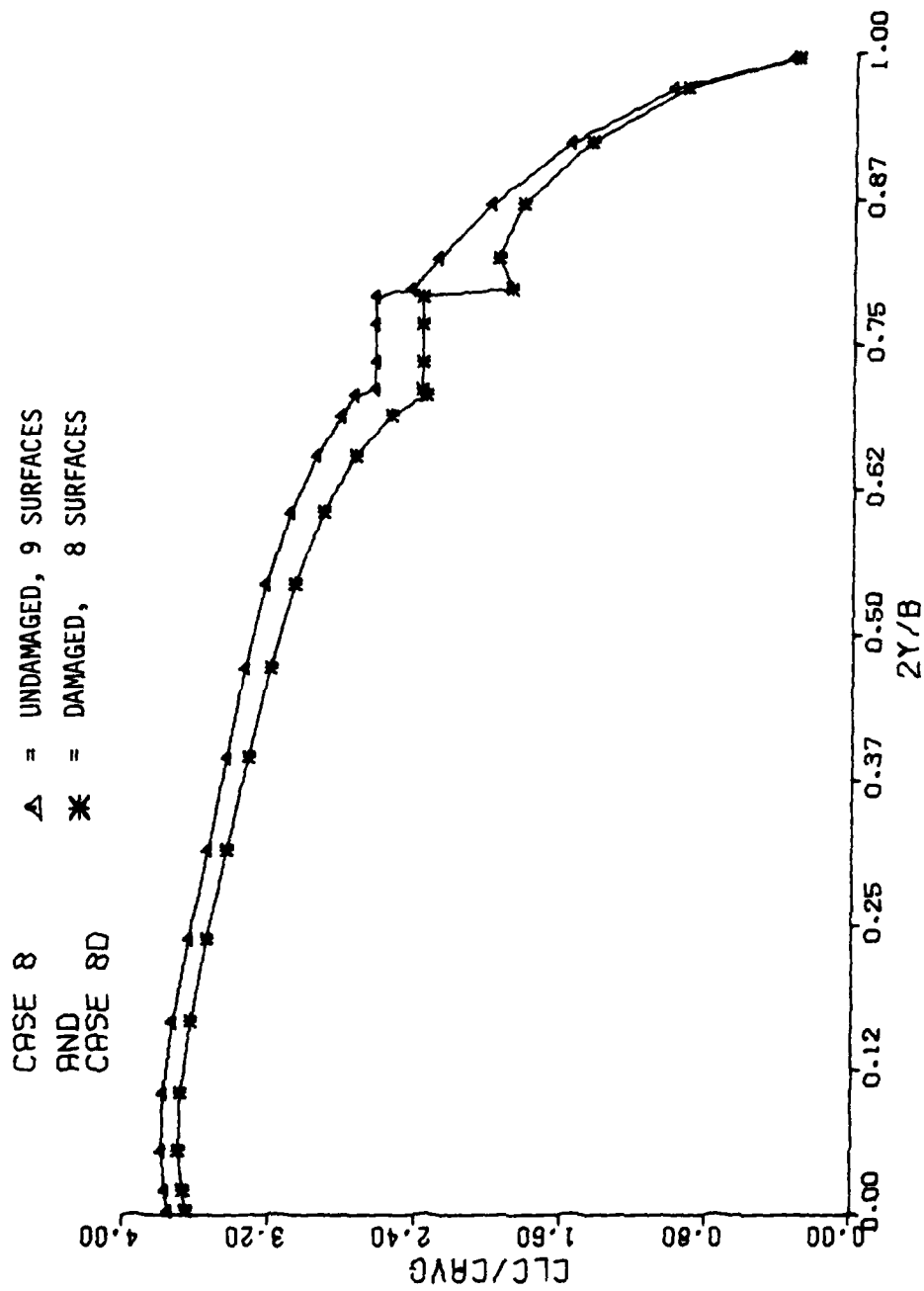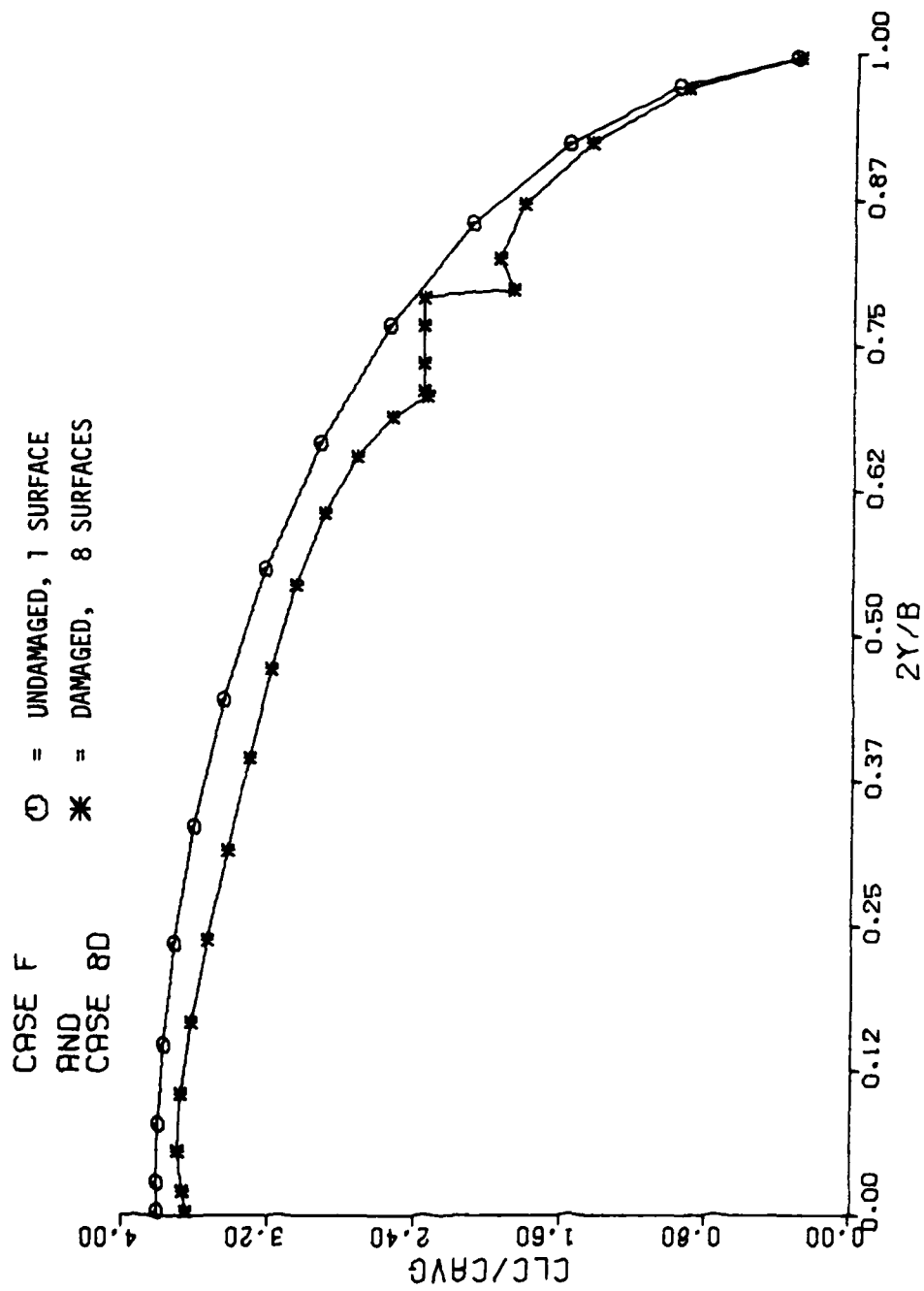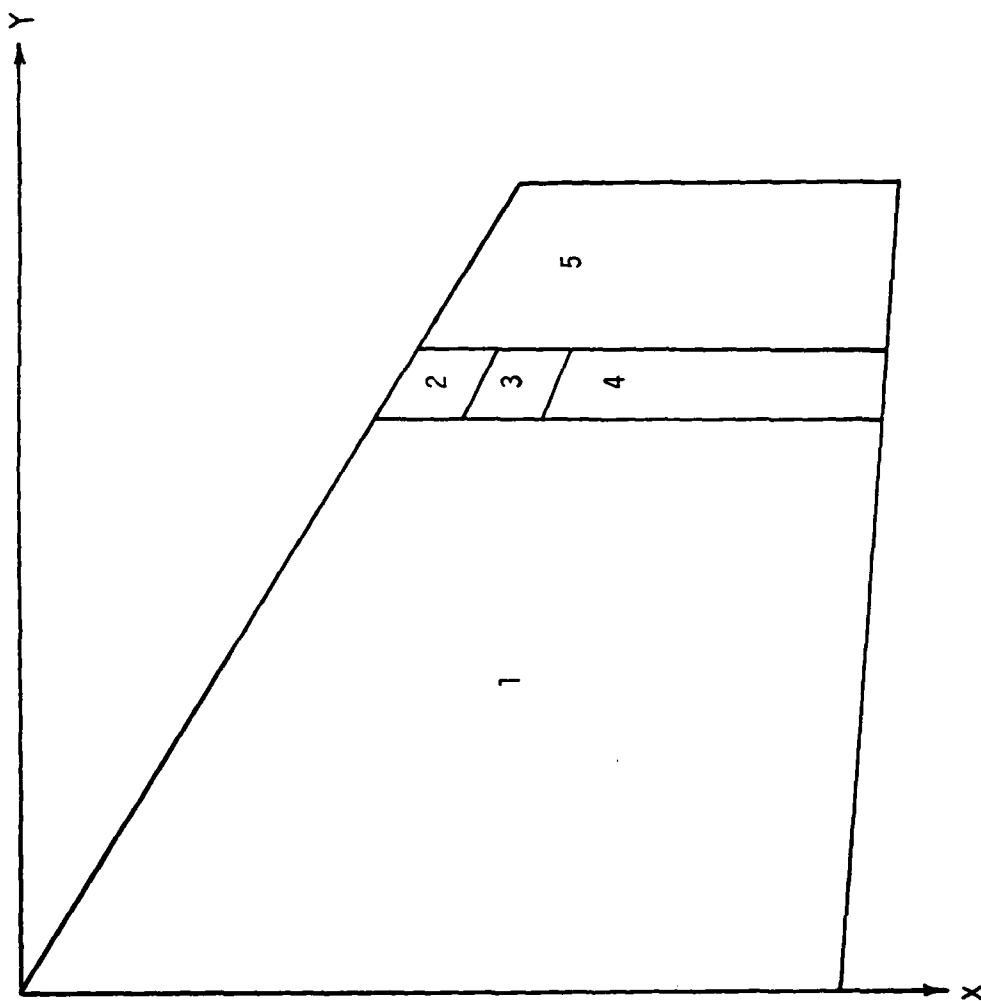
UNDAMAGED COARSE MODEL SURFACE NUMBERING

Figure 69

152
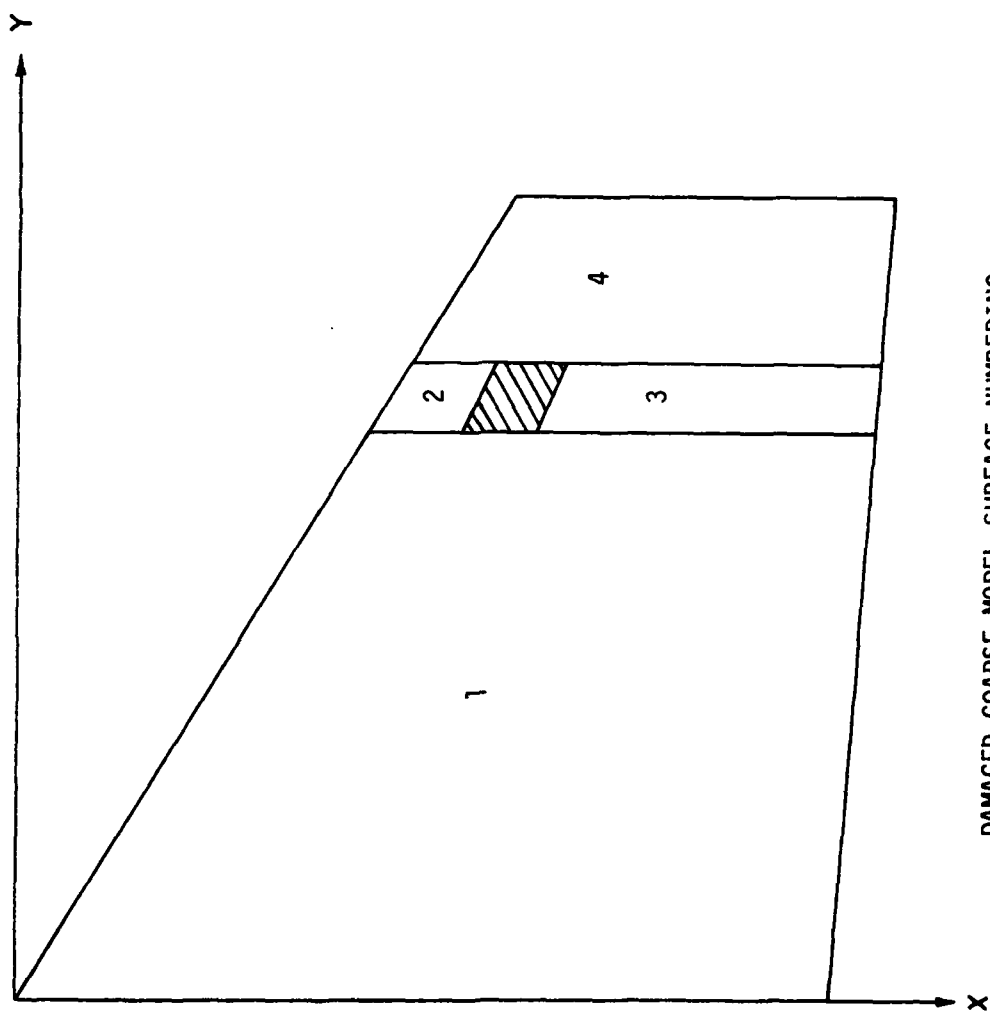
DAMAGED COARSE MODEL SURFACE NUMBERING

Figure 70

153
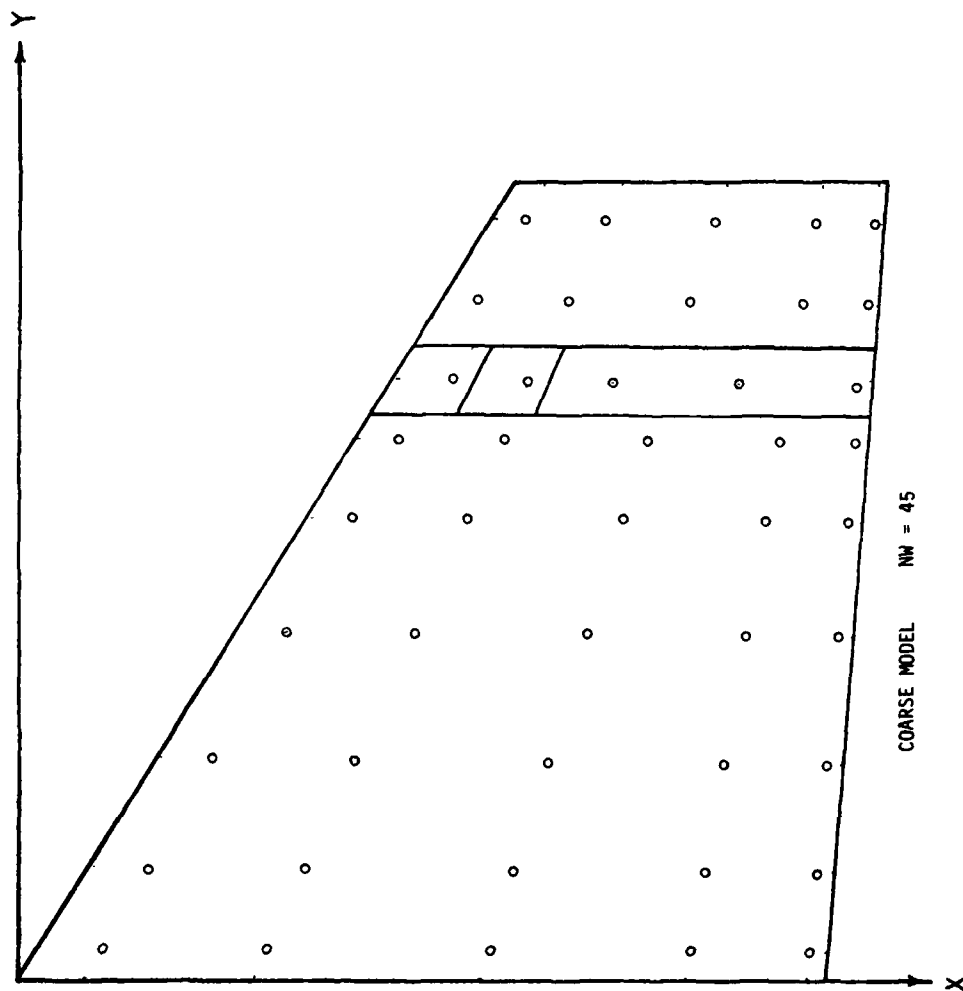
COARSE MODEL   NW = 45

COARSE MODEL CONTROL POINT LOCATIONS

Figure 71

154

COARSE MODEL

Figure 72

COARSE MODEL

YP=.65

$\times$ = UNDAMAGED, 5 SURFACES

$\times$ = DAMAGED, 4 SURFACES

Figure 73

156
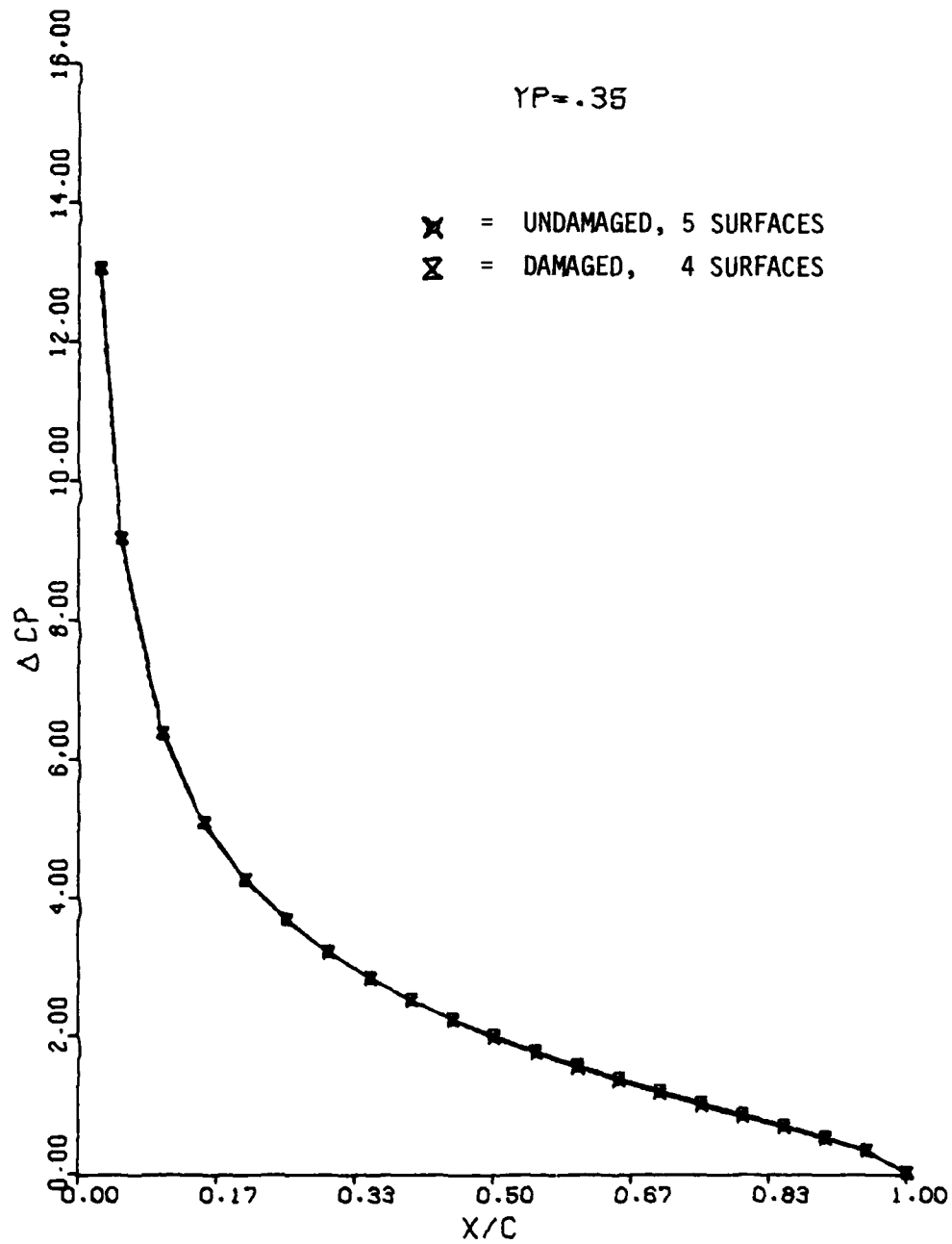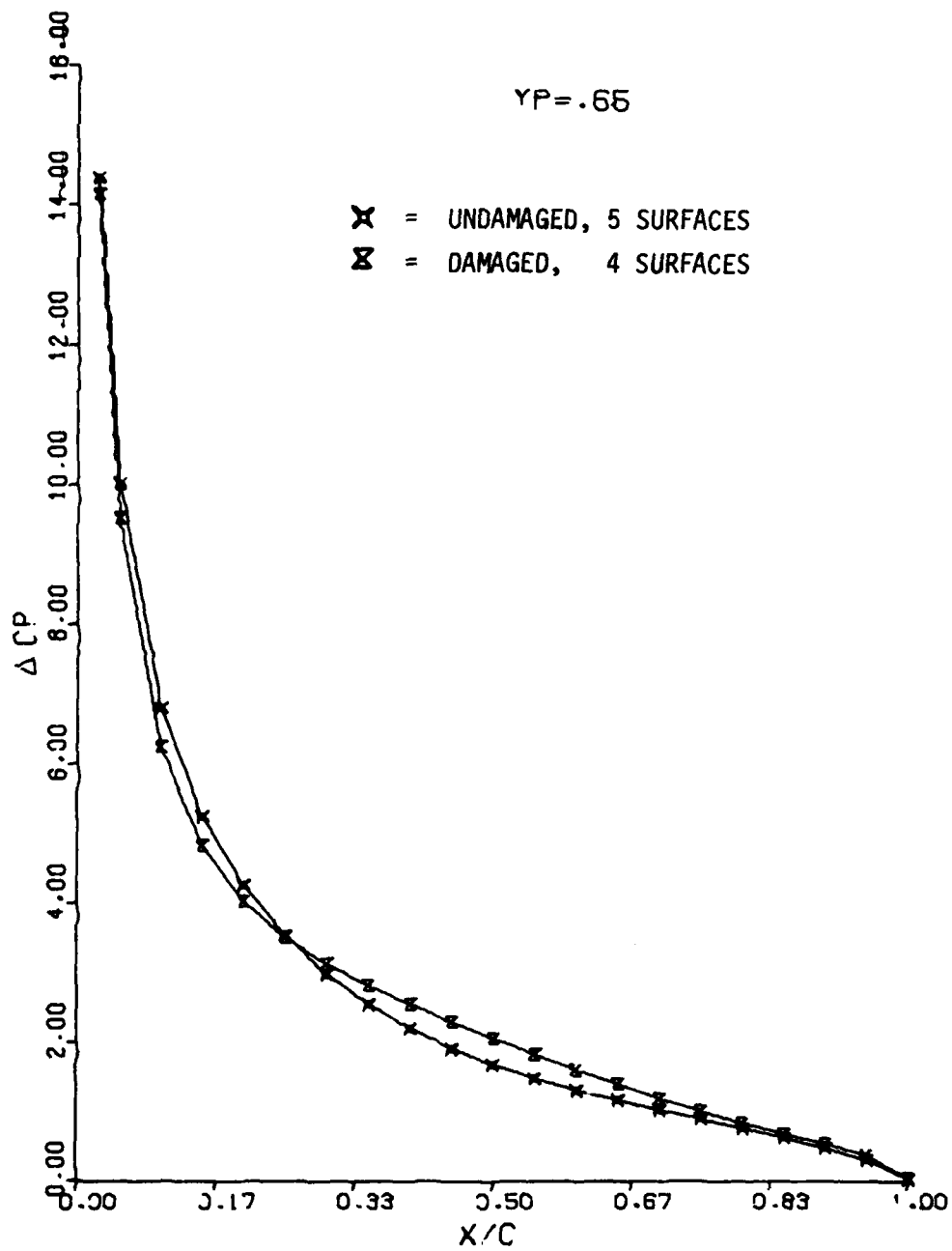
COARSE MODEL
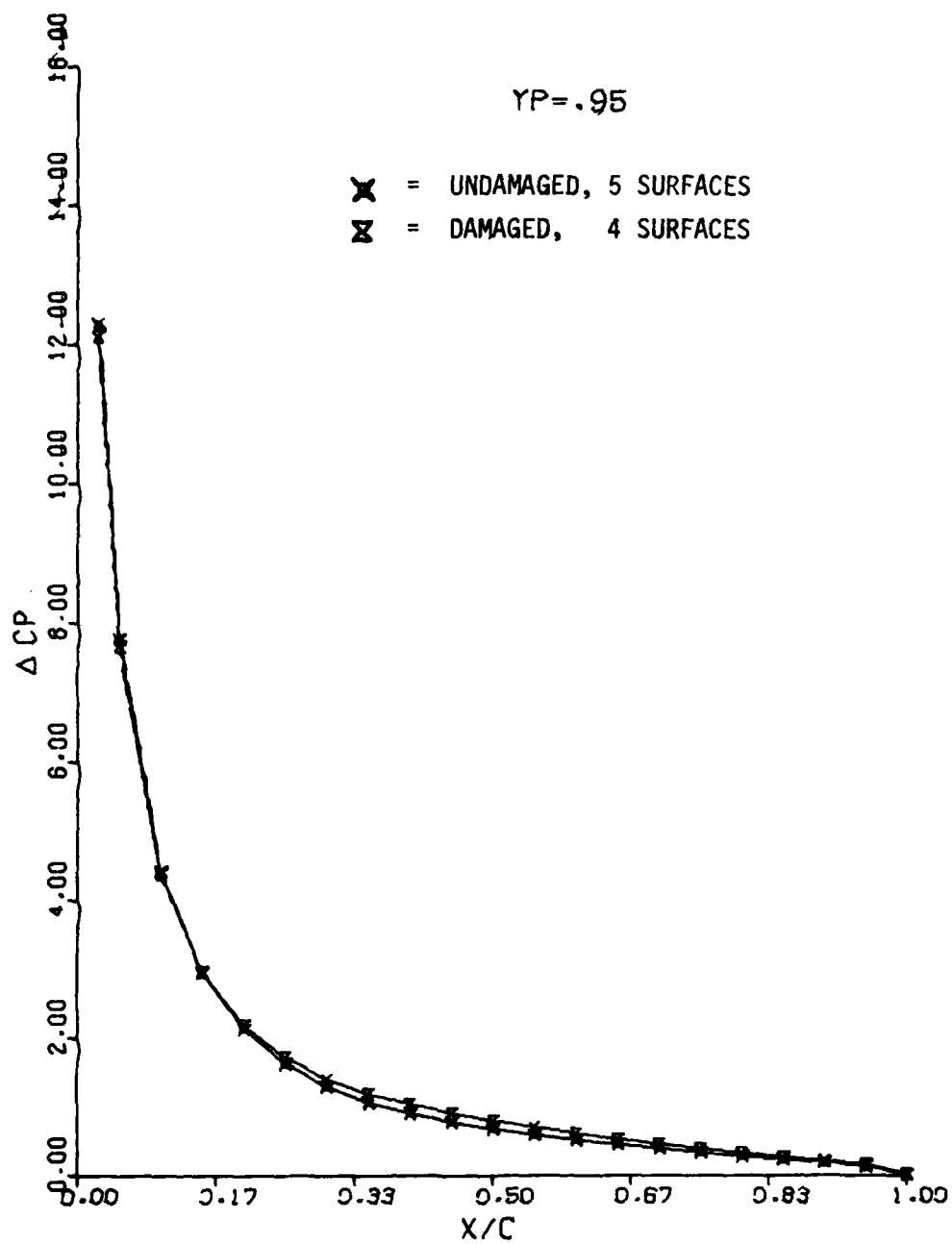
Figure 74
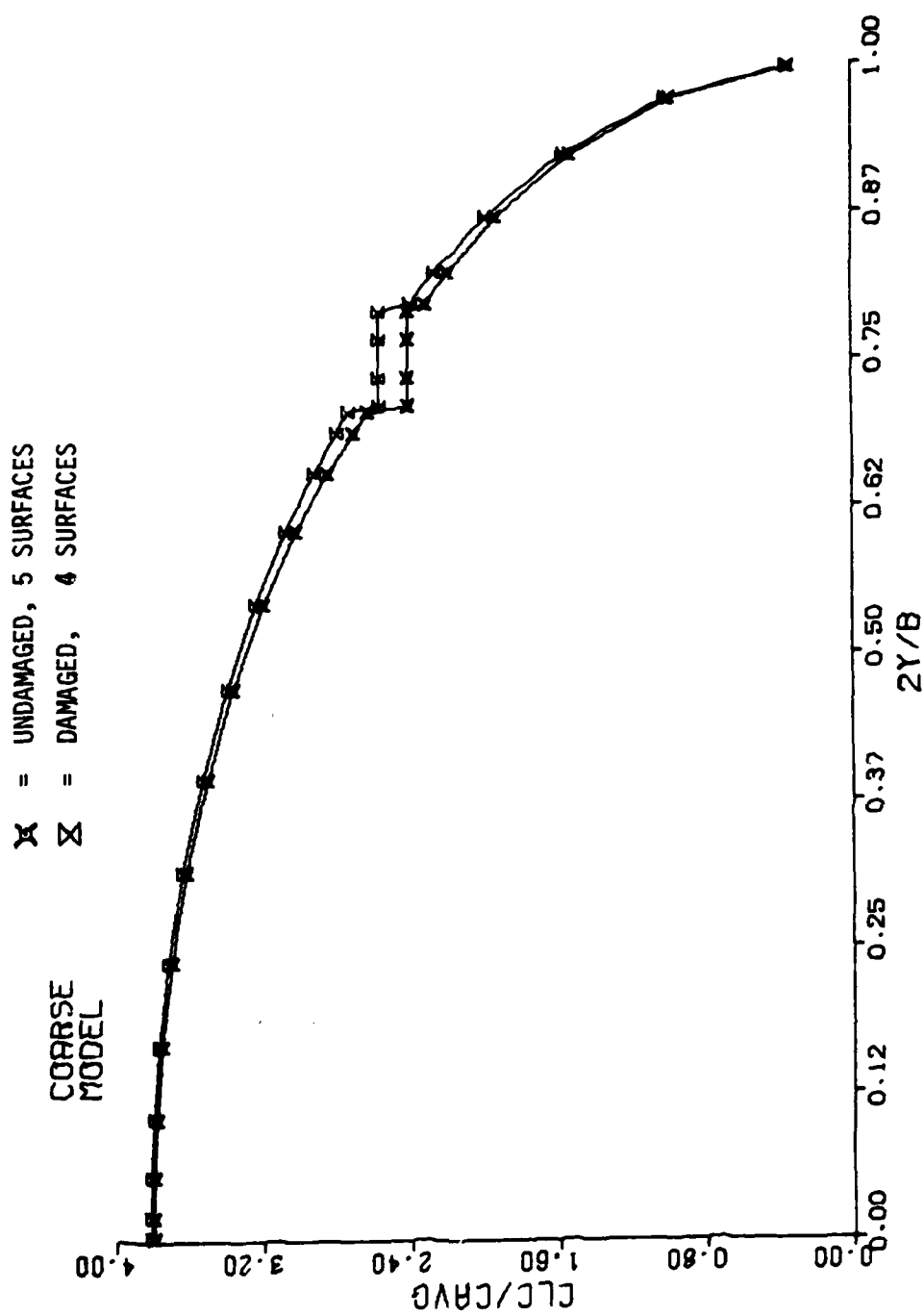
Figure 75.

158

Figure 76
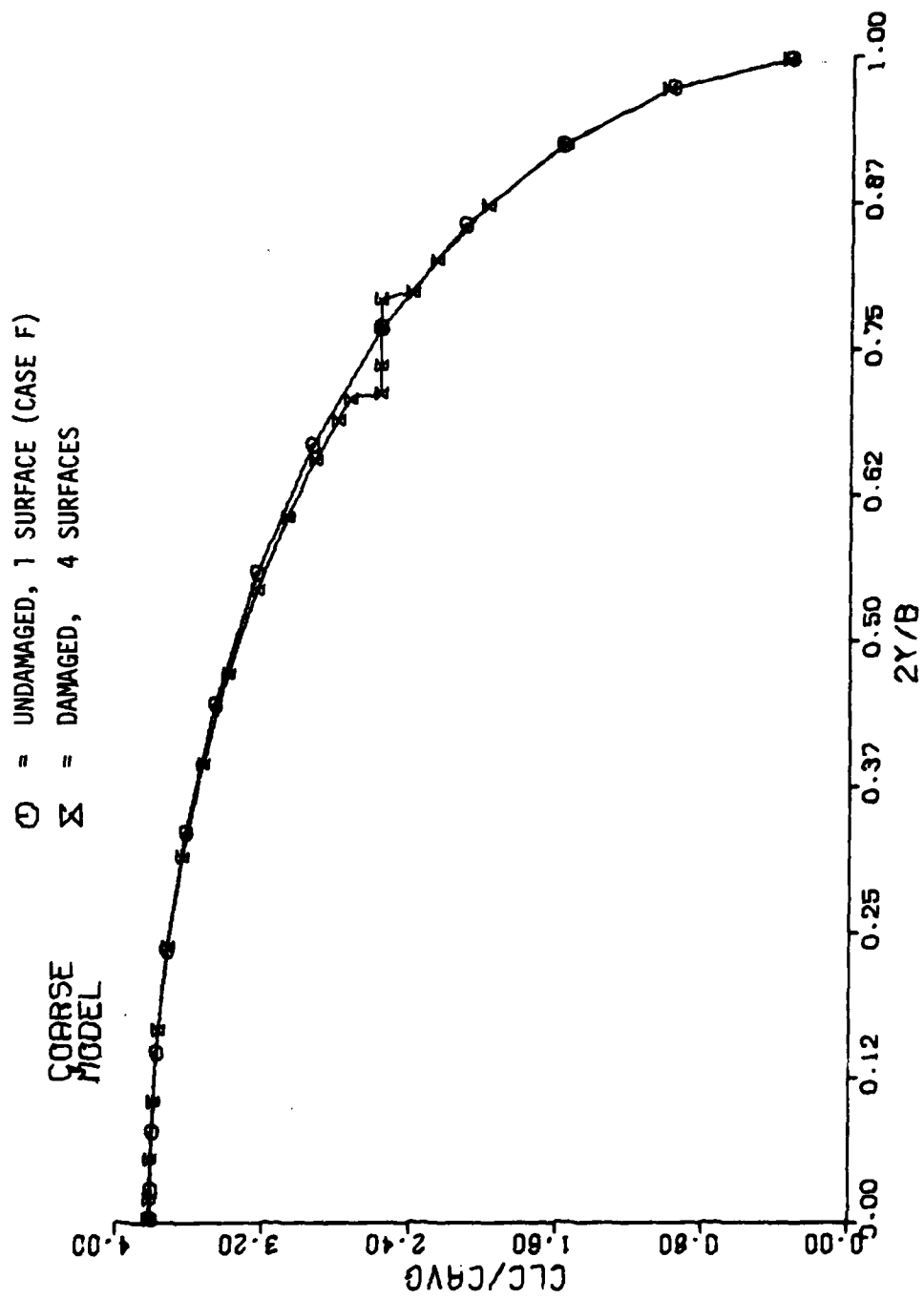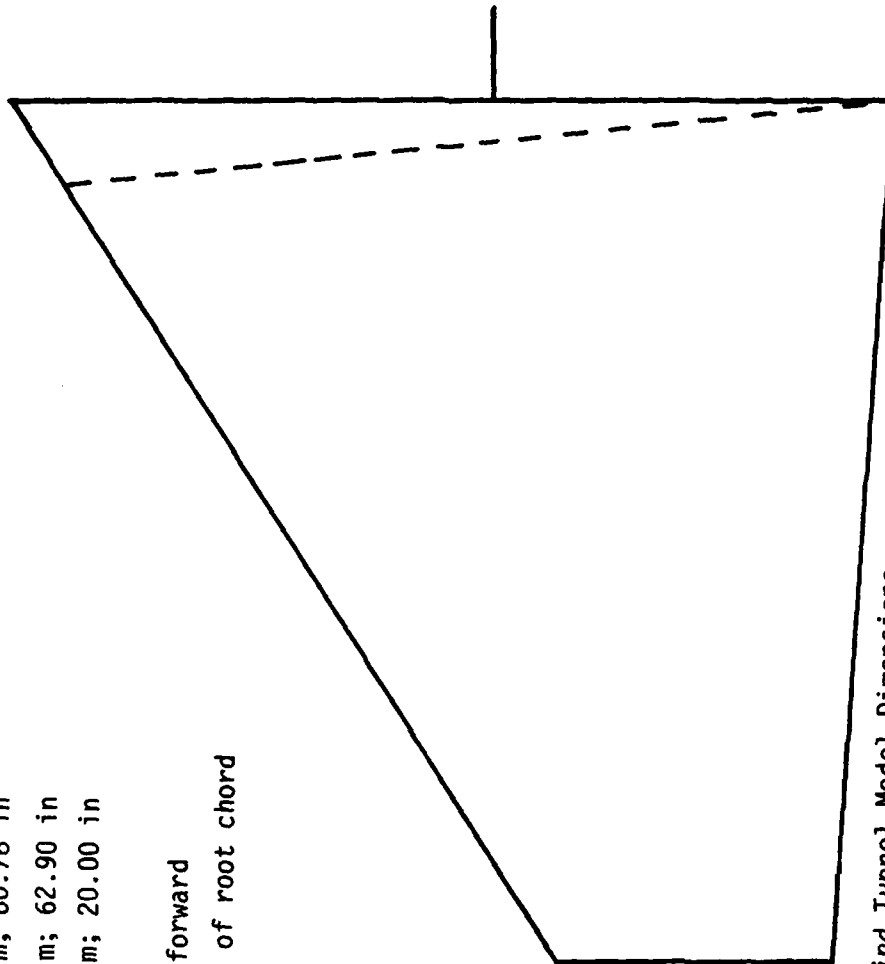
159

Figure 77
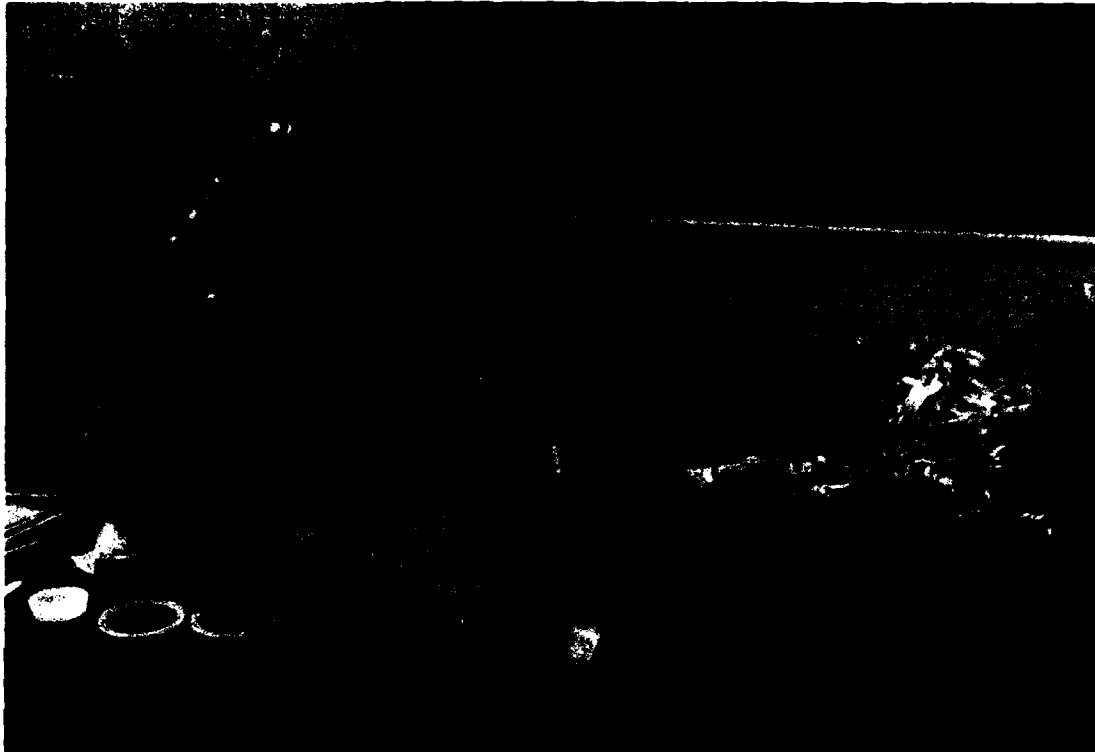
160
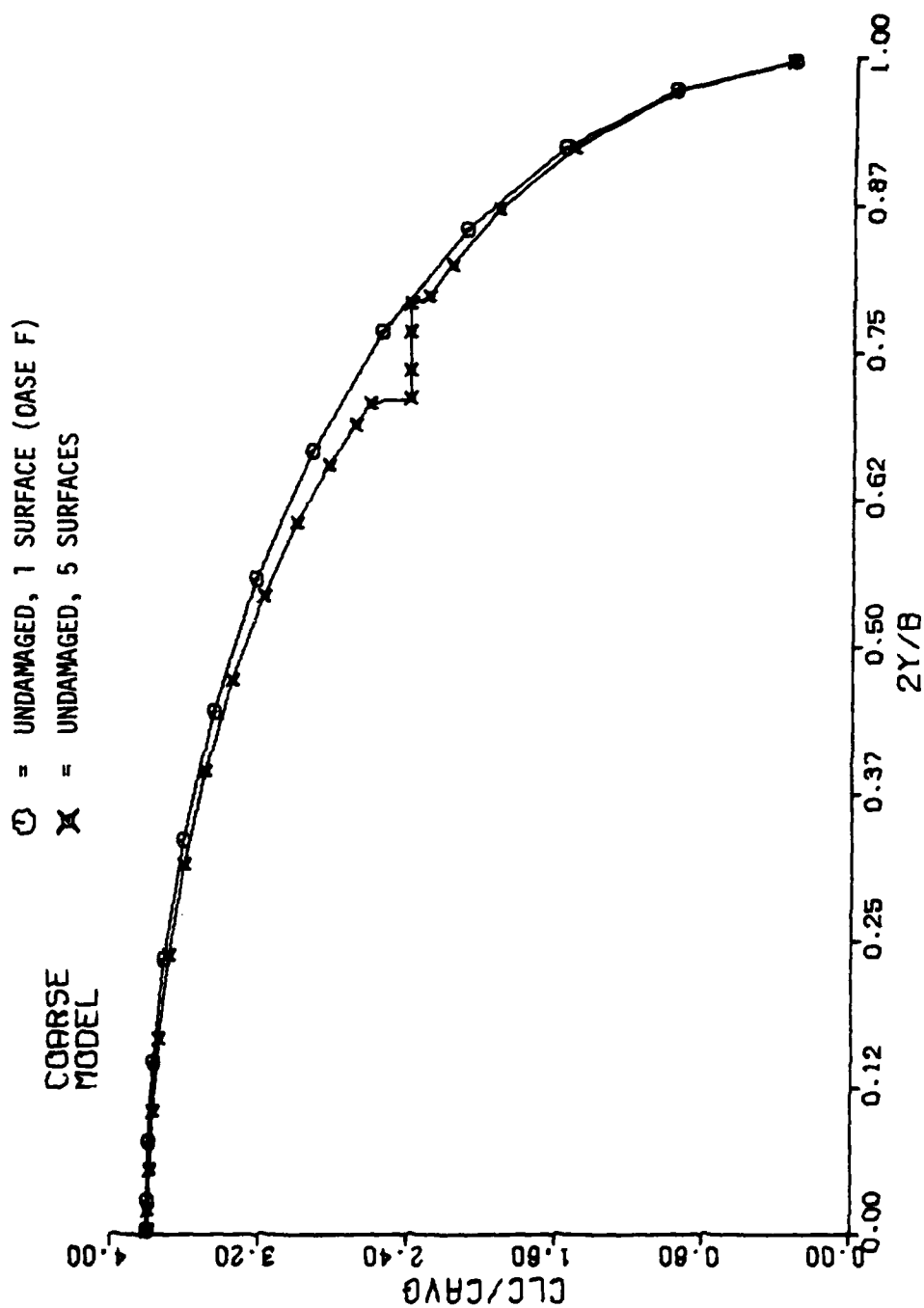
Airfoil section   - 65A004
Planform area   - 1.626 sq m; 17.50 sq ft
Semispan   - 1.544 m; 60.78 in
Root chord   - 1.589 m; 62.90 in
Tip chord   - .508 m; 20.00 in
Leading edge sweep   - 32.7°
Trailing edge sweep   - 3.61° forward
Hinge line   - 54.34% of root chord
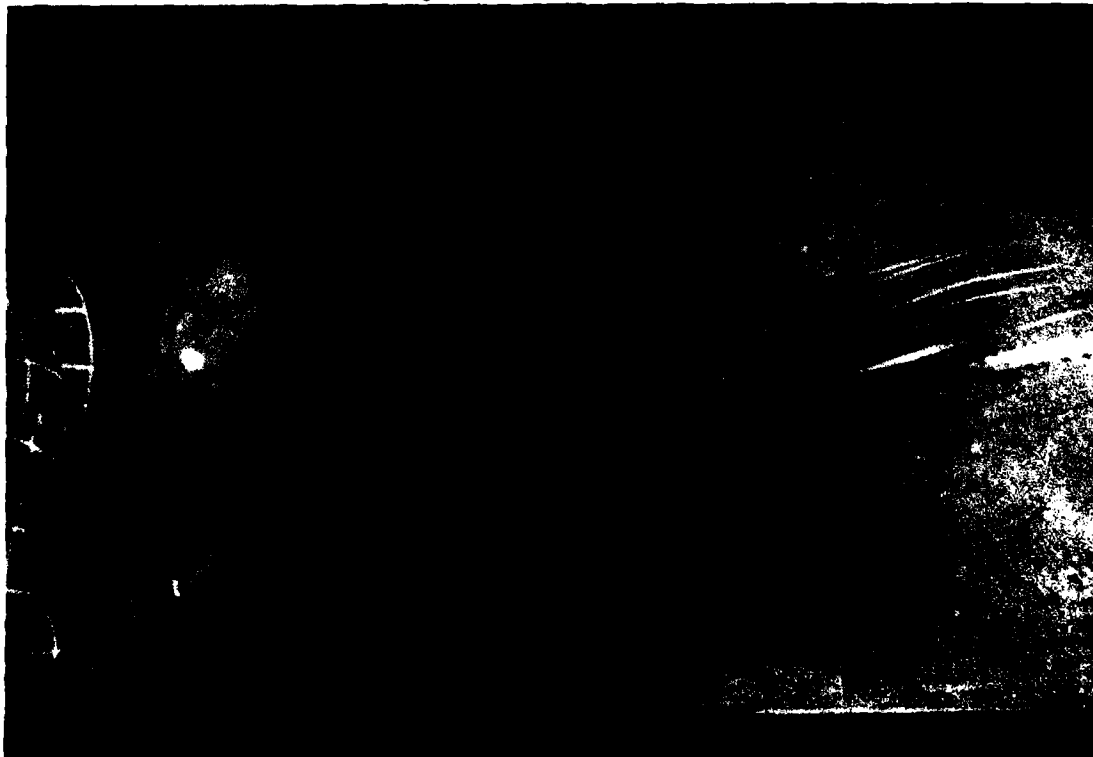Dihedral   - -4.00°

Wind Tunnel Model Dimensions
(Modified T-38 Stabilizer)

Figure 78

161

INSTALLATION OF PRESSURE TUBES IN STABILIZER

Figure 79
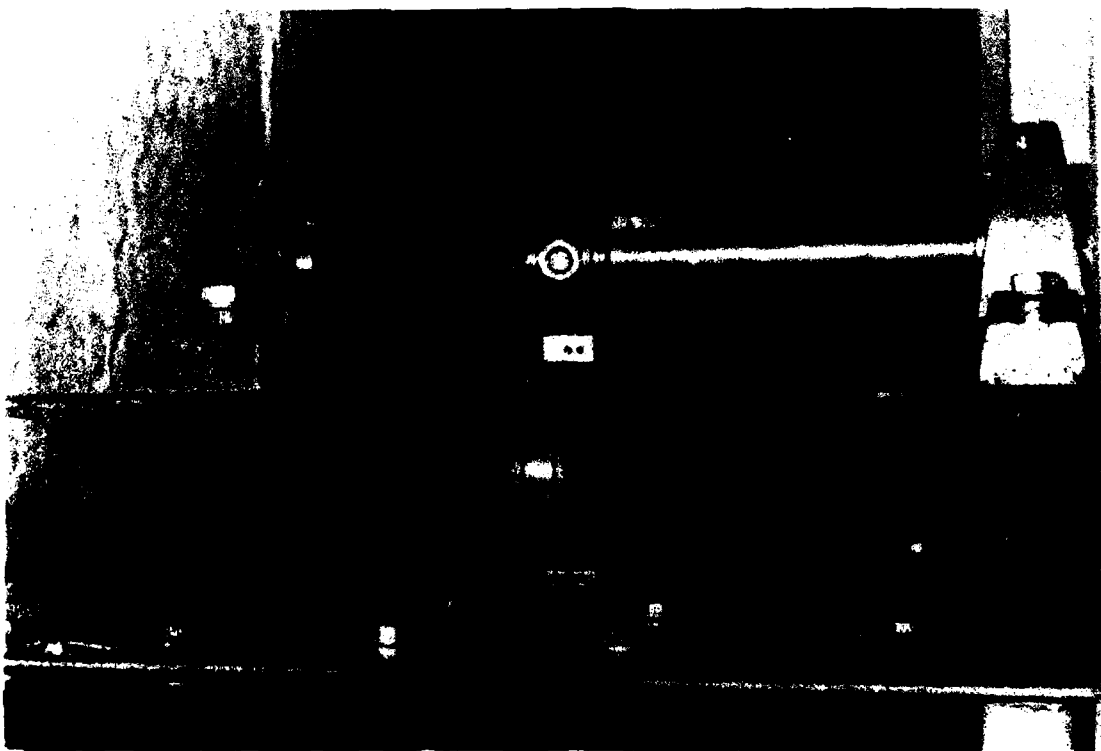
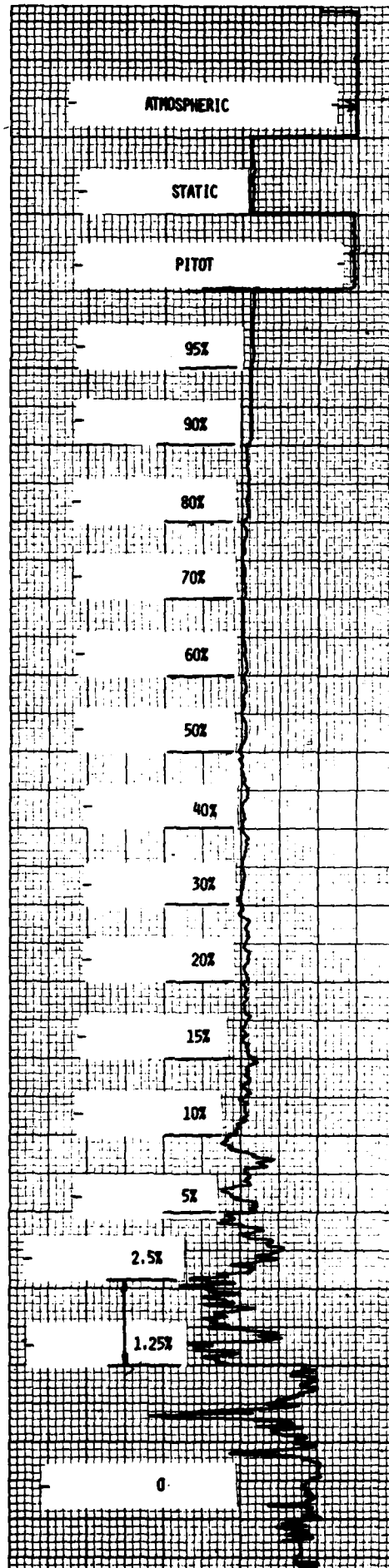STRAIN GAGE AND PRESSURE TUBE ADAPTER DETAILS

Figure 80

INSTALLED STABILIZER (ABOVE) AND MOUND (BELOW)

Figure 81

PRESSURE TRACE AT 67% SEMISPAN, M = .12,

ZERO ANGLE OF ATTACK

Figure 82

164 A

APPENDIX

ESTIMATE OF DRAG INCREMENTS DUE TO DAMAGE

A.1 Introduction

As mentioned in Section 2.2.2, the current state of the art for estimating damage induced drag levels leaves much to be desired. Before a literature survey is made, in order to gain an estimate of the drag rise due to aerodynamic damage, the methods of data reduction are specified. For the estimation of the influence of aerodynamic damage on the performance, the drag rise should be evaluated on the basis of constant lift in order to simulate the lift required to maintain desired flight conditions. This basis may cause an over-estimate in the present study of aeroelastic failure. Here, possible reduction in lift should also be considered in the analysis, by estimating the drag rise on the basis of fixed angle of attack. Actual damage will generally require aileron deflection to overcome possible asymmetries in the rolling moments generated by the two halves of the wing. This asymmetry depends on the loss in lift due to the aerodynamic damage and its location. A drag increment based on fixed angle of attack takes into account the loss in lift and is believed to be a low bound since it does not include the lift associated with the aileron deflection. The two estimates for ΔC_D due to damage are shown schematically in Figure A.1. It is believed that the actual case lies between estimates based on fixed lift coefficient and fixed angle of attack. A better estimate cannot be

made at the present stage of the study, since the required aerodynamic data is lacking.

A.2 Estimate of Drag Increment Due to Aerodynamic Damage

The first systematic experimental investigation of the aerodynamic characteristics of damaged wings is a Cornell Aeronautical Laboratory report 22/ dated 1952. The test model was a 24" chord wing, with NACA 65_1012 airfoil, that spanned the 102" height of the test section. The wing was tested at Mach numbers 0.3, 0.7 and 0.85 with various simulated damage configurations that are shown in Figure A.2 which is Table I of Reference 22.

The test results were processed in a later report by the same laboratory 11/ by fitting a parabolic drag model to the data. Using the notation of this reference:

$$C_D = C_{D_\pi} + pC_L^2 ,$$

changes of C_D caused by damage are recorded as changes of the "parasitic" drag coefficient, C_{D_π}, and the slope $p = dC_D/dC_L^2$. The results were normalized to the damage hole area, instead of wing area by introducing

$$C_D^* = \frac{\Delta D}{qA}$$

$$= C_{D_\pi}^* + p^* C_L^2$$

Figure A.3, which is Table II of Reference 11, is a summary of drag

166

increases due to damage holes of various configurations. This data is
the basis for the estimations made in Section 2.2.2.

Before we proceed and discuss the results of this investigation
it is important to make notes on some special features of the test condi-
tions. First, the basic wing is two-dimensional, thus the slope p^* in
the expression for C_D^* should not be interpreted as induced drag in the
sense of a finite wing. Secondly, the airfoil had a thickness ratio of
12% which was typical of aircraft of the time of the study. This value
is much higher than the thickness ratios of 6% or less used on most con-
temporary fighters. This difference is of importance since transonic
phenomena are much more violent for the thick airfoil. For example, it
shows a dip in the lift curve slope at a Mach number about 0.85, an
early drag divergence and steeper drag rise 23/ . The Mach number 0.85
tests were executed only over a very narrow range of angles of attack,
namely over very small values of lift coefficients. Therefore, the
slope term, p^*, was not evaluated for this Mach number. The discussion
below will, therefore, be limited to M = 0.7. The investigation in-
cluded several configurations with edges of the holes raised to form a
"scoop" or a "spoiler" lip. The height of the lips were 1/2" and 1",
or about 2% and 4% of the local chord. Naturally, such protuberances
generate a considerable drag. However, according to information received,
actual petals on battle damaged wings of high performance fighters do
not exceed 1" which is only a fraction of 1% or full size typical chord.
Some care should, therefore, be utilized when applying damage cases

167

E & F of Figure A.2.

The damage configurations that gave the highest drag rise are 1A15-2A15 and 1A10-2A10. Recall from Figure A.2 that hole locations 1 and 2 are at the leading edge and at quarter cord upper surface. It is believed that the combination of a leading edge hole which acts as an inlet, a hollow wing that serves as a settling chamber and a hole located in the region of maximum suction generate a fountain which acts on the external flow as a spoiler that causes separation and the associated drag rise. For example, for damage configuration 1A15-2A15 we find A/S = 0.00415 and

$$C_{D_\pi}^* = 2.4 , \qquad p^* = 10.0$$

which give for a fixed C_L = 0.8 a drag rise of C_D^* = 8.8 or its equivalent ΔC_D = 0.036. The alternative estimate, namely the one based on fixed angle of attack, predicts increase in drag coefficient is 0.017 which is less than half the value predicted for constant C_L.

A through hole is represented by damage configuration 2A15-4A15 whose two holes are centered at quarter chord. For this configuration

$$C_{D_\pi}^* = 0 \qquad p^* = 6$$

For C_L = 0.8 the predicted increase in drag coefficient is C_D^* = 3.84 or ΔC_D = 0.016. For the case of constant angle of attack we find for the damaged wing at α = 4.6°, C_L = 0.64 and C_D = 0.028, i.e. an increase of ΔC_D = 0.006 which again is less than half the value

predicted for fixed C_L.

To conclude the analysis of References 22 and 11 we summarize findings for $C_L = 0.8$ (undamaged) and $M = 0.7$.

CONFIGURATION	REPRESENTING	C_D^*		ΔC_D	
		fixed C_L	fixed α	fixed C_L	fixed α
1A15-2A15	Leading edge inlet forms a fountain	8.8	4.1	.036	.017
2A15-4A15	Through hole at quarter chord	3.8	1.5	.016	.006

However, we recall that these values are not necessarily valid in transonic speeds, that they do not include the expected large change in induced drag which results from the modification in lift distribution and that they do not include the additional effects associated with aileron deflection that should follow any non-symmetrical damage.

A.3 Full Scale Test of the A-4B

A more recent publication 24/ is a full-scale low speed wind tunnel study of the aerodynamic characteristics of an A-4B aircraft with damage to one wing. Based on this technical memorandum an estimate of the increase in total drag coefficient was made for two cases.

In the first case a comparison of the lift and drag coefficient is made of the aircraft with slats closed and open. This is an

estimate for damage resulting in a loss of the two slats. As explained before, the evaluation is made on the basis of fixed angle of attack and fixed lift coefficients as lower and upper bounds.

CONFIGURATION	α	14°	16°	18°
slats open	C_L	0.77	0.87	0.97
	C_D	0.102	0.127	0.165
slats closed (same α)	C_L	0.76	0.86	0.90
	C_D	0.100	0.142	0.180
(closed-open) (same α)	ΔC_L	-0.01	-0.01	-0.07
	ΔC_D	-0.002	0.015	0.015
slats closed same C_L	C_L	0.77	0.87	above $C_{L_{max}}$
	C_D	0.103	0.150	N/A
(closed-open) same C_L	ΔC_D	0.001	0.023	N/A

In the case of the smaller angle of attack the changes in the aerodynamic coefficients are small. In all cases the lower bound predicts a small reduction in C_D. On the other hand, the upper bound predicts a very large increase in C_D due to a complete loss of the slats at very high angles of attack. If damage occurs at $\alpha = 16°$, $\Delta C_D = 0.023$ which is higher than C_{D_o}. At higher angles of attack, $C_{L_{max}}$ is exceeded and the increase in C_D is expected to be much higher.

The largest hole configuration tested is #8 which is shown in

Figure A.4. The through hole area is about 4% of the total exposed wing area and its center is about 60% of the exposed semispan and at the middle of the local cord. Evaluation of changes in the aerodynamic characteristics is done for open slats, since this represents high lift configuration, based on Figure 68a of Reference 24 which is shown in the present report as Figure A.5.

CONFIGURATION	α	14°	16°	18°
undamaged	C_L	0.76	0.87	0.97
	C_D	0.102	0.129	0.167
damage #8 (same α)	C_L	0.71	0.81	0.91
	C_D	0.104	0.135	0.165
(damaged-undamaged) same α	ΔC_L	-0.05	-0.06	-0.06
	ΔC_D	0.002	0.004	0.002
· · · · · · · · · ·	· · · ·	· · ·	· · ·	· · ·
damage #8 same C_L	C_D	0.120	0.153	0.200
(damaged-undamaged) same C_L	ΔC_D	0.008	0.024	0.033

The lower bound predicts only very small changes in C_D while the upper bound predicts changes in excess of C_{D_0} at very large angles of attack.

171

A.4 Effect of Wing Strake

Two recent light weight fighters feature a wing-strake configuration as an aerodynamic device for increasing maximum lift and improving lift/drag ratio at high lift coefficients. Reference 25 contains longitudinal aerodynamic characteristics of such configuration, which is shown as Figure A.6, and will therefore be used to estimate the possible increase in drag coefficient associated with a major damage to the strake. Such a damage can greatly modify the strength and loca- tion of the vortex generated by the strake, thus altering its inter- action with the main wing. The present estimate is based on comparing strake-on with a strake-off configuration. The tables below are valid for M = 0.7, which is the highest Mach number reported in the reference and for a moderately cambered wing (see also Figure A.7).

CONFIGURATION	α	14°	16°	18°
strakes on	C_L	0.96	1.06	1.16
	C_D	0.22	0.28	0.34
strakes off same α	C_L	0.86	0.90	0.94
	C_D	0.180	0.22	0.26
(off-on) same α	ΔC_L	-0.10	-0.16	-0.22
	ΔC_D	-0.040	-0.06	-0.08
. . . .
strakes off same C_L	C_L	0.96	above $C_{L_{max}}$	above $C_{L_{max}}$
	C_D	0.34	N/A	N/A
(off-on) same C_L	ΔC_D	0.12	N/A	N/A

172

Again, the lower bound predicts a slight reduction in C_D, which is clearly associated with the reduction in C_L. The upper bound, however, is alarming since it predicts a very large increase in drag due to loss of a strake.

A.5 Effect of Leading Edge Flap

Another high lift device which is currently used, together with strakes, is the leading flap. In Reference 26 we find the longitudinal characteristics of a configuration similar to the one mentioned in Section A.4, except that it had a variable leading edge flap, as seen in Figure A.8. From Figure A.9, which is Figure 7 of the reference, the drag rise associated with the complete loss of the flap was estimated for $M = 0.8$.

CONFIGURATION	α	14°	16°	18°
flaps at 16°	C_L	0.76	0.83	0.89
	C_D	0.134	0.168	0.228
flaps at 0° same α	C_L	0.71	0.77	0.80
	C_D	0.184	0.226	0.260
flaps (deflected-undeflected), same α	ΔC_L	-0.05	-0.06	-0.09
	ΔC_D	0.05	0.058	0.042
flaps at 0° same C_L	C_D	0.220	over $C_{L_{max}}$	
flaps (deflected-undeflected), same C_L	ΔC_D	0.086	N/A	N/A

We use the differences between deflected and undeflected flaps to estimate boundaries for the possible change in the aerodynamic characteristics by elimination of a flap. Here the lower bound predicts drag rise in excess of twice the parasitic drag. The upper bound is again alarming since it predicts a 67% increase in C_D at $\alpha = 14°$, and post stall behavior at larger angles of attack, which may result in even higher values of C_D. If we add to these numbers the increase in parasitic drag associated with a loss or a considerable damage to a leading edge flap, a very large drag rise is expected.

A.6 Conclusions

A recent attempt to compile existing empirical aerodynamic data and program it into a working code is Reference 10. The method is based on a modification and adaptation of a code for the evaluation of the longitudinal aerodynamic characteristics of aircraft. It can handle a variety of situations like cut-outs, roughness, bluntness and more. However, like every empirical method, it is only as good as the data base on which it rests. For example, the case of through hole is based only on Reference 24, which provides low speed data. The important cases of wing-strake configuration, canard control, leading edge high lift devices are not covered. Furthermore, the transonic data base is practically non-existent.

The rough estimates of sections A.4 and A.5 show an alarming trend related to the application of sophisticated high lift devices

to fighter aircraft wings. These devices increase $C_{L_{max}}$ and C_L/C_D ratio at high values of C_L. Damage to such devices may alter the aerodynamic phenomena responsible for the improvement of the aerodynamic characteristics. In particular, some situations may lead to post stall conditions, with associated drag rise. In essence, an aerodynamically optimized wing appears to be more vulnerable to ballistic damage.

In view of these findings, a large scale aerodynamic investigation is recommended in this direction to provide the necessary foundation for the aeroelastic study.
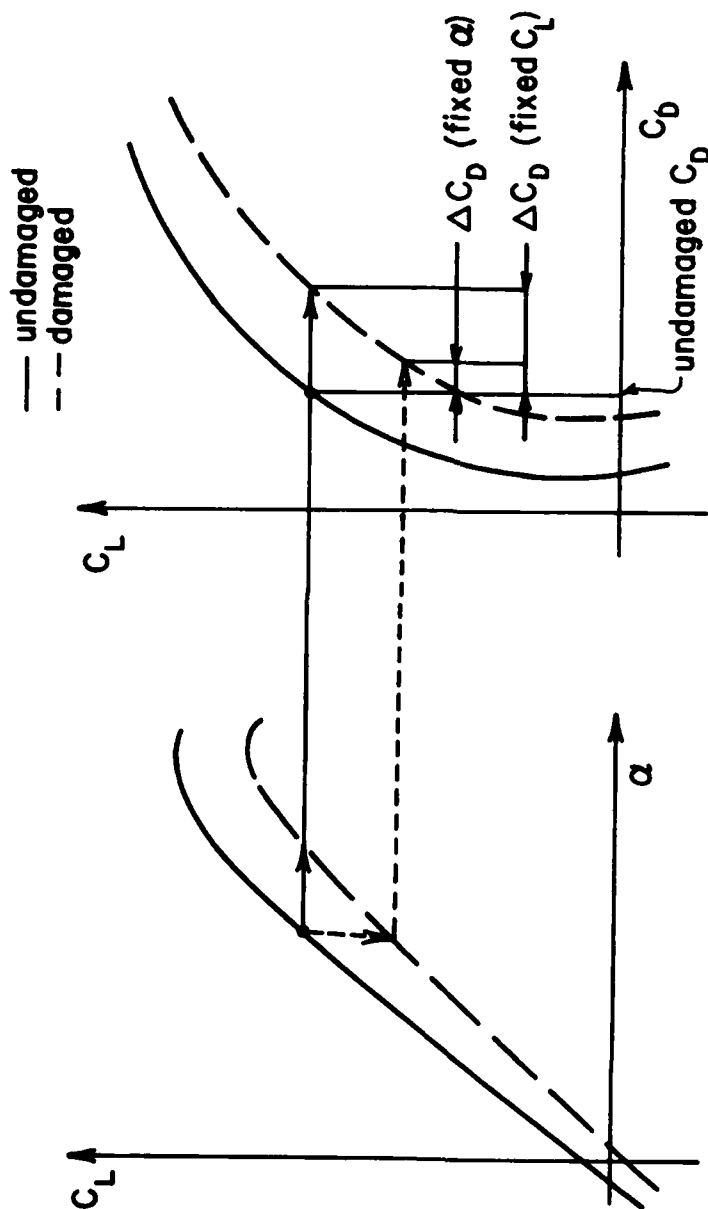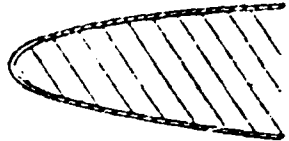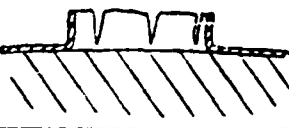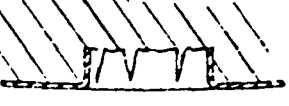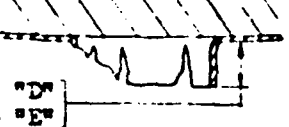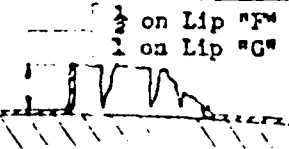
TWO WAYS TO ESTIMATE
DRAG RISE DUE TO DAMAGE

Figure A.1

Table I

Key to Configuration Notation

Hole Location	
Hole Number	Location
1	Leading edge
2	.25 chord, upper surface
3	.70 chord, upper surface
4	.25 chord, lower surface
5	.70 chord, lower surface

Lip Configuration		
Symbol	Type of Lip	Depth of Flange
A	flush	none
B	protruding	1/2 in.
C	receding	1/2 in.
D	scoop	1/2 in.
E	scoop	1 in.
F	spoiler	1/2 in.
G	spoiler	1 in.

Description of Hole Size	
Numeral	Hole Diameter*
10	.10 chord
15	.15 chord

*For leading edge holes, the diameter of an equal area circular hole.

Examples of Various Lips

Lip "A" for a leading edge hole

stream

Lip "A" for other than leading edge holes

Lip "B"

Lip "C"

Lips "D" & "E"

stream

½ on Lip "D"
1 on Lip "E"

Lips "F" & "G"

½ on Lip "F"
1 on Lip "G"

stream

denotes wing interior

DAMAGE CONFIGURATIONS TESTED IN REFERENCE 22

Figure A.2

177

M = .30

CONFIG.	$C_{D_\pi}^*$	p^*	CONFIG.	$C_{D_\pi}^*$	p^*
1A15-2A15	1.2	6.0 / 1.9	2A15-3A15	-.5	1.9 / 0
1A15-3A15	.7	3.8 / 1.9	2A15-4A15	-.1	5.0 / 6.0
1A10-2A10	1.0	5.0 / 0	2A15-5A15	-.5	3.4 / .7
1A10-3A10	1.0	3.3 / 0	3A15-5A15	-.1	1.4 / 1.4
2B15-4C15	.1	9.0 / 1.0	2A10-3A10	-.5	2.0 / 1.6
2B15-5C15	.2	7.0 / 0	2A10-4A10	1.1	4.9 / 4.3
2E15-4G15	.2	2.5 / 7.5	2A10-5A10	.5	4.0 / 2.0
2E15-5G15	.5	2.5 / .7	3A10-5A10	0	0 / 0

M = .70

CONFIG.	$C_{D_\pi}^*$	p^*	CONFIG.	$C_{D_\pi}^*$	p^*
1A15-2A15	2.4	10.0 / .7	2A15-3A15	0	2.9 / 0
1A15-3A15	1.0	.7 / 0	2A15-4A15	0	6.0 / 9.0
1A10-2A10	2.7	16.0 / -3.0	2A15-5A15	0	6.0 / 0
1A10-3A10	2.2	0 / -2.0	3A15-5A15	0	0 / 0
2B15-4C15	.7	10.0 / 0	2A10-3A10	0	3.8 / -1.6
2B15-5C15	1.0	9.0 / 1.2	2A10-4A10	0	10.0 / 10.0
2E15-4G15	1.2	8.0 / 10.0	2A10-5A10	0	9.0 / 3.8
2E15-5G15	1.0	8.0 / 0	3A10-5A10	0	0 / 0

M = .85

CONFIG.	$C_{D_\pi}^*$	CONFIG.	$C_{D_\pi}^*$
1A15-2A15	3.4	2A15-3A15	-1.5
1A15-3A15	-1.7	2A15-4A15	-.7
1A10-2A10	2.2	2A15-5A15	-1.5
1A10-3A10	-1.3	3A15-5A15	-1.0
2B15-4C15	0	2A10-3A10	-1.6
2B15-5C15	0	2A10-4A10	-2.7
2E15-4G15	4.1	2A10-5A10	-3.5
2E15-5G15	1.0	3A10-5A10	-2.1

Note: Values of p* are given in pairs. The upper figure of each pair is for α>0; the lower for α<0.

SUMMARY OF DRAG INCREASES ATTRIBUTABLE TO DAMAGE HOLES IN WINGS

Figure A.3

173
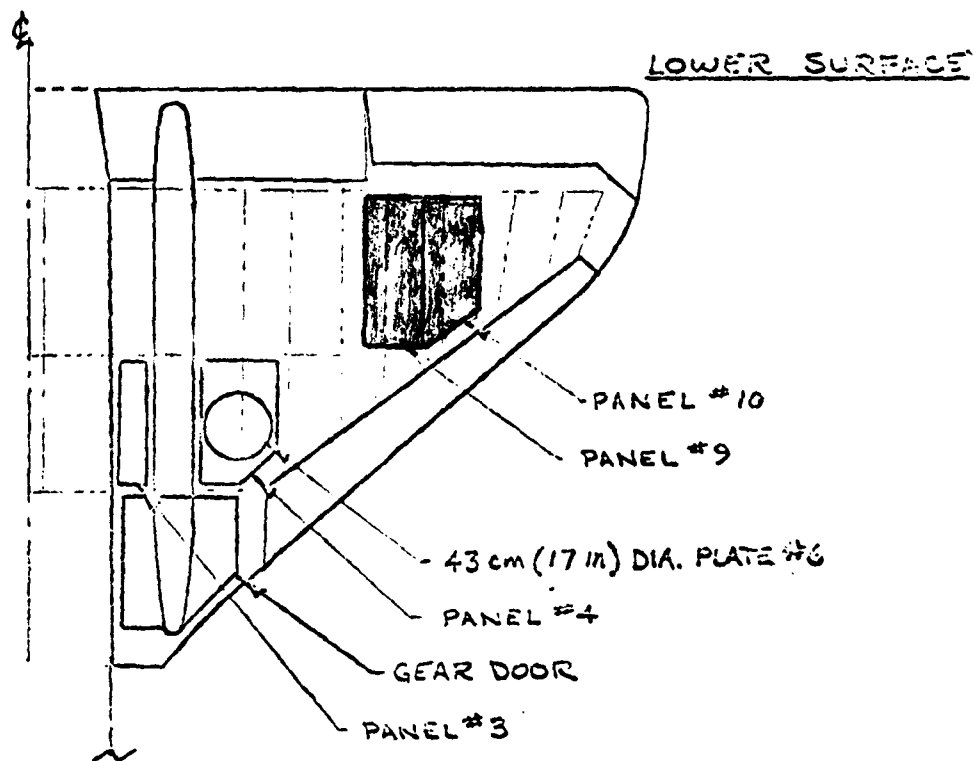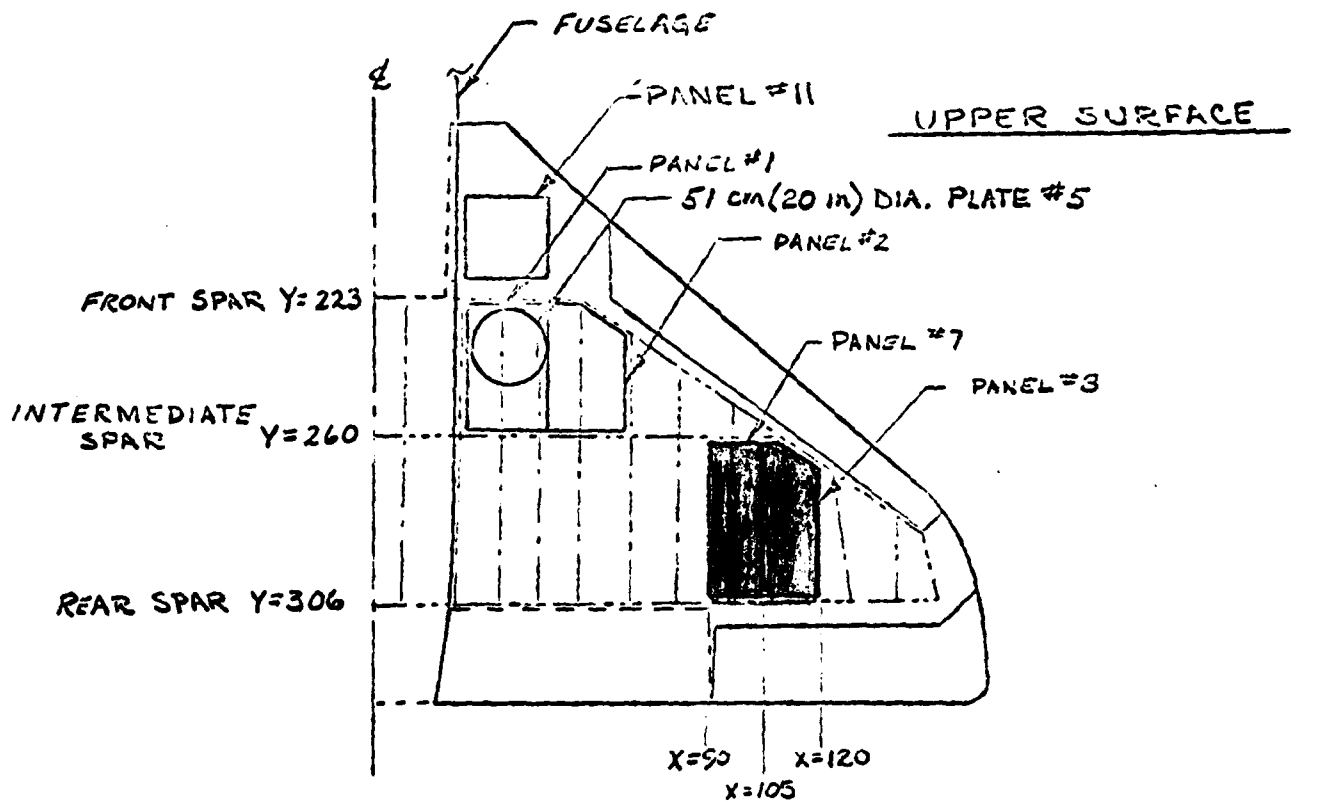
HOLE CONFIGURATION #8.   PANELS 7,8,9,&10 REMOVED
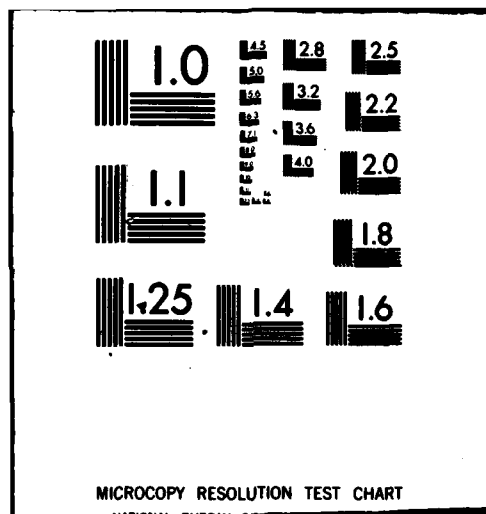
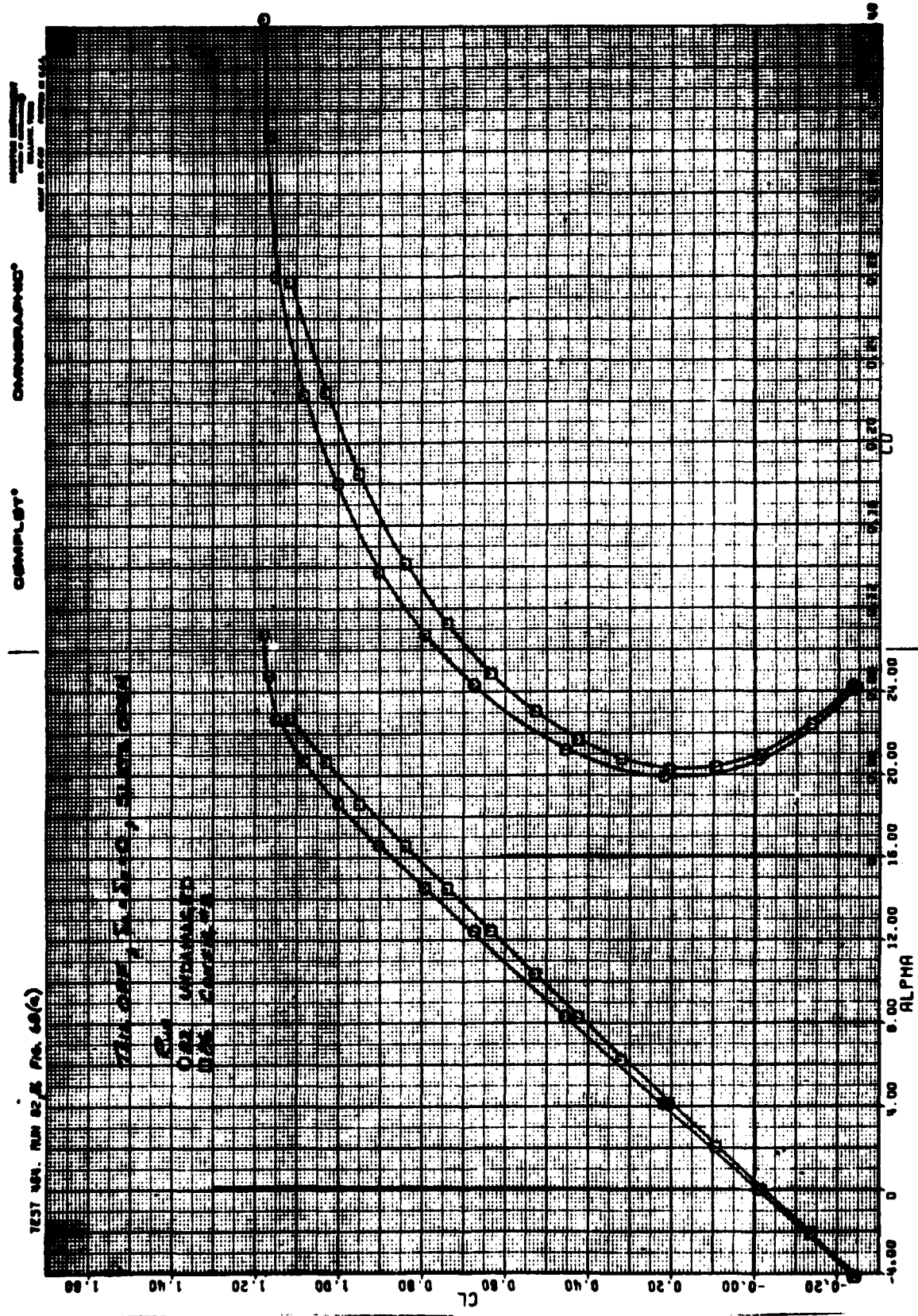A-4B WITH DAMAGE #8 (Reference 24)
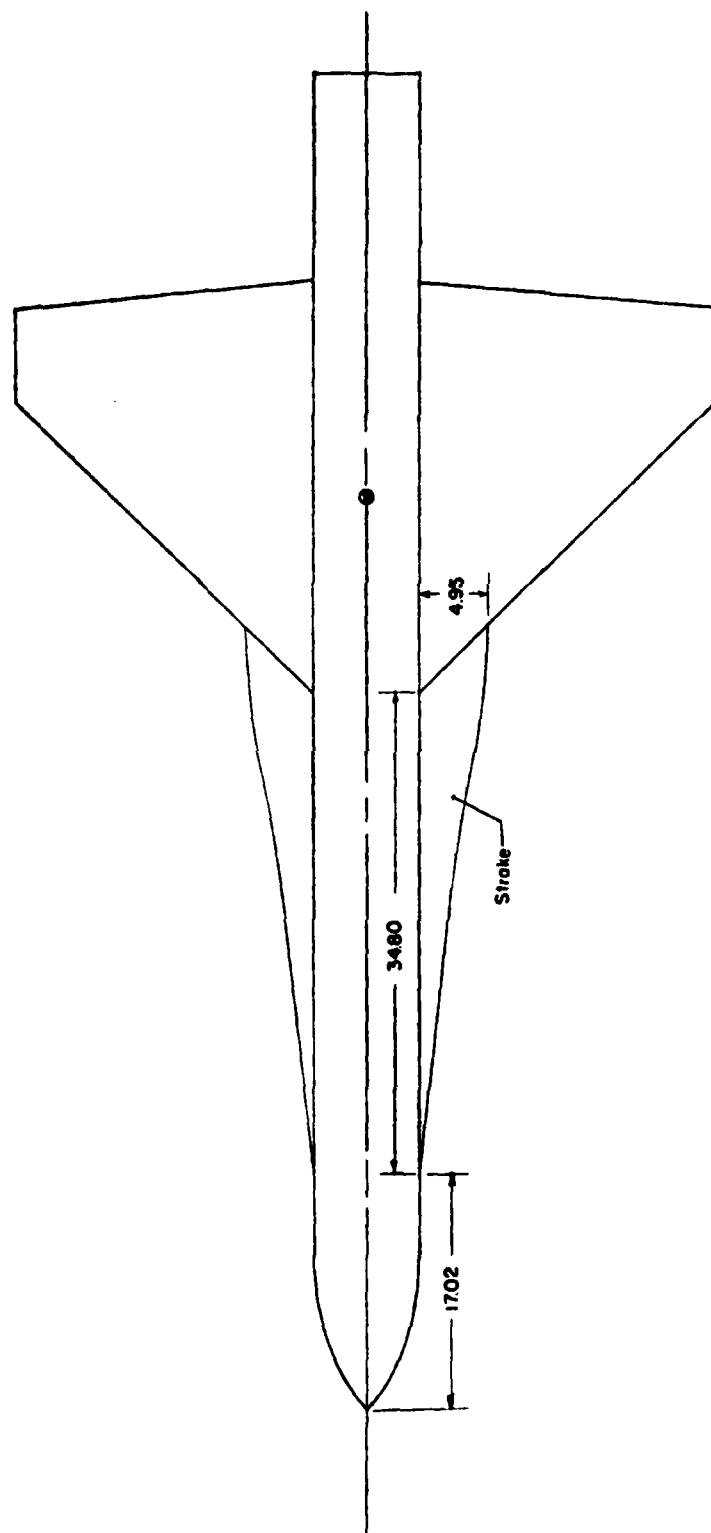
Figure A.4

MICROCOPY RESOLUTION TEST CHART

THE EFFECT OF DAMAGE #8 ON THE LIFT CURVE AND THE DRAG POLAR OF THE A-4B (Reference 24)
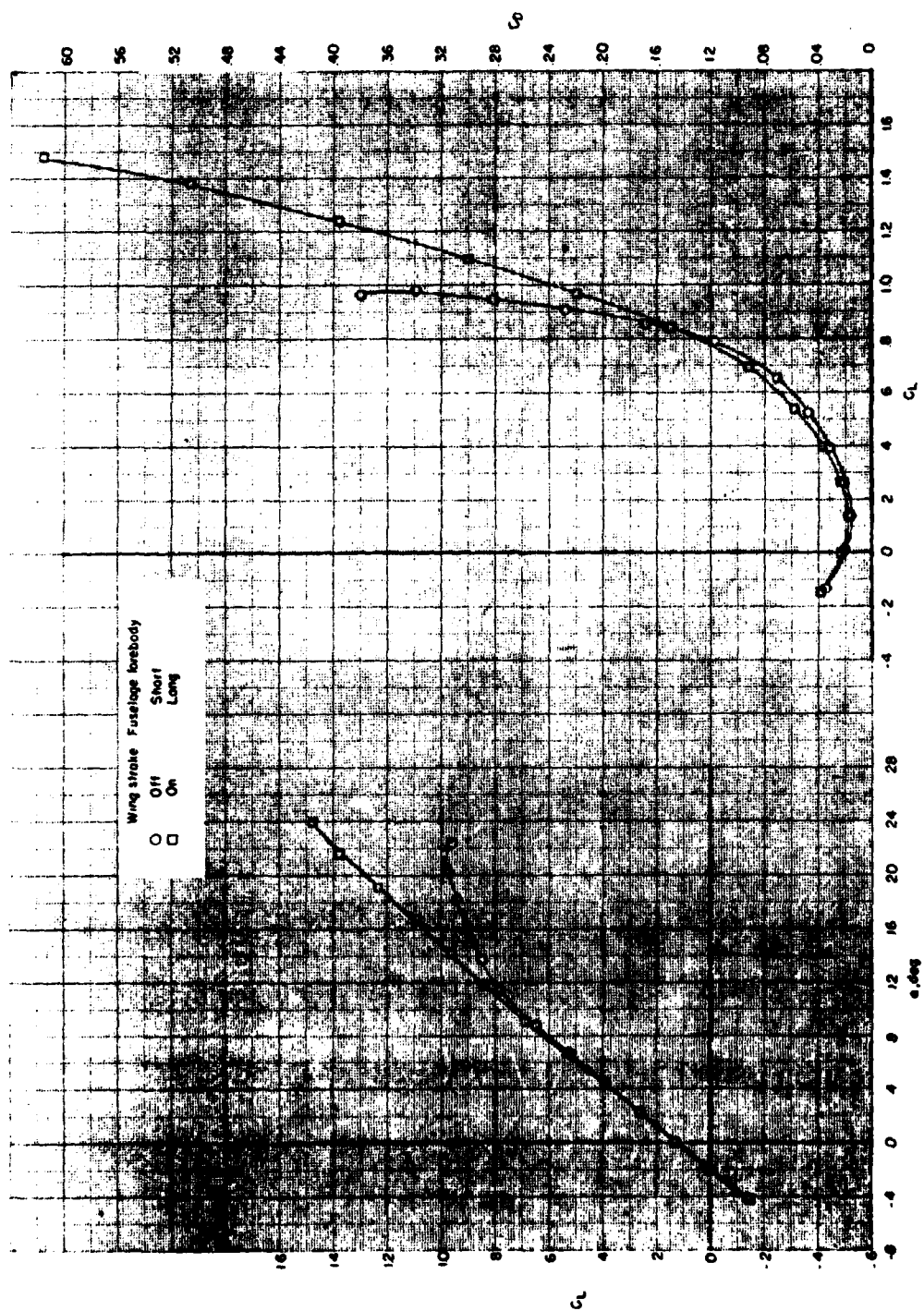
Figure A.5

(b) Details of wing strake.

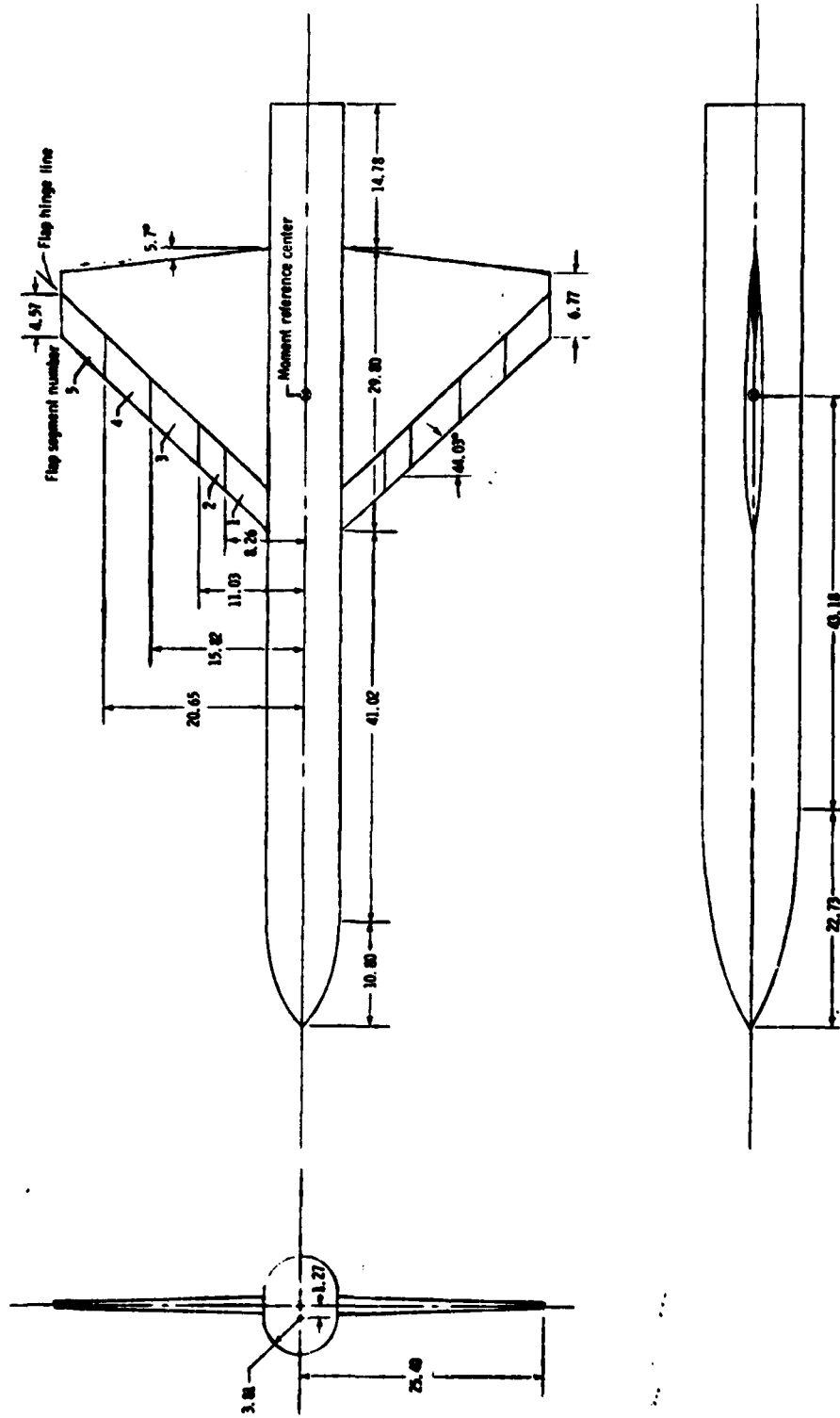WING-STRAKE-BODY CONFIGURATION OF REFERENCE 25

Figure A.6

181

(d) M = 0.70.

LIFT AND DRAG DATA FOR WING WITH AND WITHOUT STRAKE
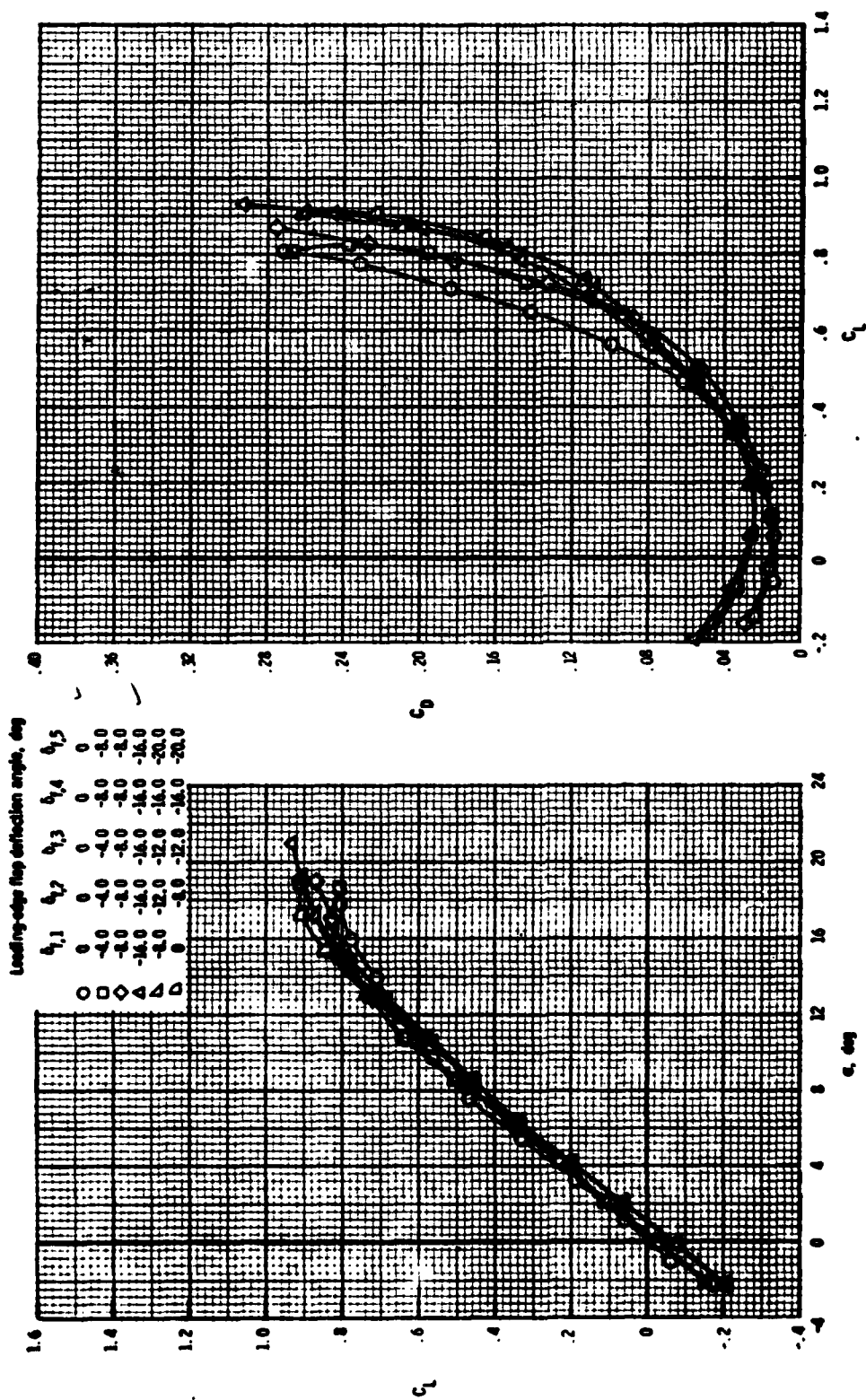
Figure A.7

182

(a) Wing-fuselage model.

Drawing of configurations under study. Dimensions are in centimeters unless otherwise noted.

MODEL OF REFERENCE 26 FEATURING LEADING EDGE FLAP

Figure A.8

183

Effect of wing leading-edge flap deflection on longitudinal aerodynamic characteristics for wing-fuselage configuration at M = 0.80.

LIFT AND DRAG DATA FOR THE MODEL OF REFERENCE 26

Figure A.9

184

REFERENCES

1. Biot, M. A. and L. Arnold, "Study of Vulnerability of Aircraft to Damaged Induced Flutter", Ballistic Research Laboratories Report No. 743, October 1950.

2. Hemmig, F. G., V. B. Venkayya, and F. E. Eastep, "Flutter Speed Degradation of Damaged, Optimized Flight Vehicles", AIAA/ASME/ASCE/ AHS 20th Structures, Structural Dynamics, and Materials Conference, St. Louis, Missouri, April 4-6, 1979.

3. Petre, A. and H. Ashley, "Drag Effects on Wing Flutter", Journal of Aircraft, Vol. 13, No. 10, October 1976, pp. 755-763.

4. Boyd, W. N., "Effect of Chordwise Forces and Deformations Due to Steady Lift on Wing Flutter", SUDAAR No. 508, December 1977 (AFOSR Contract 74-2712).

5. Breitbach, E., "Aircraft Flutter Simulation by Means of the Electronic Analogue Computer with Special Regard to Structural Non-linearities", ESRO TT-121, December 1974.

6. Stark, V. J., "Comparative Flutter Calculations for Viggen Aircraft", Journal of Aircraft, Vol. 14, No. 9, September 1977, pp. 921-922.

7. Mykyto, W. J., et al, "Investigations Concerning the Coupled Wing-Fuselage-Tail Flutter Phenomenon", Journal of Aircraft, Vol. 9, No. 1, January 1972.

8. Goetz, R. C., "Divergence of Some All-Movable Control Surfaces Including Drag Loadings", NASA TN D-4793, October 1978.

9. Shatz, R. E., "Aerodynamic Vulnerability of Aircraft", Final Report No. G1-634-6-14, Cornell Aeronautical Laboratory Inc., March 31, 1952.

10. Schemensky, R. and Roy Howel, "Aerodynamic Accounting Technique for Determining Effects of Nuclear Damage to Aircraft, Vol. I: Empirical Methods", DNA 4531F-1, prepared by General Dynamics Corporation, 1978.

11. Reece, J. W., "Interpretation of the Drag Changes Measured in the Wind Tunnel Tests of a Holed Wing", Cornell Aeronautical Laboratory, Inc., Report No. GI-634-6-1, March 1952.

12. Gail, A. and R. Shatz, "A Preliminary Estimate of the Aerodynamic Vulnerability of Subsonic Aircraft", Cornell Aeronautical Laboratory, Inc., Report No. G1-634-6-8.

13. "Military Specifications - Airplane Strength and Rigidity Flight Loads", MIL-A-8861 (ASG) 18 May 1960 - Table I, Symmetric Flight Parameters.

14. Ankeney, D. B., "Physical Vulnerability of Aircraft Due to Fluid Dynamic Effects", AGARD Advisory Report No. 106, July 1977.

15. Cunningham, A. M. Jr., "A Collocation Method for Predicting Oscillatory Subsonic Pressure Distributions on Interfering Parallel Lifting Surfaces", A.I.A.A. Paper No. 71-329, April 1971.

16. Cunningham, A. M. Jr., "An Efficient, Steady, Subsonic Collocation Method for Solving Lifting-Surface Problems", Journal of Aircraft, March 1971.

17. Cunningham, A. M. Jr., "A Steady and Oscillatory Kernel Function Method for Interfering Surfaces in Subsonic, Transonic, and Supersonic Flow", NASA CR-144895.

18. Cunningham, A. M. Jr., and Anderson, J. D., "Supplementary Notes on Appendix H of NASA CR-144895", NASA/LANGLEY Research Center, Purchase Order No. L72474A.

19. McCullough, G. B. and Gault, D. E., "Boundary-Layer and Stalling Characteristics of the NACA 64A006 Airfoil Section", NACA TN 1923, 1949.

20. Loftin, L. K., "Theoretical and Experimental Data for a Number of NACA 6A-Series Airfoil Sections", NACA Report 903, 1948.

21. Gray, V. H., "Correlations Among Ice Measurements, Impingement Rates, Icing Conditions, and Drag Coefficients for Unswept 65A004 Airfoil", NACA TN 4151, February 1958.

22. "Investigation of Characteristics of Airflow within Aircraft Structures--Phase b(1)", Cornell Aeronautical Laboratory, Inc., Report No. V-699-D-17, April 1952.

23. Abbott, Ira H. and Von Doenhoff, Albert E., "Theory of Wing Sections".

24. Betzina, M. D. and Brown, D. H., "Aerodynamic Characteristics of an A-4B Aircraft with Simulated and Actual Gunfire Damage to One Wing", NASA TMX-73, 119, July 1976.

25. Henderson, W. P. and Hoffman, J. K., "Effect of Wing Design on the Longitudinal Aerodynamic Characteristics of a Wing-Body Model at Subsonic Speeds, NASA TN D-7099, 1972.

186

26. Henderson, W. P., "Effect of Wing Leading-Edge Flap Deflection on Subsonic Longitudinal Aerodynamic Characteristics of a Wing-Fuselage Configuration with a 44° Swept Wing", NASA Technical Paper 1351, November 1958.